ILLINOIS CENTER FOR TRANSPORTATION

CIVIL ENGINEERING STUDIES
Illinois Center for Transportation Series No. 22-001
UILU-ENG-2022-2001
ISSN: 0197-9191

Bond Characteristics and Experimental Behavior of Textured Epoxy-coated Rebars Used in Concrete Bridge Decks

Prepared By
Bassem Andrawes
Ernesto Alfredo Perez Claros
Zige Zhang
University of Illinois Urbana-Champaign

Research Report No. FHWA-ICT-22-001

A report of the findings of

ICT PROJECT R27-197
Characterization of the Bond Strength of Textured Epoxy-Coated (TEC) Reinforcement Bars (Phase 2)

https://doi.org/10.36501/0197-9191/22-001

Illinois Center for Transportation

January 2022

TECHNICAL REPORT DOCUMENTATION PAGE

1. Report No.	2. Government Accession No.	3. Recipient's Catalog No.
FHWA-ICT-22-001	N/A	N/A

4. Title and Subtitle	5. Report Date
Bond Characteristics and Experimental Behavior of Textured Epoxy-coated Rebars Used in Concrete Bridge Decks	January 2022
	6. Performing Organization Code N/A

7. Authors	8. Performing Organization Report No.
Bassem Andrawes (https://orcid.org/0000-0002-8954-3751), Ernesto Alfredo Perez Claros (https://orcid.org/0000-0001-5323-7819), and Zige Zhang (https://orcid.org/0000-0002-1439-0009)	ICT-22-001 UILU-2022-2001

9. Performing Organization Name and Address	10. Work Unit No.
Illinois Center for Transportation Department of Civil and Environmental Engineering University of Illinois at Urbana-Champaign 205 North Mathews Avenue, MC-250 Urbana, IL 61801	N/A **11. Contract or Grant No.** R27-197

12. Sponsoring Agency Name and Address	13. Type of Report and Period Covered
Illinois Department of Transportation (SPR) Bureau of Research 126 East Ash Street Springfield, IL 62704	Final Report 7/16/18–1/15/22 **14. Sponsoring Agency Code**

15. Supplementary Notes

Conducted in cooperation with the U.S. Department of Transportation, Federal Highway Administration.
https://doi.org/10.36501/0197-9191/22-001

16. Abstract

The deterioration of bridge decks is a problem typically associated with the corrosion of the reinforcing steel. This issue was partially controlled during the 1970s with the incorporation of the epoxy-coating protection system. However, research later demonstrated that the smooth surface resulting from the epoxy-coating application reduces most of the friction between the rebar and the surrounding concrete. Consequently, forces acting on the rib faces are reconfigured in such a way that the radial components increase, triggering the early development of cracks. To mitigate both the reduction of bonding and the formation of cracks, the Illinois Department of Transportation proposed a new type of coated bars: textured epoxy-coated (TEC) bars. Over the last few years, different projects have been executed to understand and improve the characteristics of TEC rebars. This report is a continuation of research performed at the University of Illinois Urbana-Champaign to evaluate the bond behavior of TEC bars. The experimental program starts by characterizing, qualitatively and quantitatively, the roughness of the TEC rebars. Next, their bond-slip interaction embedded in concrete is evaluated through pull-out tests. Finite element models of these tests are developed to validate the behavior observed as the textured reinforcement loses anchorage with concrete. Based on these results, the experimental program then aims to study the impact of the drying shrinkage, temperature change, and flexural demands on two large-scale bridge deck specimens reinforced, individually, with TEC and standard epoxy-coated bars. The results collected from both specimens using digital image correlation and strain gauges are compared to explore the differences exhibited by the traditional and the new type of reinforcement coatings in terms of stress distribution in bridge decks. Finally, given the specialized equipment and time-consuming procedure needed to calculate the roughness parameters of TEC bars, an empirical, weight-based approach is developed as a rapid method for assessing the rebars' roughness on-site.

17. Key Words	18. Distribution Statement
Bridge Decks, Concrete Cracking, Reinforcement, Textured Epoxy Coating, Shrinkage, Thermal Stresses, Bending Stress, Roughness, Pull-out Test, Bond Strength, Finite Element Method	No restrictions. This document is available through the National Technical Information Service, Springfield, VA 22161.

19. Security Classif. (of this report)	20. Security Classif. (of this page)	21. No. of Pages	22. Price
Unclassified	Unclassified	66 + appendices	N/A

ACKNOWLEDGMENT, DISCLAIMER, MANUFACTURERS' NAMES

This publication is based on the results of **ICT-R27-197: Characterization of the Bond Strength of Textured Epoxy-Coated (TEC) Reinforcement Bars (Phase 2)**. ICT-R27-197 was conducted in cooperation with the Illinois Center for Transportation; the Illinois Department of Transportation; and the U.S. Department of Transportation, Federal Highway Administration.

Members of the Technical Review Panel (TRP) were the following:

- Jayme Schiff, TRP Co-chair, Illinois Department of Transportation
- Dan Tobias, TRP Co-chair, Illinois Department of Transportation
- Dan Brydl, Federal Highway Administration
- Michael Brydl, Illinois Department of Transportation
- Dana Coughlin, Illinois Department of Transportation
- Matt Mueller, Illinois Department of Transportation (retired)
- Del Reeves, Illinois Department of Transportation
- Kevin Riechers, Illinois Department of Transportation
- Mark Shaffer, Illinois Department of Transportation
- Megan Swanson, Illinois Department of Transportation
- Scott Hughes, Illinois Department of Transportation

The research group of this project would like to acknowledge the contribution received from Dr. Grzegorz Banas and Dr. Alex Weber-Kamin. Their insight was important to effectively conduct the series of experiments performed at the Newmark Structural Engineering Laboratory facilities. Likewise, special gratitude is extended to the machine shop team, led by Mr. Kyle Cheek, whose work was essential for the test setups to become a reality.

EXECUTIVE SUMMARY

Currently, epoxy-coated rebars are widely used in bridge structures to mitigate the corrosion of reinforcing steel. However, research and practical experience have shown that the smoothness from the traditional epoxy coating significantly reduces the bond between the concrete and steel bars. This condition often triggers the early development of transverse cracks in bridge decks. Thus, to palliate this problem, the Illinois Department of Transportation (IDOT) proposed a new type of textured epoxy-coated (TEC) reinforcement. It incorporates an increased surface roughness that seeks to enhance the bond with the surrounding concrete while continuing to act as a cost-effective corrosion-protection system.

This investigation was conducted to evaluate the structural performance of TEC rebars and to increase the knowledge about this novel technology. The experimental program started by focusing on numerical studies and small-scale tests, which were intended to understand the principal characteristics of the different types of TEC bars developed hitherto and how they impacted the bond-slip behavior with concrete. First, the surface roughness of the TEC rebars was compared to that of uncoated (UC) and standard epoxy-coated (EC) rebars using 2D and 3D roughness parameters, which were calculated through Gaussian-filtered topology analyses. Second, direct pull-out tests were carried out on concrete specimens reinforced with UC, EC, and TEC bars. This contrasted their respective bond strength and slip-resistance progression as the anchorage level decreased. Overall, TEC bars exhibited better performance in terms of initial slip resistance. Additionally, a 3D finite element model was developed and calibrated to simulate the bond-slip behavior of TEC bars embedded in concrete. As a complement, the basis of a procedure—possible to replicate in the field of construction—that correlated the roughness of TEC rebars with a weight-based index was established. This series of steps aimed to have an empirical resource to preliminarily classify specific types of coatings.

The next phase of the experimental program focused on examining the influence of TEC reinforcement on structural behavior at large scales. Therefore, and as a means of comparison, two laboratory bridge deck specimens were built, one of which incorporated EC bars and the other one TEC bars. Except for the coating type, both specimens were identical. The type of bar used in the TEC specimen combined the characteristics of previously tested TEC bars that exhibited a higher potential in improving the bond-slip behavior. Three tests were conducted on the large-scale specimens: shrinkage, temperature effect simulation, and flexural tests. The shrinkage and temperature effect simulation tests were intended to monitor, study, and compare the strain distribution and potential cracks arising from the effects of the drying process and thermal loads, respectively. The drying process is induced by the movement and loss of internal moisture, while thermal loads are induced by temperature gradients between the elements of the bridge composite section. The flexural test intended to study and compare the load-deflection relationship and elastic stiffness under flexural stresses generated by a tandem load in a simply supported boundary condition. In all the large-scale experiments, strain gauges and digital image correlation (DIC) techniques were utilized as the instrumentation strategies. They made it possible to have a comprehensive understanding of how the strain was spatially distributed during different stages of interest. The results from the shrinkage test suggested that TEC bars interacted better with the surrounding concrete. In other words, TEC rebars

were more actively resisting the stress induced by the shrinking action from the concrete. Regarding the temperature effect simulation test, more but finer cracks occurred in the specimen that incorporated TEC bars. This observation implied lower exposure of the reinforcement to external agents. Ultimately, the results of the flexural test demonstrated that TEC bars possessed higher resistance to slip and crack widening. The EC specimen, on the other hand, demonstrated more flexibility under flexural demands, which might be related to the lower bond between the rebars and the surrounding concrete.

In general, despite that the series of tests carried out in this investigation represent some of the most relevant stress conditions experienced by bridge decks, more research is needed to evaluate the characteristics of TEC bars under other types of demands, such as fatigue, cyclic thermal loading, and aging.

TABLE OF CONTENTS

LIST OF FIGURES

LIST OF TABLES

CHAPTER 1: INTRODUCTION

MOTIVATION OF THE RESEARCH

The Federal Highway Administration (FHWA) states in their National Bridge Inventory that 7.5% of highway bridges were structurally deficient in 2019 (FHWA, 2019). Regrettably, as the American Society of Civil Engineers (ASCE) mentioned, the rate of deterioration is currently exceeding the rate of repair, rehabilitation, and replacement, which makes it an unsustainable model (ASCE, 2021). One of the reasons for this problem is the occurrence of transverse cracks (perpendicular to traffic) in bridge decks. Many factors can trigger their development but, as explained by Babaei and Fouladgar (1997), drying shrinkage, thermal shrinkage, and flexural stresses are some of the most relevant ones. These cracks, typically of full depth and spaced 3 ft–10 ft (0.90 m–3.0 m) apart along the length of the span, develop at the early ages of bridge deck life, sometimes right after construction or at early stages of operation under roadway traffic (Saadeghvaziri & Hadidi, 2005). In general, cracks are prejudicial because they create a path for water and deicing salts to reach the steel, often leading to corrosion of the reinforcement (Frosch et al., 2010). Once the reinforcement is compromised, the life span of the structure is reduced, and the repair measures are laborious and costly. By 2013, the Association for Materials Protection and Performance (AMPP) estimated the annual direct cost of corrosion for highway bridges in the United States to be $13.6 billion (AMPP, 2021). Also, aesthetically, leakage through the cracks onto structural members and components beneath the deck gives the bridges a poor appearance (Krauss & Rogalla, 1996).

To overcome the susceptibility of bridge decks to cracking and other structural problems, bridge engineers are now using materials such as ultra-high-performance concrete, corrosion-resistant reinforcement, high-performance steel, composites, and improved coatings to increase resilience and add durability (ASCE, 2021). The latter is one of the research topics that the Illinois Department of Transportation (IDOT) has been studying lately. They identified that almost no account had been given to the friction between the concrete and steel because, as mentioned by Treece and Jirsa (1989), the bearing of the rebar deformations against the concrete is normally considered the major component of bond strength. Moreover, the traditional approach of using standard epoxy-coated (EC) bars produces the opposite effect, reducing the bond strength because the texture of the coating is smoother than the mill-scale finish of the uncoated (UC) reinforcement (Cairns & Abdullah, 1994). As a result, IDOT developed a new type of coated rebar with a roughened surface. The so-called textured epoxy-coated (TEC) reinforcement is manufactured by applying an additional layer of polymeric powder, and it is intended to enhance the bond-slip interaction by increasing the friction component at the rib faces. TEC bars have already been used in real bridges in Illinois but, disconcertingly, transverse cracks were still observed at the early stages after construction.

This research intends to explore the reasons for these cracks by conducting some analytical and experimental studies on the TEC rebars. To assess how the surface profiles of the TEC reinforcement impact its behavior with concrete, it was important to determine the roughness parameters of the different types of TEC bars and characterize their bond-slip relationships. The latter aspect was assessed through pull-out tests, using different concrete strengths and degrees of confinement. However, small-scale tests do not precisely describe the state of stresses encountered in actual

bridge instances and, thus, a more precise appraisal was incorporated to resemble a practical scenario. Correspondingly, two large-scale laboratory bridge deck specimens were built and specially designed to evaluate the effects of the coating type under shrinkage, thermal, and flexural demands. Both specimens shared the same properties, except that one was reinforced with TEC bars while the other one was reinforced with EC bars. For the specimen reinforced with TEC bars, the surface roughness of the bars was selected based on the promising results of the initial characterization of the surface profiles of TEC bars with a wide range of roughness parameters. Ultimately, the costly and time-consuming procedures at the time of evaluating the effectiveness of the textured coating led to developing a methodology to correlate the roughness parameters with an empirical weight-based index. This methodology can help determine the acceptance of the TEC bars on the field.

BACKGROUND ON BOND THEORY

Contrary to what was believed for many years, it is now clear that bond strength depends not only on the materials but also on the geometry of the reinforcing bars and the characteristics of the structural members themselves (ACI Committee 408, 2003). Hence, in structural design and construction, it is important to guarantee a satisfactory interaction between the rebars and the surrounding concrete so that the theory of reinforced concrete accurately describes the behavior of the members built with this compound material.

When rebars are subjected to demands, nonconstant bond stresses are generated throughout them. This condition has led researchers to analyze short bonded lengths over which bond stress and bond-slip may be considered uniform (Cairns & Plizzari, 2003). In these regions, bond stress can be defined as the axial force developed in the reinforcing bar divided by the surface area of the rebar in the anchorage length (Cleary & Ramirez, 1991). Therefore, bond strength represents the maximum force the steel bars can withstand on their longitudinal axis without significantly losing anchorage.

The transfer of forces from the reinforcement to the surrounding concrete occurs for a deformed bar by three components: chemical adhesion between the rebar and the concrete, frictional forces arising from the roughness of the interface, and mechanical anchorage or bearing of the ribs against the concrete surface (ACI Committee 408, 2003). However, the contribution of chemical adhesion is often considered negligible. In addition, the bar slip relative to concrete plays an important role in the transferring mechanism. First, for any bar to slip, adhesion and friction at the reinforcement surface must be overcome. Second, the level of slip determines the way frictional and bearing components interact with each other. As Cairns and Abdullah (1994) explained, at large slips, relative movement on a shearing surface across the top of the ribs predominates, provided a splitting failure is prevented. At small slips, once the friction on the barrel of the rebar is reduced, movement is concentrated in the vicinity of the bearing face of the rib, and changes in bond performance are closely related to the frictional properties of the rib face. In the latter scenario, when confinement is not granted but the friction is significant, it should stop the concrete key from sliding relative to the rib. Thus, if there was a way to constantly preserve an adequate level of friction on the ribs, an effective transfer of forces would be achieved, and it would be more difficult for cracks to develop.

Based on the previous discussion, and as expressed by Cairns and Abdullah (1994), the forces acting on the rib face are resolved into a normal component, F_{n}, perpendicular to the rib face, and a shear component, F_{f}, parallel to the face. They may also be resolved into a bond component, F_{b}, parallel to the bar axis, and a radial splitting component, F_{r}, perpendicular to the bar axis. Figure 1 illustrates their arrangement for flat and steep ribs combined with normal and low-friction surfaces. There, the force due to friction is added vectorially to the bearing component (Treece & Jirsa, 1989). The same happens if the other approach is considered, where the radial force is added vectorially to the bond component. Both cases share the same resultant, yet the values of the four forces cannot be determined by statics alone, as only two equilibrium equations can be set up (Cairns & Abdullah, 1994). To determine them, information on the load-deformation characteristics of each component would be necessary.

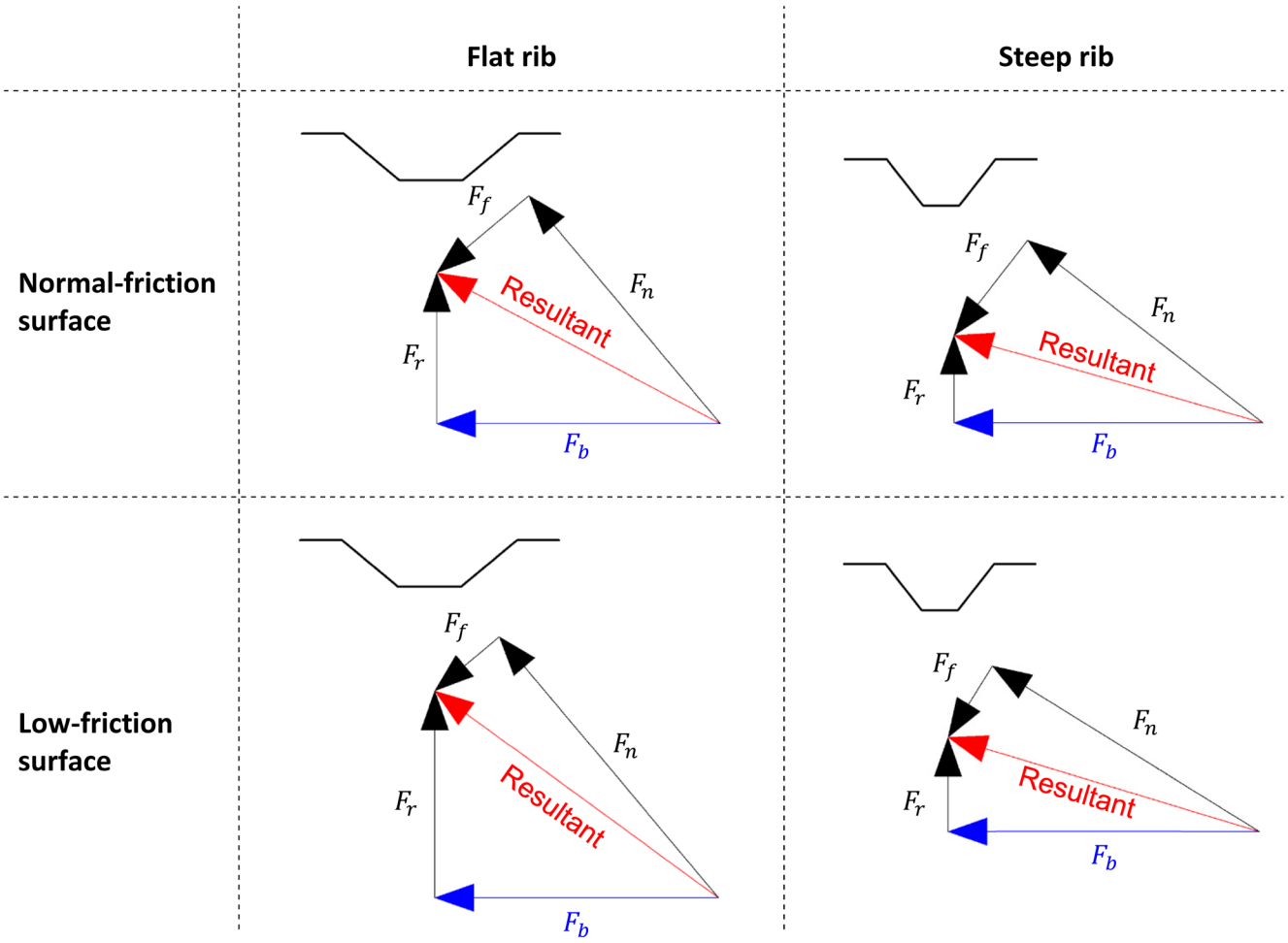

Figure 1. Illustration. Forces acting on flat and steep ribs of rebars with normal and low-friction surfaces.

Figure 1 displayed the condition for constant bond strength and sufficient radial resistance. Nevertheless, from the second row, it is clear that if the friction between the concrete and steel is small or negligible, such as in standard epoxy-coated reinforcement, the predominant component of

the bond strength is the force perpendicular to the face of the rib, F_n (Treece & Jirsa, 1989). The augmented bearing force is required to develop an equivalent bond strength, and it increases, in turn, the radial component. This situation, as seen in Figure 1, has greater consequences on rebars with flat ribs. As Treece and Jirsa (1989) explained, the amount of radial pressure the concrete cover can resist before splitting around the bar can additionally control the magnitude of the bond force. For example, if the capacity of the cover is constant, rebars with no friction will have a much smaller bond capacity than rebars that develop friction between the concrete and the bar lug (Treece & Jirsa, 1989).

Figure 1 also demonstrated that, theoretically, steep rib faces have a better performance than flat ribs. Idun and Darwin (1999) determined that epoxy-coated rebars show the same performance as uncoated ones for rib face angles greater than or equal to 45 degrees. However, in practice, it is difficult to roll bars with face angles as steep as that (Idun & Darwin, 1999). Moreover, it is challenging to achieve a uniform coating thickness on them because the coating builds up on the bearing face of the rib, originating variations in the angle along the rib face. This results in an overall smaller angle than intended. Bendability and fatigue endurance tend to reduce with increasing rib steepness, too (Cairns & Abdullah, 1994).

REPORT OUTLINE

This report contains nine chapters. First, the report will introduce the reader to the bond behavior concepts with a brief theoretical background and how it relates to the topic of the research. After that, the report presents the methodology and analyzes the results of the experimental program conducted at the University of Illinois Urbana-Champaign. The scope of each chapter is as follows:

Chapter 1 covers the motivation of this research and a concise literature review about bond behavior, highlighting the different forces acting at the steel-concrete interface.

Chapter 2 contains the qualitative description of the TEC rebars and the methodology of quantitatively measuring and evaluating the surface roughness. Based on this, different roughness parameters of TEC bars were determined and compared to those of uncoated (UC) bars.

Chapter 3 presents the procedures and experimental outcomes of pull-out tests on specimens reinforced with UC, EC, and different types of TEC bars, including their resulting bond strength and bond-slip characteristics as slip progressed. This chapter also explains the finite element (FE) studies conducted to understand the interaction mechanism between the TEC rebars and the surrounding concrete. The FE software ABAQUS (Dassault Systèmes Simulia Corp., 2014) was used to create a 3D model of a pull-out specimen. It considered the detailed geometry of the steel bar and cohesive behaviors as the interaction between the rebar and concrete. The numerical results were compared with the experimental for validation, and stress contour plots were generated to gain an understanding of the interaction mechanism at different stages of the pull-out action.

Chapter 4 describes the characteristics of the large-scale laboratory bridge deck specimens. It explains the considerations taken into account when designing them, their construction process, and the principal properties of the materials used to build them.

Chapters 5, 6, and 7 discuss the experimental program for the large-scale specimens, including the different setups, the implemented instrumentation strategies to acquire the data, and the analysis of the results. Chapters 5 and 6 describe the shrinkage and temperature effect simulation tests, respectively, which are complemented by a comparison of the behavior, strain distribution, and cracks exhibited by the specimens. Chapter 7, in turn, describes the flexural test. Similarly, a comparison of the strain distribution was performed, accompanied by the evaluation of the overall elastic stiffness exhibited by both specimens.

Chapter 8 explains the procedure and results of the empirical roughness measurement methodology developed to correlate a weight-based index with the roughness parameters of the TEC bars.

Chapter 9 summarizes the major findings of the study.

CHAPTER 2: SURFACE ROUGHNESS CHARACTERIZATION

SPECIMEN DESCRIPTION

Six types of TEC bars coated with different texture patterns were studied initially. They were classified from TEC1 to TEC6. Regarding their manufacturing process, one company was in charge of TEC1 to TEC3 rebars, while a different company manufactured TEC4 to TEC6. In both cases, however, the same polymeric powder was used to create their texture. The details of the coating application procedure are proprietary, but the different texture roughnesses were created by varying the size and density of the applied powder.

To perform a qualitative comparison of the surface characteristics of the textured reinforcing bars, they were visually examined through a microscope, and the results are shown in Figure 2. All profiles showed voids with various densities and sizes, except TEC1. For example, TEC4, TEC5, and TEC6 rebars appeared to have larger voids than TEC2 and TEC3, with the voids of TEC5 being slightly smaller than those of TEC4 and TEC6.

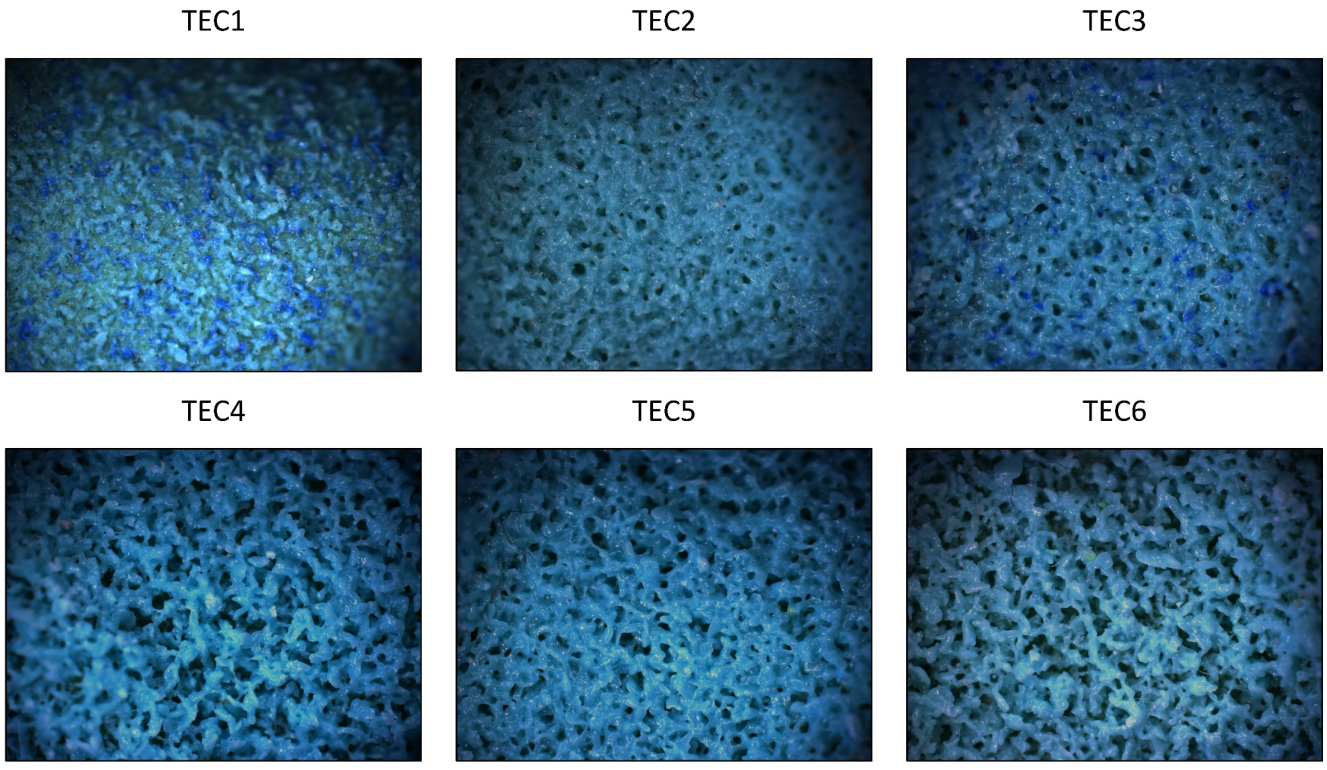

Figure 2. Photo. Microscopic images of TEC bars.

SURFACE ROUGHNESS QUANTIFICATION

Besides the previous qualitative description of the TEC bars' surface textures, a quantitative evaluation was necessary to determine their roughness parameters. For that purpose, 2D and 3D profile analyses were run on 3 in. long (76.2 mm) samples of each textured rebar type. The profile measurements were executed by a stylus-based profilometer with a surface height range of $41.26 \times 10^{-3} \pm 20.63 \times 10^{-3}$ in. (1048 ± 524 μm) and a resolution of 2.46×10^{-6} in. (0.0625 μm). The stylus had a 7.87×10^{-5} in. (2 μm) radius tip and scanned the surface with a contact force between 1.10×10^{-6} lb–1.10×10^{-4} lb (0.5 mg–0.50 mg). The apparatus and the steel bar sample are shown in Figure 3.

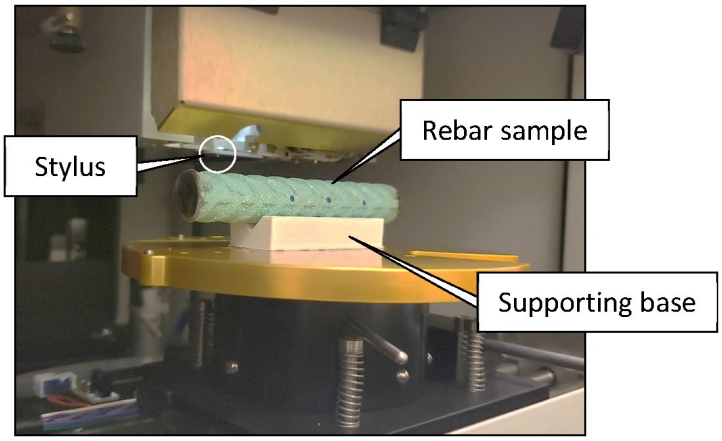

Figure 3. Photo. Roughness measurement setup using the profilometer.

For both the 2D and 3D analyses, the raw surface profiles had to be measured first. Then, the data was post-processed using a MATLAB script code to eliminate the effects of noise and the long waviness of the measured surface. The code applied the Gaussian filter based on the International Organization for Standardization (ISO) 16610-21 (ISO, 2011), which has been widely used for surface analysis. Initially, the digitalized raw profile of the bar specimens was filtered using an S-filter with a short cutoff wavelength, λ_s, of 3.15×10^{-4} in. (8 μm). ISO 3274 (ISO, 1996a) recommends this to suppress the high-frequency noise that is included during the measurement. Then, the primary profile was filtered again using an L-filter to separate the roughness and waviness profiles. A long cutoff wavelength, λ_c, was used first to obtain a waviness (low frequency) profile, and the roughness profile was generated by subtracting this waviness profile from the primary one. ISO 4288 (ISO, 1996b) recommends different λ_c values that range from 0.0032 in. (0.08 mm) to 0.32 in. (8 mm), depending on the roughness of the filtered profile. In this study, and based on the short available scan length of roughly 0.20 in. (5 mm) between the rebar ribs, λ_c was taken as 0.10 in. (2.5 mm).

Once the filtered profiles were obtained, the different roughness parameters were calculated. They are normally classified into amplitude, spacing, and hybrid parameters, according to their

functionality (Gadelmawla et al., 2002). Among all parameters, the amplitude parameters were the most relevant to study the impact of the roughness on the bond strength with concrete, because they depict the deviations perpendicular to the bar surface. From the 2D analysis, the linear parameters R_a and R_{max} were determined as the average of the measurements taken in three regions of each sample. Each region, in turn, was separated by a rib in between and consisted of three 0.20 in. long (5000 µm) lines with a spacing of 0.002 in. (50 µm). As defined by Gadelmawla et al. (2002), R_a represents the average absolute deviation of the roughness irregularities from the mean line over one sampling length, while R_{max} represents the vertical distance between the highest peak and the lowest valley along the assessment length of the profile. Although R_a and R_{max} provide certain insight on the bar surface roughness, they do not reflect the spacing between the peaks and their skewness because two different surface topologies may share the same values. Therefore, to obtain the full picture of the surface roughness, 3D analyses were also conducted. A 0.10 × 0.10 in. (2.5 × 2.5 mm) square area placed between the ribs of each rebar was evaluated. The area of analysis was created by a set of 251 longitudinal lines, separated from each other 3.94×10^{-4} in. (10 µm) in the transverse direction. For each area, S_a and S_{max} were determined. They are the surface homologs of R_a and R_{max}. Specifically, S_a is based on the average absolute deviation from the mean line over the sampling surface, and S_{max} evaluates the difference in height between the highest peak and the lowest valley along the sampling surface.

The experimental results were separated into two phases. In the first phase, the linear and surface roughness parameters of TEC1 to TEC6 rebars were compared to those of the uncoated ones. These calculations were complemented with the pull-out test results, as will be portrayed in the next chapter. Based on these findings, a new type of TEC bar, labeled TEC7, was manufactured. The TEC7 rebar was intended to combine the characteristics of the TEC2, TEC3, and TEC6 bars, as they showed a higher potential in improving the bond-slip behavior. Because TEC2 and TEC3 were provided by a different manufacturer than TEC6, the TEC7 rebars were made by the first manufacturer with consultation from the second one to combine the advantages of both of their roughness application procedures. Finally, the second phase of the results incorporated the roughness parameters of the newly developed TEC7 reinforcement. Figure 4 summarizes the results obtained for each calculated surface parameter.

The R_a and R_{max} values, shown in Figure 4, of all TEC bars were at least four to eight times greater than those of the UC bars, which proved the significantly increased roughness magnitude on their surface. Among all TEC bars, TEC7 manifestly had the highest R_a and R_{max} values. From S_a and S_{max} two main groups could be identified, where TEC4 to TEC7 had much rougher surfaces than those of TEC1 to TEC3. Among TEC1 to TEC3 bars, TEC1 had a slightly higher S_a value than the other two. Based on the microscopic images presented in Figure 2, TEC1 rebars, unlike TEC2 to TEC6 rebars, exhibited no surface voids. Consequently, it was not readily apparent whether the presence of voids had any impact on the surface roughness. Lastly, TEC6 had the highest S_a value, while TEC7 held the highest S_{max} value.

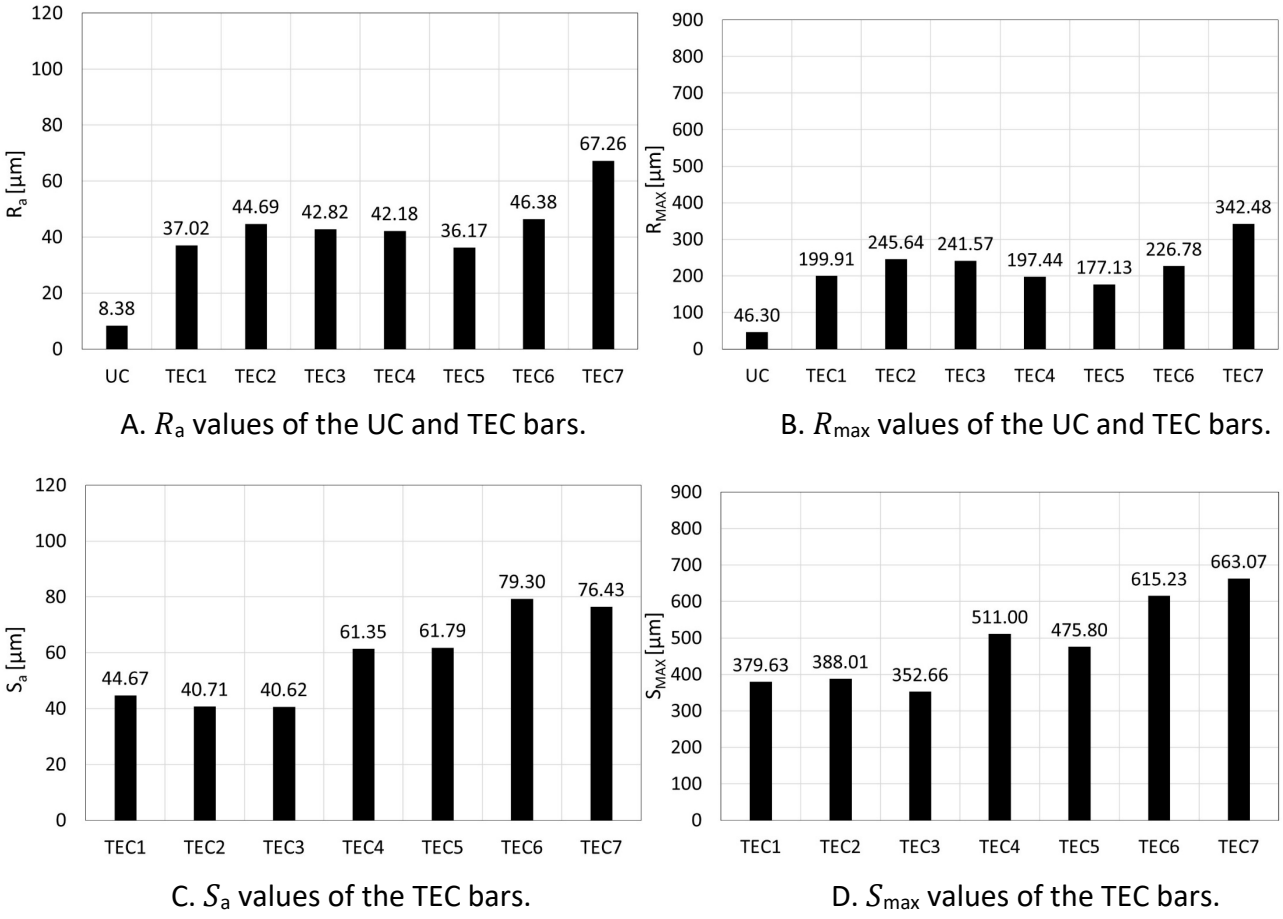

A. R_a values of the UC and TEC bars.

B. R_{max} values of the UC and TEC bars.

C. S_a values of the TEC bars.

D. S_{max} values of the TEC bars.

Figure 4. Graph. Comparison of linear and surface roughness parameters of the studied rebars.

CHAPTER 3: PULL-OUT TESTS

After examining the surface of various TEC bars, it was essential to correlate their profiles with the bond-slip behavior they exhibit embedded in concrete. To achieve this objective, a pull-out test program was carried out to compare the bond strength of TEC rebars with that of EC and UC rebars, all of which were made from Grade 60 steel (F_Y = 60 ksi, E = 29000 ksi). The results provided a global comparison of all TEC, EC, and UC bars.

SPECIMEN PREPARATION AND TEST SETUP

The specimens' dimensions, illustrated in Figure 5-A, and the detailed test procedure were based on the International Union of Laboratories and Experts in Construction Materials, Systems, and Structures (RILEM) pull-out test specifications (RILEM, 1994). In these tests, an increasing tensile load is applied to one end of the reinforcing bar until it slips as the bond strength between itself and the surrounding concrete is surpassed. The concrete block had both a diameter and a height of 6 in. (152.4 mm). The reinforcement for the pull-out specimens consisted of No. 5 steel rebars with a bonded length, l_e, of 3.0 in. (76.2 mm), equivalent to l_e/d_b = 4.8. A typical specimen utilized for this test is shown in Figure 5-B.

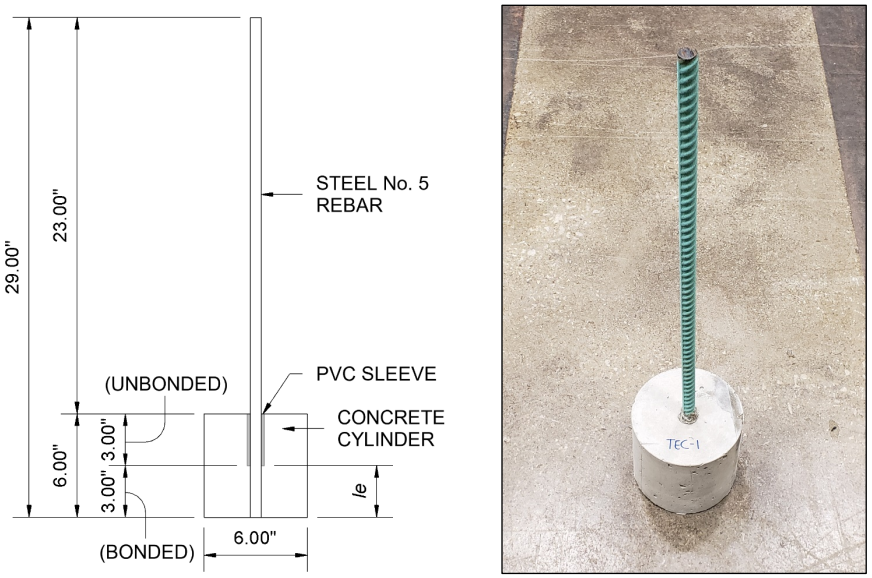

A. Pull-out specimen dimensions. B. Actual pull-out specimen.

Figure 5. Illustration and photo. Typical pull-out specimen.

The specimens were cast vertically and upside down so that the surface being pulled against the loading frame can be kept flat. Round, commercially available concrete form tubes made from plastic with their upper half removed were used for the activity, as shown in Figure 6-A. In addition, to avoid the adherence of concrete over the unbonded regions of the rebars and the creation of significant end-effects, polyvinyl chloride sleeves were installed, adjusting their position by sealing their ends with silicone-based caulk. If bond breakers were not installed, the specimens would experience a loss

of bonding caused by the development of cone-type cracks near the loaded end. On the opposite side, at the unloaded end, a linear variable differential transformer (LVDT) was installed, concentrically aligned to the exposed, epoxy-coated free, reinforcing bar end, to record the slip. The device was mounted on an aluminum support glued to the base of the specimen, given that the slip should be determined as the relative displacement of the rebar with respect to the concrete bottom surface. Two different uniaxial servo-hydraulic frame systems were used to complete the testing program. In both cases, the machines were modified to include an assembly of plates through which the concrete block could react to trigger the slip of the bar while it was being pulled. Figure 6-B shows a pull-out specimen positioned in one of the frames. The load was applied at a rate of 1/1000 of the rebar diameter per second, equivalent to 0.0375 in./min. (0.95 mm/min.), until a significant slip was observed.

A. Specimen casting molds. B. Testing setup.

Figure 6. Photo. Pull-out test specimen preparation and testing.

Four types of concrete mixtures were used. The first three batches comprised individually eight specimens, including one UC, one EC, and six TEC bars (TEC1–TEC6), while the fourth batch comprised six specimens, including two UC, two EC, and two TEC7 bars. Batch 4 was also used for casting the large-scale specimens built for the next phases of the experimental program, as will be discussed in upcoming chapters. Table 1 presents a summary of the compressive strength of the four batches utilized in the fabrication of the specimens.

Table 1. Summary of the Batches Used in the Pull-out Tests

Batch ID	Batch 1	Batch 2	Batch 3	Batch 4
Confinement type	Unconfined	Unconfined	Confined with 2 layers of CFRP	Unconfined
28-day-old compressive strength, f'_c	5.80 ksi (40.0 MPa)	9.20 ksi (63.4 MPa)	8.30 ksi (57.2 MPa)	7.25 ksi (50.0 MPa)

For the direct pull-out test, there are two possible failure modes: splitting and pull-out. However, the probability of experiencing one or the other failure mode in practical field conditions is based on factors such as concrete strength, concrete cover, bar spacing, or degree of confinement. For instance, for high-strength concrete or concrete with a small cover, splitting failures are more likely to happen (Lundgren, 2005). After running tests for Batches 1 and 2, most failures were found to occur due to the splitting of the specimens. To ensure that both failure modes were well represented in the data, Batch 3 specimens were confined prior to testing using carbon fiber–reinforced polymer (CFRP) sheets. The CFRP sheet had a ply thickness of 0.049 in. (1.25 mm), an ultimate elongation of 0.98%, a tensile modulus of 13,000 ksi (89,630 MPa), and a tensile strength of 135 ksi (930 MPa). The specimens were confined with two layers of CFRP sheets, applied using the wet-layup method, on a height of 4 in. (101.6 mm) starting from the bonded region. In Batch 4, both failure modes were well represented in the results. Figure 7 presents an example of both failure types observed in the tests.

A. Pull-out failure. B. Splitting failure.

Figure 7. Photo. Failure modes exhibited by the pull-out specimens.

TEST RESULTS

Peak Strength

Figure 8 presents a comparison of the peak strength of the bars from the four batches. The nominal yield strength of No. 5 rebars, calculated as 18.6 kips (82.7 kN), was additionally included as a reference in the plot.

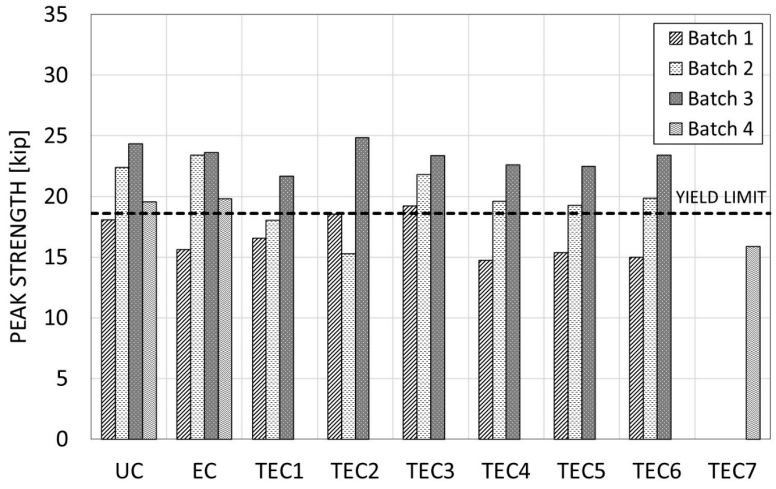

Figure 8. Graph. Comparison of the peak strength of all bar types in the four batches.

In Batch 1, the EC, TEC1, TEC2, and TEC6 specimens failed due to concrete splitting, while the UC, TEC3, TEC4, and TEC5 specimens failed in the pull-out mode. Among the specimens that experienced pull-out failures, only TEC3 exhibited steel yielding, with a peak strength 3.3% greater than the yield limit; UC, TEC4, and TEC5 reached peak strengths 2.8%, 20.9%, and 17.3% lower than the yield strength, respectively. Among the specimens that experienced splitting failures, only TEC2 reached yielding by scarcely surpassing the yield strength magnitude.

In Batch 2, which had the highest concrete compressive strength of all batches, all TEC specimens experienced splitting failures, while UC and EC specimens experienced pull-out failures. This behavior was probably generated by the combination of the effects of the high roughness of the TEC bars with the high strength of concrete, which is more susceptible to splitting failures (Lundgren, 2005). In addition, except for TEC1 and TEC2 specimens, all other specimens experienced yielding of the rebar before failing. Particularly, in the group that surpassed the yield limit, TEC5 exhibited the lowest peak strength corresponding to a value 3.6% higher than the yield strength. Also, even though the smooth surface of EC bars decreases the friction with the surrounding concrete, the specimen using this type of coating was still able to develop a peak strength higher than the rest of the rebars. This strengthened the observation that, between the three components arising on the bars to transfer forces, the bearing action played an essential role in the bond strength.

In Batch 3, where confinement was included, all specimens failed in the pull-out mode. Although micro-splitting was observed in some cases, the CFRP wraps still effectively prevented the splitting failures. All specimens experienced yielding in this batch. Specimen TEC2 had the highest peak strength, whose magnitude was 33.5% higher than the yield strength, while specimen TEC1 had the lowest peak strength, whose magnitude was 16.6% higher than the yield strength.

In Batch 4, UC and EC specimens had roughly the same bond performance, sustaining forces between 5.0% and 6.5% greater than the yield limit, respectively. The average value of the TEC7 specimens was 14.6% lower than the yield limit. However, this result was strongly affected by the behavior

displayed by specimen TEC7-1, whose bond strength was 29.8% lower than the yield limit. In fact, in all cases except that of specimen TEC7-1, yielding of the reinforcing bar occurred before failure.

Based on these results, it could not be concluded whether EC bars possessed higher or lower peak strengths than UC bars. Similarly, TEC rebars did not necessarily seem to improve the peak strength compared to the UC and EC ones. For example, in Batches 1 through 3, TEC5 specimens attained lower peak strengths than their UC and EC counterparts. TEC3 was the only type of bar that experienced steel yielding in the three batches it participated in, which indicated the existence of a strong bond between the rebar and the surrounding concrete. Ultimately, in Batch 4, both TEC7 specimens exhibited lower peak strengths than the UC and EC ones. For example, specimen TEC7-2 showed a reduction of 4.3% and 5.5% with respect to the peak strengths of UC and EC specimens, respectively.

Initial Slip Resistance

Since the transverse cracks observed in bridge decks typically occur at the early stages of construction, when the stress range is significantly lower than the bond strength recorded during the pull-out tests, what influences the development of these cracks is likely the initial slip resistance of the rebars and not their ultimate-state behavior. Therefore, this study also examined the bond-slip performance of the specimens at low levels of slip.

The overall bond-slip curves are illustrated in Figure 9. The truncated curves at the maximum force values are indicative of splitting failures along the reinforcing rebars, as shown, for example, in specimen TEC3 from Batch 2 or specimen EC-2 from Batch 4. In contrast, the large slips occurring after the maximum force was reached are indicative of pull-out failures, as evidenced, for example, in specimen TEC5 from Batch 1 or specimen TEC6 from Batch 3. In Batch 4, the curve corresponding to specimen EC-1 followed the vertical axis due to an error in the acquisition of the free-end slip measurement. Consequently, in this curve, no parameter could be evaluated other than the previously reported maximum force it attained before splitting. Figure 10, in turn, shows a close-up view of the curves to visualize the initial slip resistance of the specimens. Figure 9 and Figure 10 classify the results according to the different concrete mixtures utilized in the experimental program.

A common feature observed in the plots of Figure 10 was that UC and EC bars manifested notably lower initial slip resistance than the TEC bars, which demonstrated that the applied roughness on the surface had a positive impact on increasing the bond as the slip started to develop. Between UC and EC rebars, in most cases, EC specimens exhibited lower slip resistance. From Figure 10-C, it was visible that although the curve of the TEC1 specimen had a higher initial slope, its slip resistance degraded sharply. At a later stage, it featured even lower slip resistance than the UC bars. Apart from Batch 4, the performance of the TEC curves did not show significant differences among each other. However, in the first three batches, they all displayed much higher slip resistance than TEC1, and their degradation took place much later than that of the TEC1 rebars. In Batch 4, specimen TEC7-1 possessed the highest initial slip resistance. Nonetheless, as in the case of TEC1 in the other batches, after reaching the peak load, softening of the force-slip interaction occurred. In general, it is believed that the surface voids on the TEC2 to TEC7 rebars might have served as micro anchorages that helped with increasing the initial bond until the cementitious material filling them was sheared off.

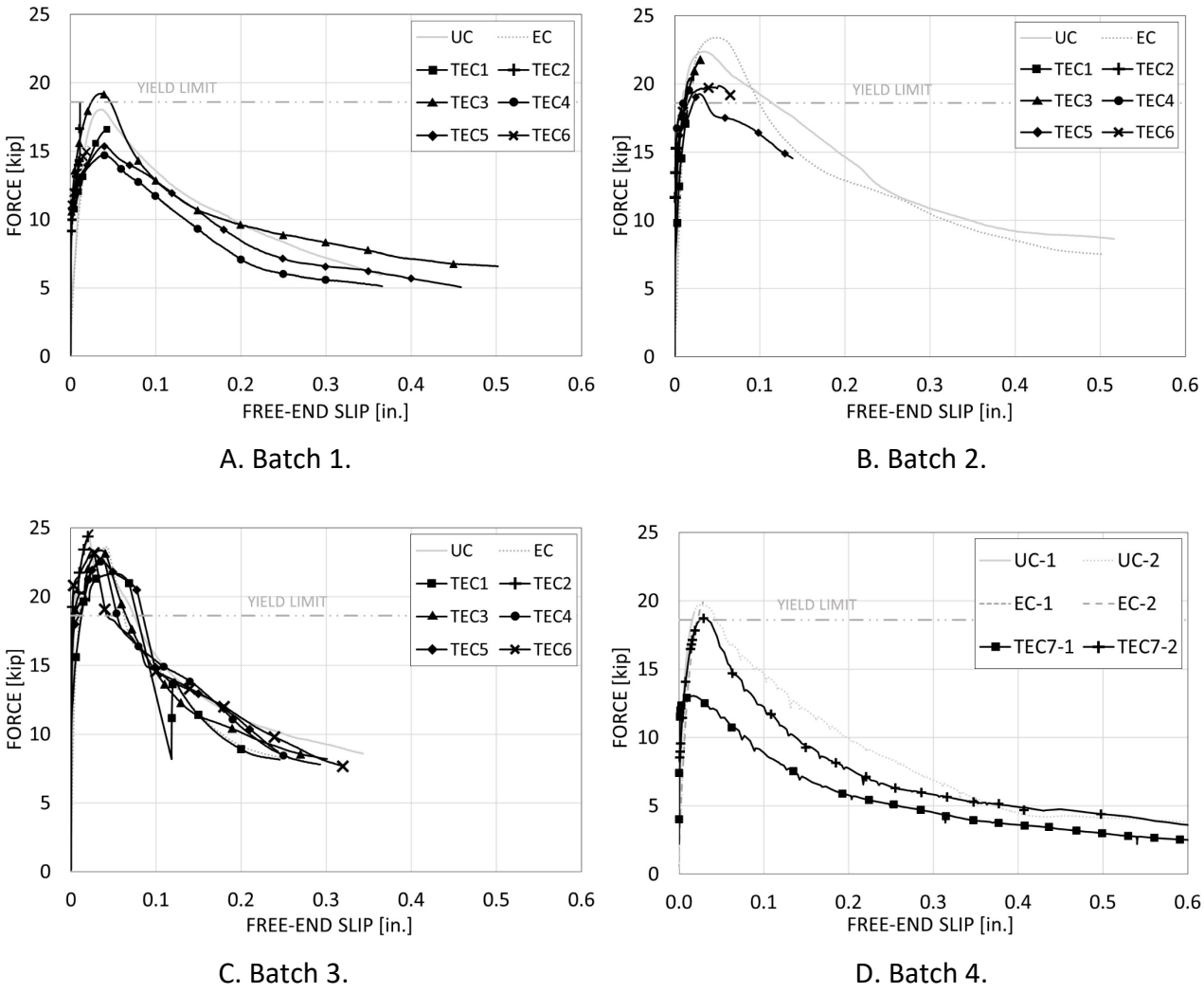

Figure 9. Graph. Overall force-slip curves of specimens according to the different batches studied.

To better quantify the performance of the various bar types, the slip resistance was evaluated by calculating the initial tangent and secant slopes from their force-slip curves. The initial tangent slope is a parameter that represents the stiffness of the concrete-reinforcement anchorage before any significant decrease in the slip resistance takes place; the secant slope represents a more accurate parameter to evaluate the slip resistance when cracks on the bridge decks normally start to appear.

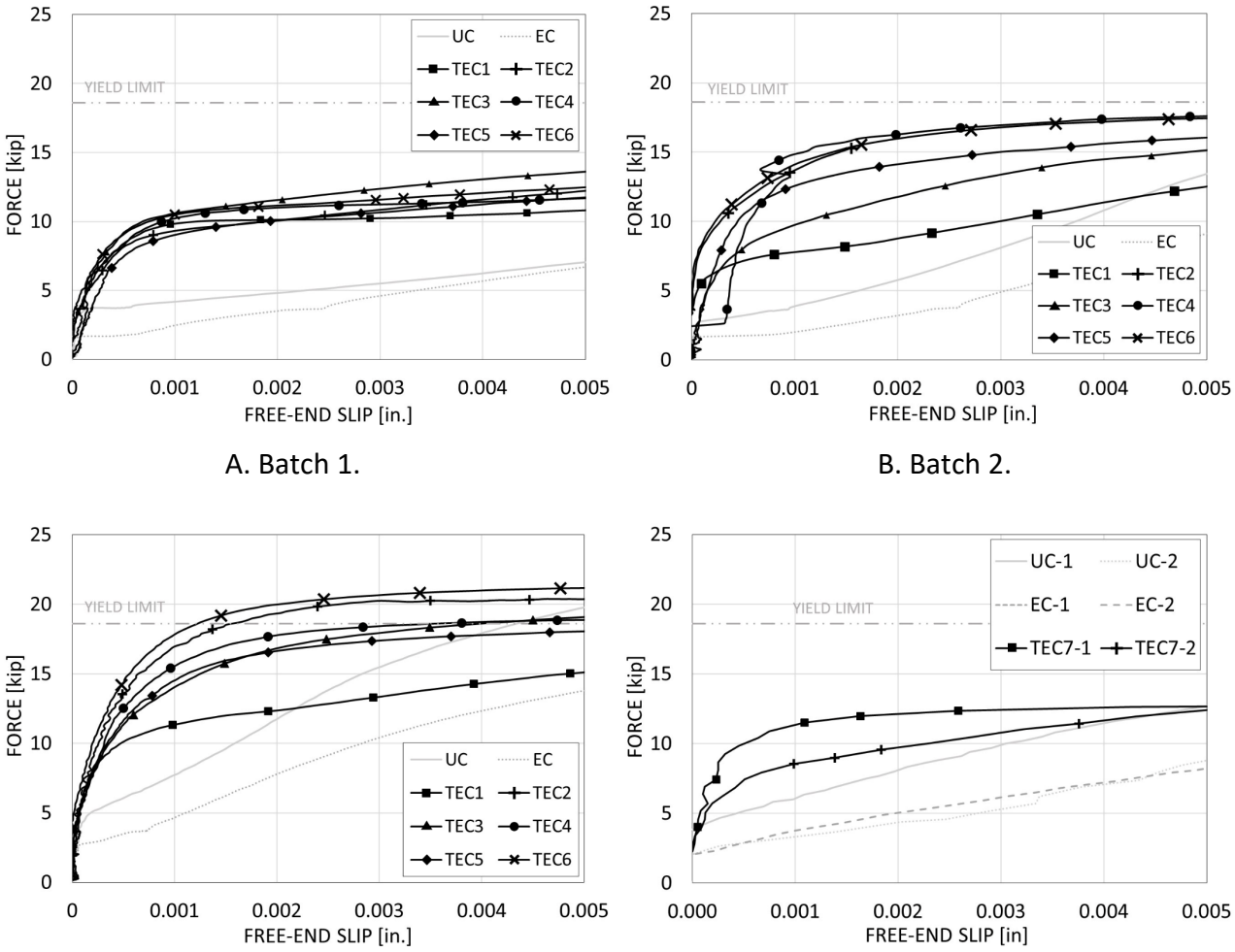

Figure 10. Graph. Initial slip resistance curves of specimens according to the different batches studied.

From a visual observation of the plots in Figure 10, the slope significantly decreased in all batches at a slip less than 0.001 in. (0.0254 mm). Therefore, the initial tangent slope was taken in the interval of 0 in.–0.0001 in. (0 mm–0.0025 mm) for all batches. To determine the secant slope, slip levels of 0 in.–0.0014 in. (0 mm–0.036 mm) were considered. This range of data was based on an investigation of bridge decks carried out by DalSoglio (2017). In his research, the crack spacing and crack width of multiple bridges were quantified. Based on all the measured crack widths, an average value of 473 microstrains was selected as the threshold of the secant slope calculation. Because the length of the bonded region in the pull-out specimens was 3 in. (76.2 mm), the upper bound of the range for the secant slope was determined to be 0.0014 in. (0.036 mm), i.e., the bonded region length multiplied by the strain value. Figure 11 summarizes the results of the initial tangent and secant slopes for the four batches of concrete.

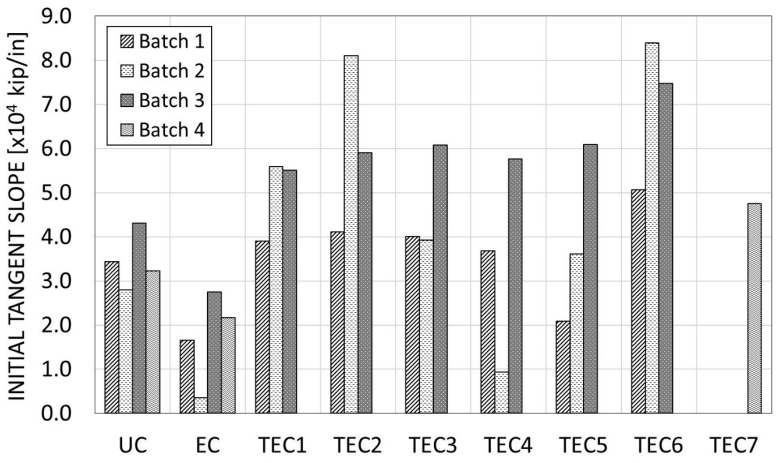

A. Initial tangent slope at 0.0001 in. (0.0025 mm).

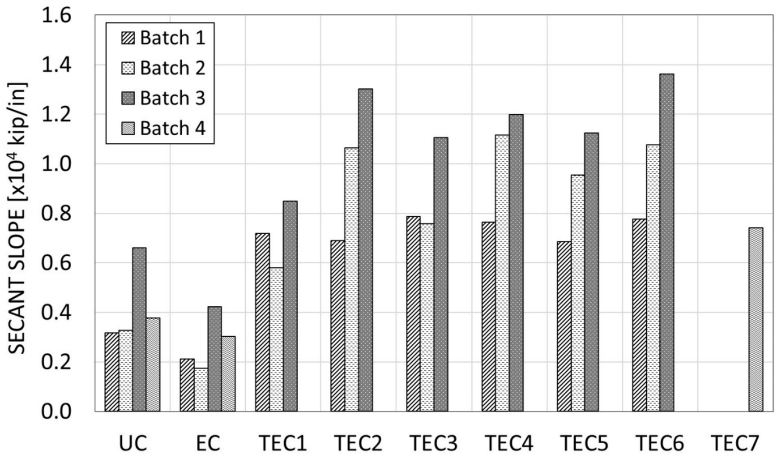

B. Secant slope at 0.0014 in. (0.036 mm).

Figure 11. Graph. Comparison of the slip resistance at different levels of slip.

Overall, Batch 3 showed the highest slip resistance probably due to the application of the CFRP confinement. Furthermore, the slip resistance of the TEC bars was, on average, much higher than those of the UC and EC bars. Also, the earlier observation regarding the rapid slip resistance degradation of specimen TEC1 in Batch 3 could be corroborated in Figure 11, with an 85% reduction between the two stages presented above.

FINITE ELEMENT ANALYSIS

From the results of the roughness measurements and the pull-out tests, the TEC bars showed great potential in improving the bond-slip behavior. However, their bond mechanism at the interfaces between the reinforcement, epoxy coating, and surrounding concrete was not well understood. To obtain a more in-depth insight into the bond mechanism, a numerical finite element (FE) simulation

of the pull-out test was carried out using ABAQUS (Dassault Systèmes Simulia Corp., 2014). The FE model was developed and calibrated using the experimental test results from the TEC6 rebar in Batch 1, which was the TEC bar type with the best bond-slip behavior.

Model Description

The rebar was modeled as accurately as possible to capture the different factors affecting the bond-slip interaction, such as the geometry of the bar ribs, the epoxy coating, and the surrounding concrete next to the bonded region. To reduce the meshing complexity and increase the modeling efficiency, the ribs on the unbonded region were not modeled, and the ribs on the rebar were modeled to have sharp edges instead of the smooth edges as in reality. The geometric properties of the specimen were specified in agreement with the actual pull-out test specimen. Both the steel bar and the concrete were modeled with solid, homogeneous C3D8R elements, while the coating was modeled using C4R shell elements.

The different materials were established based on the models specified hereafter. The ABAQUS concrete damaged plasticity model was adopted to simulate the crushing of concrete between the ribs. The default input parameters were considered. The compressive stress-strain branch was defined by the modified Hognestad model (Hognestad et al., 1955), decreasing the slope of the post-peak descending portion for easier convergence of the model; the tensile stress-strain branch was defined using the splitting tensile strength, as indicated by ACI Committee 318 (2019). For the steel reinforcement, an elastic-plastic model was adopted. Regarding the epoxy coating, the mechanical properties were selected based on typical values from the literature. For example, Xiong et al. (2016) determined the elastic modulus as 600 ksi (4,150 MPa), the yield strength as 1.75 ksi (12MPa), and the Poisson's ratio as 0.31.

To simulate the pull-out force, boundary conditions were placed on the top surface of the concrete to prevent the displacement in all directions without any rotational constraints. A displacement control protocol of 0.0375 in./min (0.95 mm/min), the same as the loading rate of the actual pull-out test, was imposed on the top surface of the rebar.

Interfacial Properties

In the FE model, two interfaces were defined: the interface between the steel substrate and epoxy coating and the interface between the epoxy coating and the surrounding concrete. The bond-slip behavior was not the same for both cases. From the experimental pull-out tests, it was verified that some coating residues were adhered to the concrete, exposing several regions of the uncoated bar, which denoted that the bond between the coating and concrete was stronger. Based on this observation, a stronger bonding strength between the concrete and the epoxy coating was assumed for the FE model.

Cohesive behavior was specified at the coating-concrete and coating-steel interfaces to simulate the bond between those surfaces. The bond strength and debonding failure of the cohesive layers were defined in terms of traction-separation, where each cohesive element was assumed to have a linear initial response until the damage initiation criterion occurs. Then, the material damage developed according to a predefined damage evolution rule. In other words, the damage initiation marked the

beginning of the linear degradation of the cohesive response, and the damage evolution described the rate at which the material stiffness degraded after the point of damage initiation was reached.

Comparison between Experimental and Simulated Results

Figure 12 presents the comparison between the experimental and numerically simulated bond-slip behavior of the TEC6 bar in Batch 1. As indicated earlier, the initial ascending slip resistance is of particular interest because it is associated with the development of transverse cracks at the early stages of bridge construction. At a low level of slip, less than 0.0047 in. (0.12 mm), the simulated force-slip curve closely matched the experimental result; at a higher slip stage, the simulated result started to deviate and diverge.

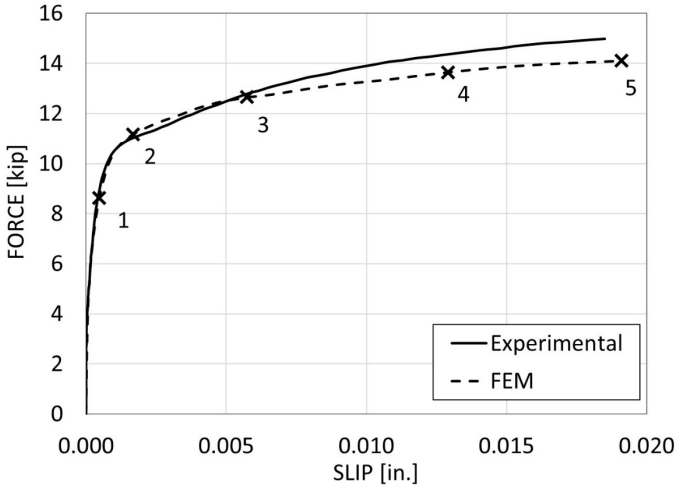

Figure 12. Graph. Experimental and simulated bond-slip curves of TEC6 bar in Batch 1.

By evaluating the FE stress results along the bonded region at a slip of 0.019 in. (0.48 mm), which was close to the slip level just before the splitting failure took place in the experimental test, it was verified that the shear stress was concentrated at the ribs of the rebar and at the lower part of the concrete key between the ribs. This distribution seemed reasonable because as the bar was being pulled out, bearing forces on the ribs resisted the upward movement against the surrounding concrete. Likewise, the axial stress in the rebar decreased towards the bottom end. On the surrounding concrete, the axial stress was concentrated at the upper part of the bonded region and, primarily, around the bar ribs.

Unlike the low levels of stress experienced by the coating of standard EC rebars, the applied surface roughness of the TEC bars subjected the coating to high friction with the concrete that, in turn, developed high levels of stress on it. Figure 13 shows the contour plots of the propagation of the longitudinal stress along the bonded region of the coating at three different slip levels. These points were part of those labeled on the force-slip plot of Figure 12. At point 1, the upper part of the bonded region was subjected to significantly higher stresses than the lower part, and some coating elements had already yielded at this early stage. As the slip increased, the longitudinal stress on the coating started to propagate downwards and an increasing amount of the coating reached yielding, indicating the presence of damage. The stress was also primarily concentrated on the bar ribs. The top face of

the ribs was first subjected to compressive stresses at the early stages of the simulation but, as the pull-out action progressed, the stress on the ribs became tensile. This can be exemplified by tracking the change in the longitudinal stress of the element pointed out in Figure 13-A. It evolved from −1.62 ksi (−11.17 MPa), −0.67 ksi (−4.62 MPa), and 1.89 ksi (13.04 MPa) at points 1, 3, and 5, respectively. Furthermore, the horizontal splitting stress in the concrete initiated at the region close to the bonded region and propagated outwards. Again, before the splitting occurred, higher stresses were concentrated on the ribs in comparison to the region between the ribs. At this same point, the splitting stress at the edge of the concrete specimen reached the concrete tensile capacity, indicating the rupture of the material, which matched with the experimental observation.

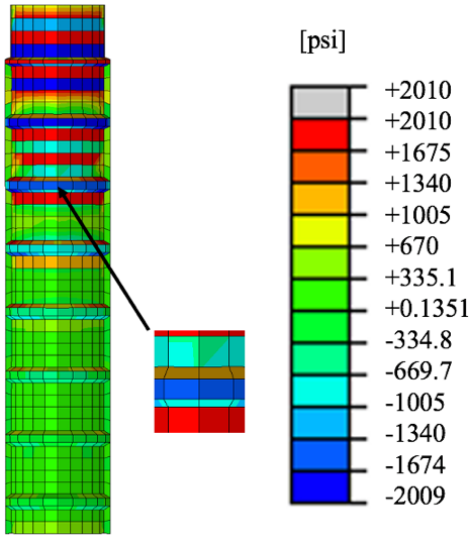

A. Point 1: Slip = 4.69×10-4 in. (0.01 mm), Force = 8.62 kip (38.34 kN)

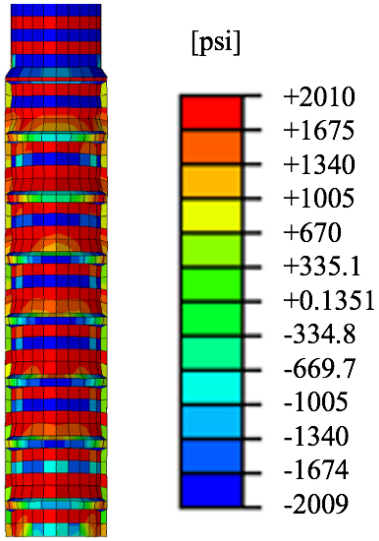

B. Point 3: Slip = 5.74×10-3 in. (0.15 mm), Force = 12.65 kip (56.26 kN)

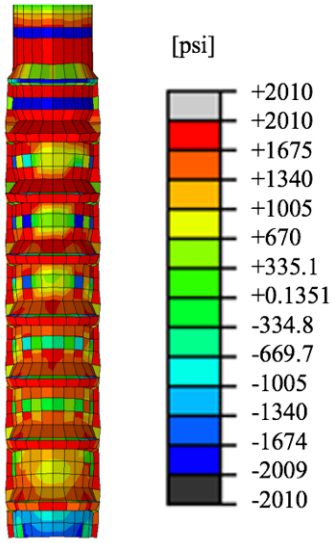

C. Point 5: Slip = 0.019 in. (0.49 mm), Force = 14.11 kip (62.76 kN)

Figure 13. Graph. Deformed contour plots for the longitudinal stress on the coating along the bonded region at different slip levels.

CHAPTER 4: DESIGN AND FABRICATION OF LARGE-SCALE SPECIMENS

MATERIALS

This section describes the principal characteristics of the steel reinforcing bars, concrete mixture, and structural steel section composing the large-scale bridge deck specimens built for this part of the experimental program.

Steel Reinforcing Bars

The steel reinforcing bars employed were provided by IDOT. They were used in the "as-delivered" condition, meaning that, for the corresponding cases, the epoxy coating was previously applied to the uncoated elements. The batch consisted of No. 5 rebars, manufactured according to ASTM A706/A706M-16 (ASTM, 2016), designated as Grade 60, and cut in 18 ft (5.49 m) pieces. They did not belong necessarily to the same heat of steel. The spiral deformation pattern was the same for all the bars, forming an angle of 60° with their longitudinal axis.

As mentioned earlier, TEC7 rebars were manufactured based on the advantageous characteristics exhibited by the former TEC2, TEC3, and TEC6 bars. Thus, one of the laboratory specimens incorporated this type of coated rebar. The other twin specimen incorporated standard epoxy-coated bars because it was desired to compare the performance between the new and the traditional coating protection system. Figure 14 presents the appearance of both types of reinforcing bars.

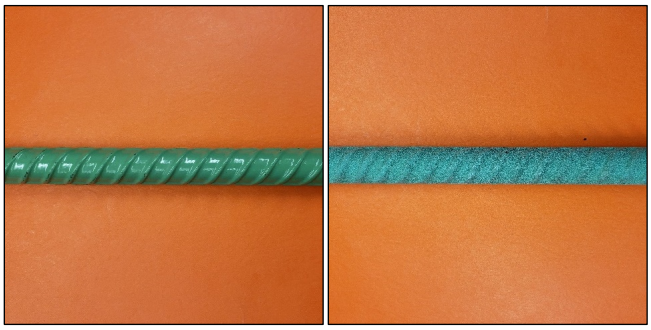

A. EC rebar. B. TEC7 rebar.

Figure 14. Photo. Surface appearance of the No. 5 steel reinforcing bars used in the large-scale bridge deck specimens.

Figure 14 illustrated the noticeable differences between EC and TEC7 elements. The former is glossy and smooth, while the latter is opaque and granular. Also, in TEC7 rebars, the coating tends to build up on the bearing face of the rib, which results in rib face angles smaller than the nominal ones.

Concrete

The specimens were cast using an approved IDOT class BS concrete mixture, whose detailed design criterion, extracted from IDOT's *Standard Specifications for Road and Bridge Construction* (2016), is shown in Table 2. This class of concrete is intended for bridge decks and other bridge superstructure elements.

Table 2. Concrete IDOT Class BS Design Criteria

Cement factor	Water/Cement ratio	Slump	Air content	Minimum compressive strength at 14 days
605–705 lb/CY (358–418 kg/m^3)	0.32–0.44	2.0–4.0 in. (50.8 –101.6 mm)	5.0%–8.0%	4,000 psi (27.58 MPa)

The concrete mixture was provided by Prairie Material, a ready-mix concrete supplier, and its specific proportions are summarized in Table 3. As defined in Section 1020.05 of IDOT's *Standard Specifications for Road and Bridge Construction* (2016), more than one supplementary finely divided mineral can be added to this type of mixture. Therefore, in this case, the weight of fly ash should be considered as a part of the cementitious materials. In addition, the weights presented for the fine and coarse aggregates correspond to a saturated surface dry condition. Regarding the mixture workability, IDOT allows the inclusion of high-range water-reducing admixtures to improve the workability by increasing the slump to even 7.0 in. (177.8 mm) after adding this component (IDOT, 2016). However, this was not used when casting the specimens.

Table 3. Concrete IDOT BS Mixture Proportions

	Quantity per m^3	Quantity per CY
Fine aggregate (natural sand, gradation 01)	717 kg	1,209 lb
Coarse aggregate (crushed stone, gradation 11)	807 kg	1,360 lb
Coarse aggregate (crushed stone, gradation 16)	269 kg	453 lb
ASTM C 150 Type I Portland cement	273 kg	460 lb
Fly ash	91 kg	153 lb
Water	146 kg (146 L)	246 lb (29.5 gal)
Water/Cement ratio	0.40	
Aggregate air content correction factor	0.40%	
Total batch weight	2,303 kg	3,882 lb

To verify that the delivered hydraulic-cement concrete mixture satisfied the design criteria, different tests were performed on a representative sample as part of the quality control program. This sample was obtained as stipulated by ASTM C172/C172M-17 (ASTM, 2017a). The slump, air content, and temperature of the concrete mixture were determined according to ASTM C143/C143M-20 (ASTM, 2020c), ASTM C231/C231M-17a (ASTM, 2017b), and ASTM C1064/C1064M-17 (ASTM, 2017c), respectively. Regarding the strength test, ACI Committee 318 (2019) indicates cylinders to be tested at the age of 28 days. However, in this experimental program, it was stipulated to monitor the

strength also at the ages of 7 and 14 days. The 7-day result provided insight regarding the early strength gain, while the 14-day result was the direct comparison to the class BS concrete mixture criteria established by IDOT, as shown previously in Table 2. The procedure established by ASTM C31/C31M-19a (ASTM, 2019a) was followed to make the cylinder samples, choosing the standard method of curing. Thus, specimens were initially cured for 38 hours, at 68°F (20°C), covering them with a plastic lid to prevent the loss of moisture; the final curing, after removing the molds, took place in a moist room complying with ASTM C511-19 (ASTM, 2019b). Finally, the compressive strength of the cylindrical concrete specimens was determined as specified in ASTM C39/C39M-20 (ASTM, 2020d), using an unbonded capping system.

Table 4 summarizes the results of the previous test. The results proved that the mixture met the target parameters established in the IDOT criteria, cited in Table 2.

Table 4. Summary of the Test Results Performed On-site

Slump	Air content	Temperature	Average compressive strength		
			7-day old	14-day old	28-day old
3.75 in. (95.0 mm)	5.30%	63.0°F (17.0°C)	5,680 psi (39.20 MPa)	6,560 psi (45.20 MPa)	7,250 psi (50.0 MPa)

Structural Steel

A W-shape section was utilized as the steel girder of the large-scale specimens' composite section. It was made out of a high-strength, low-alloy steel type, according to ASTM A992/A992M-20 (ASTM, 2020b) designation.

SPECIMEN DESCRIPTIONS

As mentioned before, two large-scale specimens were built using the materials described above, keeping the coating type as their only discrepancy. Each specimen was designed to emulate a composite section of a bridge deck and supporting steel girder belonging to a positive moment region. The concrete cross-section possessed a depth of 8.0 in. (0.20 m) and a width of 50.0 in. (1.27 m), which was calculated as the effective flange width of the composite deck according to AASHTO (2017) specifications. The length of each deck was 199.0 in. (5.05 m) so that the resulting aspect ratio would be approximately 4:1. This geometry was chosen to trigger the occurrence of the shrinkage and thermal effects primarily along the longitudinal direction of the concrete element. Regarding the steel section, plate girders used in similar bridges have approximately 14 in. wide (0.35 m) flanges and 48 in. deep (1.21 m) webs. However, in this laboratory model, it was considered unnecessary to incorporate an element with that height. Instead, a W14 × 90 shape was selected, which has approximately the same width but a shorter depth. This provided a similar contact area with the concrete and enough space to install the shear connector studs. Figure 15 shows the typical cross-section of the specimens, defining the element's dimensions and the distribution of reinforcement accordingly. The detailing is based on a representative bridge of the state of Illinois.

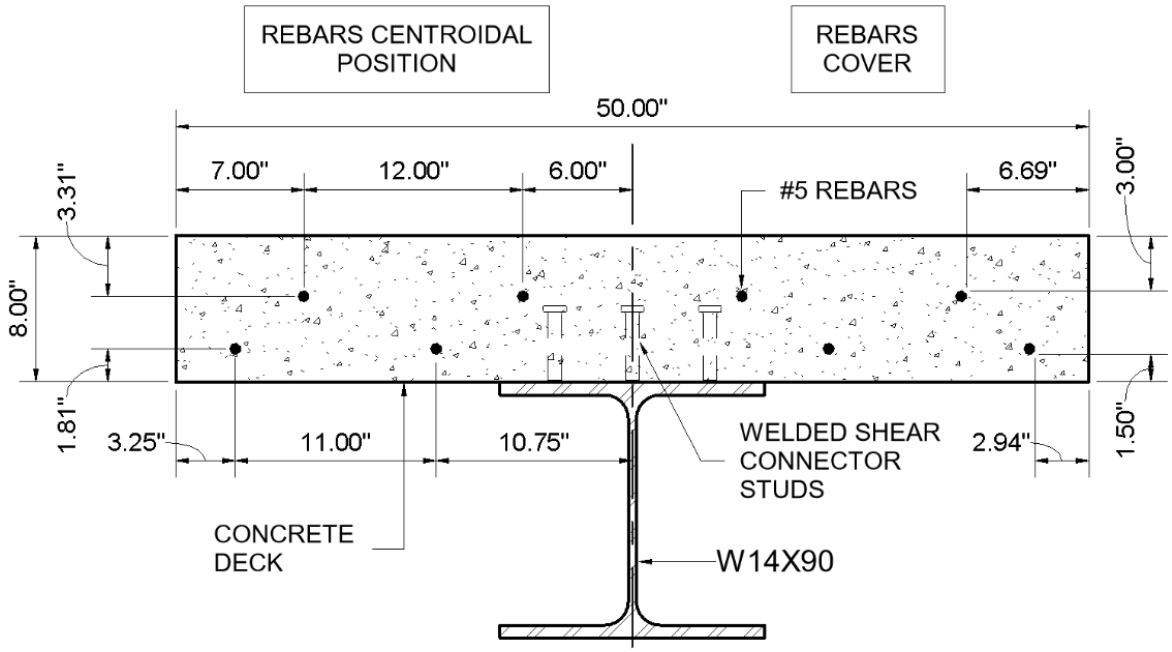

Figure 15. Illustration. Specimens' cross-section detail.

No. 5 rebars are one of the most typically used reinforcement in bridge decks. Thus, each specimen contained eight No. 5 reinforcing bars, non-spliced, distributed in two layers throughout its depth, of four rebars each. The spacing of the top layer of reinforcement was 12 in. (0.30 m), and that of the bottom layer was 11 in. (0.28 m). The cover-to-bar diameter ratio was 4.8 for the top surface, 2.4 for the bottom surface, and 10.7 and 4.7 for the sides with respect to the top and bottom layers, correspondingly. No transverse reinforcement was included.

Figure 16 shows the typical plan view of each specimen, defining primarily the type and distribution of the welded shear connector studs along the steel girder. The position of the studs was established to restrain both ends of the deck. Therefore, no connectors were installed in the middle third of the specimens so that the shear lag, or transfer of stress in compression across the section, could be developed between the two arrays. Also, this helped to avoid the intervention in bond behavior of any factor other than the type of coating. In actual structural designs, the spacing and number of studs vary according to the degree of composite action needed to overcome the demands developed on the different regions of the members. For this case, each array consisted of five lines of studs, 15 in. (0.38 m) apart from each other. Each line, in turn, was comprised of three shear connectors.

Additionally, each specimen possessed two 99 in. long (2.51 m) L8" × 8" × 1/2" steel angles, each one connected to the steel girder using two 1 in. diameter (25.4 mm) bolts at both ends. They were in charge of constraining the movement of the rebars inside the concrete deck.

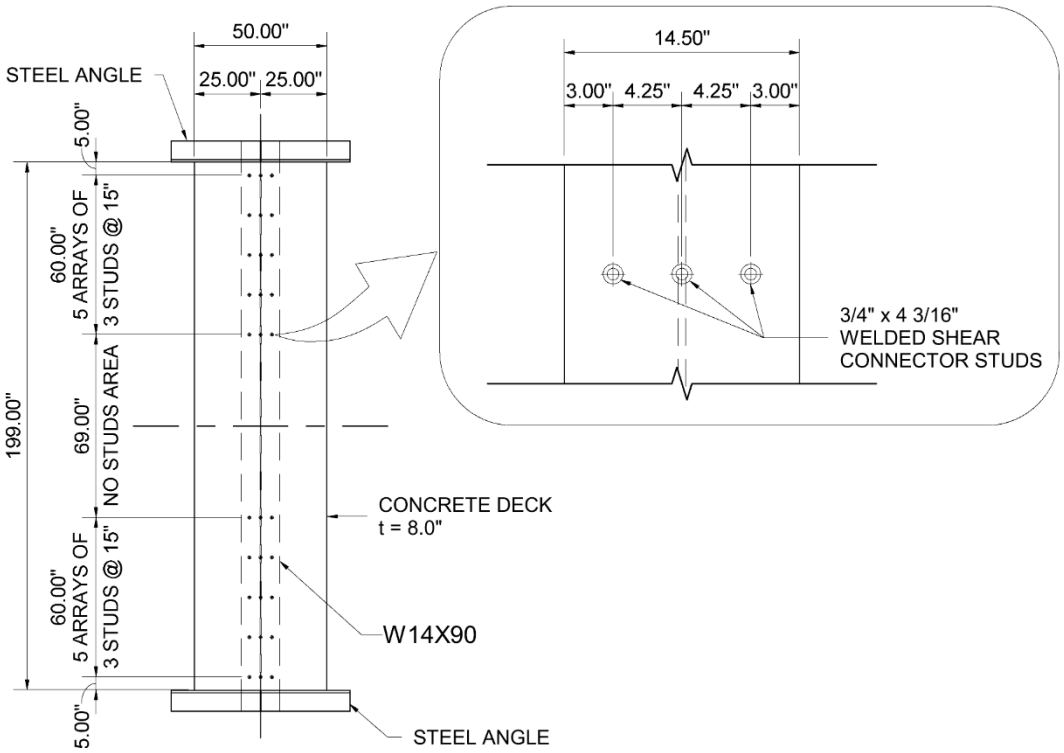

Figure 16. Illustration. Specimens' plan view detail.

The construction of the specimens, according to the previously described dimensions and characteristics, took place in the Newmark Structural Engineering Laboratory facilities at the University of Illinois Urbana-Champaign. To start, the shear connector studs were welded to the wide-flange section. Soon after, the steel angles were bolted at both ends of the girder, and the assemble was positioned over the supports that were decided to be used on the first tests, as will be elaborated in the next chapters. Then, the formworks for the concrete decks were constructed around the metal frames. For this task, 2 × 4 in. (51 × 102 mm) lumbers were used as the horizontal and vertical elements of the primary structure in charge of resisting the weight of the concrete to be poured. This stage of the process is shown, representatively, in Figure 17-A. Also, 3/4 in. thick (19.1 mm) plywood sheets were added as the bottom and lateral faces that contained the fresh mixture. Once everything was firmly assembled, the joints between the different elements that were to have contact with the concrete mixture were sealed using silicone-based caulk.

The next step was to place the rebars in their corresponding position. The L8″ × 8″ × 1/2″ steel angles had 3/4 in. (19.1 mm) holes predrilled according to the distribution of the reinforcement shown in Figure 15. Therefore, the 18 ft long (5.49 m) EC and TEC7 elements were inserted through those holes until they extended 8 in. (0.20 m) outside of both angles, as is shown in Figure 17-B. This simulated the continuity of the reinforcement beyond the edges of the concrete decks. To prevent the rebars from sliding back and forth, each of them was manually fastened with a lock collar on the outer face of the angle members. Later, the lock collars were glued to the metal surface using commercial epoxy to prevent the bars from rotating about their longitudinal axis.

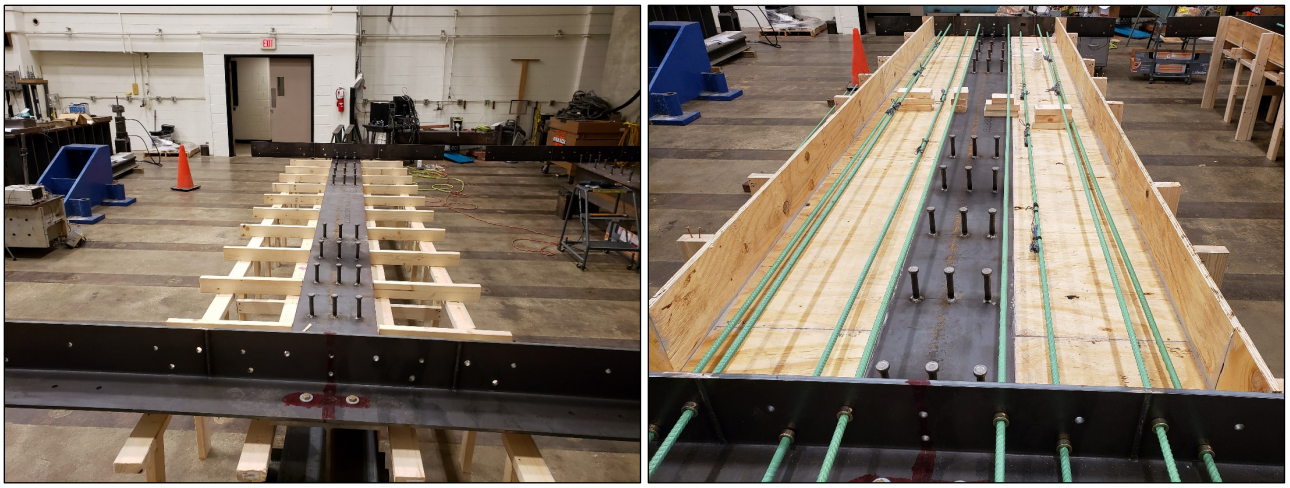

A. Primary supporting frame of the formwork. B. Steel rebars installed on the specimen.

Figure 17. Photo. Installation of formwork and reinforcement in the large-scale bridge deck specimens.

Although the correct position of the reinforcement was ensured at both ends of the specimens by the steel angles, the rebars exhibited deflections and misalignments in the interior. Placing support objects, such as plastic chairs, was not desired because the volume they occupy could have affected the experimental results. Hence, it was decided to preserve the alignment of the steel bars using a method that involved minimal inclusion of foreign materials. Under these circumstances, nylon thread was utilized at some points in the transverse direction of the specimens to hold the rebars. The thread was wrapped around each reinforcing bar, and both ends of it were tied on a screw installed on the vertical wood members that supported the lateral formwork, as shown in Figure 18-A. The position of the rebars was then controlled by tightening or loosening the nylon thread, which was regulated by rotating the screws, similar to the mechanism of a winch in a well. The threads were tightened until the bars were straight, as shown in Figure 18-B.

Before casting, the appearance of the reinforcement was clean and free of harmful foreign materials, as stipulated in Section 26.6.1.2 of ACI 318-19. Also, the coating did not present signs of damage or surface imperfections. Both specimens were cast in a single activity, using the same batch of class BS concrete described before. The truck mixer discharged the fresh concrete into a metal container that was dragged with the laboratory moving bridge crane over the specimens to be released, as shown in Figure 18-C. However, before starting to fill the container, a preliminary slump test was made to check the initial workability of the mixture. The result was satisfactory, falling within the limits for this type of concrete. Once the mixture was released over the specimens' formworks, it was consolidated with mechanical vibrators. The surface was leveled with a straight metal screed that was ridden along the top edges of the forms, and two hours after the concrete was cast, the surface received a typical troweled finishing, as shown in Figure 18-D.

A. Wrapping nylon thread around rebars and end screw. B. Rebars after being straightened.

C. Releasing concrete mixture from metal container over specimens. D. Finishing specimens' surface.

Figure 18. Photo. Representative steps of the fabrication of the large-scale bridge deck specimens.

Approximately 30 minutes after the finishing concluded, both specimens were covered with a plastic lid to control the loss of moisture and start their initial curing process, as shown in Figure 19-A. Because both decks were in the laboratory facilities, they were protected from direct sunlight, and the ambient temperature remained constant at 68°F (20°C). The initial curing period lasted one and a half days since the surfaces needed to be prepared as soon as possible to start the instrumentation of the first part of the experimental program. The final curing process was accomplished under the same conditions provided in the laboratory.

The removal of the formwork was performed in two stages. In the first stage, 3 days after casting, the lateral pieces were disassembled from the wood framework. The time when the second stage took place was determined to ensure that the developed strength of the concrete would be sufficient to

prescind of the support the props provided. This stage occurred 7 days after casting, and it comprised the complete removal of the remaining parts of the formwork, as shown in Figure 19-B.

A. Specimens covered with a plastic lid.

B. Specimens after the formwork was completely removed.

Figure 19. Photo. Curing and formwork removal of the specimens.

CHAPTER 5: SHRINKAGE TESTS

Shrinkage is the decrease in either length or volume of a material resulting from chemical and moisture content changes (ACI-CT, 2020). In concrete, as ACI Committee 209 (2005) explained, shrinkage generates strains even though specimens are load-free, but it does not include changes arising from temperature variations. Autogenous shrinkage is the term associated with chemical interactions. It occurs in the absence of moisture exchange due to the hydration reactions taking place inside the cement matrix (ACI Committee 209, 2005). Drying shrinkage, in turn, is the term associated with the loss of moisture. It occurs when the specimen is exposed to the environment and allowed to dry, and it involves moisture movement through the material and moisture loss (ACI Committee 209, 2005). Figure 20 illustrates both components of the full shrinkage process.

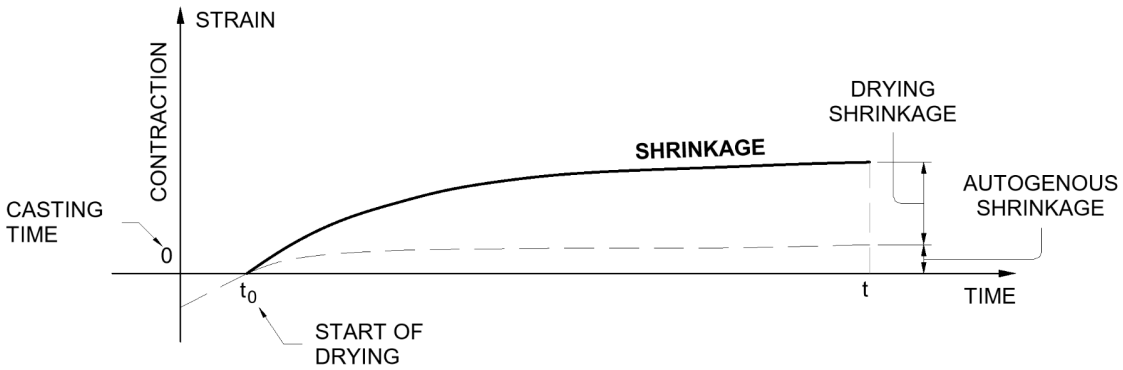

Figure 20. Illustration. Strain-time relationship of a load-free hardened concrete specimen.

(Adapted from ACI Committee 209, 2005).

Figure 20 shows the strain attributable to shrinkage increases with time. Additionally, drying shrinkage begins when the concrete settles and starts to harden, while autogenous shrinkage begins even before drying. For normal-strength concretes, such as the mixture used to build the specimens of this research, autogenous shrinkage can be considered negligible. As ACI Committee 209 (2008) stated, in most cases, it does not exceed 150 microstrains. However, for concretes with water-cement ratios less than 0.4, mean compressive strengths greater than 8,700 psi (60 MPa), or both, autogenous shrinkage may be a major component of the shrinkage strain (ACI Committee 209, 2008). In these situations, it has been proved that its magnitude could be almost the same as that of the drying shrinkage (Tazawa & Miyazawa, 1995).

In reinforced concrete members, rebars resist shrinkage. As a result, small, neighboring cracks are likely to develop around them. These cracks can act as stress raisers and points of crack initiation at the bar ribs at relatively low loads (ACI Committee 408, 2003). Full-depth cracks can also develop when flexural members are restrained at the supports, where shrinkage causes a buildup of tension in the member, in addition to the bending caused by the external loads (Gilbert, 1992). Based on this, this test was intended to monitor and compare the changes in strain and potential cracks exhibited by both specimens while they were allowed to dry after their initial curing concluded. This helped to exemplify the impact that the bar roughness would have on the long-term shrinkage in bridge decks.

The monitoring period consisted of 66 days, divided into three segments. The first period began when the paint on the deck surface required for the digital image correlation (DIC) implementation was completed, as will be explained later in this chapter. This occurred 4 days after the initial curing stopped and lasted one and a half days, up until the formwork was completely detached. The second period started at that moment. It lasted 5 days and comprised the time spent installing the strain-gauge instrumentation on the bottom surface of the decks. For this activity, wood props were placed at both sides of the steel angles as a measure of precaution against any instability. The final period began after the wood props were removed and consisted of 59 days. This period concluded when no significant variations were furthered observed in the strain.

TEST SETUP

For these tests, the W-shape section was supported on one end by a steel block and on the opposite end by a steel rod, simulating a partially fixed-roller boundary condition. Figure 21 illustrates the lateral elevation view of each specimen.

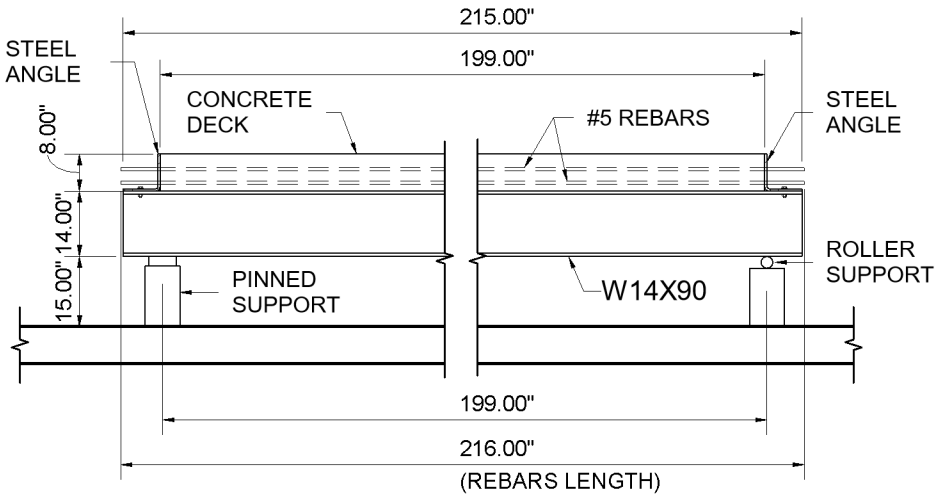

Figure 21. Illustration. Specimens' elevation view detail.

Instrumentation

The two instrumentation strategies implemented for measuring the strain in these tests were digital image correlation and strain gauges.

Digital Image Correlation

Different studies, such as the ones conducted by Salmanpour and Mojsilovic (2013) or Gencturk et al. (2014), monitored the strain in large-scale specimens using 2D DIC. Contrary to conventional strain gauges that measure strains at discrete locations, this noncontact technology allows the generation of fields that can be illustrated by comprehensive contour diagrams. In this test, this resource was implemented for recording the development of the strain at the top surface of both large-scale specimens.

In essence, DIC requires the application of a speckle pattern over the planar region to be studied. After that, a set of photographs of that region should be taken, keeping the position of the camera stationary and at a constant distance from the visual sensor as the test of interest develops. As stated by Correlated Solutions, Inc. (2020a), this technique works by tracking, throughout the input set of pictures, the patterned dots included in a mesh of small subsets as they change by the movements and deformations the specimen experiences.

Two Nikon D90 cameras were used to capture the photographs. This model has a resolution of 12.3 megapixels equivalent to 4288 × 2848 pixel-size pictures. The aspect ratio of 3:2 was the basis to determine the target area of interest. By considering the width of the decks as the short side, the length of the region resulted in 75 in. (1.91 m), as illustrated in Figure 22.

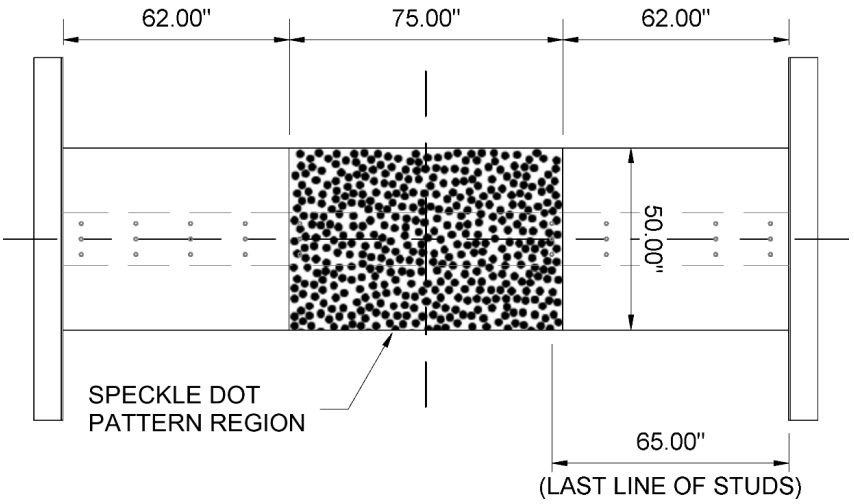

Figure 22. Illustration. Region of interest for DIC analysis.

To keep the camera lenses looking down at the specimens during the photograph acquisition period, an instrumentation frame was assembled. It comprised one column, one beam, and two supporting plates. The supporting plates were in charge of holding the cameras above the middle point of both the transverse and longitudinal directions of the specimens. The diagram of the instrumentation arrangement is illustrated in Figure 23-A, and the final setup is shown in Figure 23-B.

Before the acquisition period began, it was decided to capture photographs twice a day per specimen. Hence, during the 66 days of the monitoring period, one picture was taken at 9:30 a.m. and the other one at 9:30 p.m. To post-process the series of photographs taken to the specimens, the software VIC-2D, version 6.2.0, developed by Correlated Solutions Inc. was used.

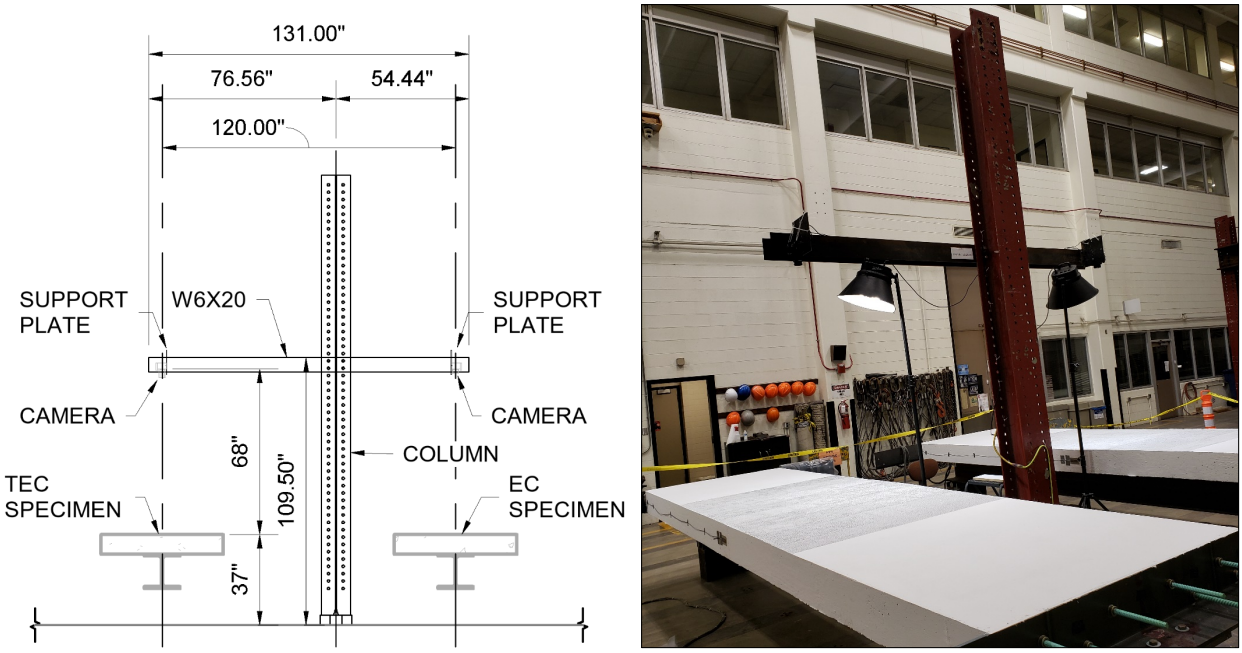

A. Elevation view diagram.

B. On-site assembly.

Figure 23. Illustration and photo. Instrumentation frame built for the DIC acquisition technique.

Strain Gauges

Besides DIC, strain gauges were also employed in this test to monitor the strain developed at some points along the reinforcing steel bars and the bottom of the concrete decks. Tokyo Sokki Kenkyujo Co., Ltd. devices were utilized and installed as specified by the provider's instructions. For the steel rebars, strain gauges type FLA-6-11-5LJCT were used, installing them by applying CN adhesive as the fixing component, and SB tape and Epoweld 8173 as the humidity and shock protective coatings, respectively. For the concrete surfaces, strain gauges type PL-60-11-5LJCT-F were used, installing them by applying epoxy resin and CN-E strain gauge adhesive as the surface leveling and fixing component, respectively.

Each specimen contained 10 steel strain gauges and 10 concrete strain gauges distributed to capture a general depiction of the changes in the strain happening in roughly the middle half of them, where most longitudinal shrinkage was expected. The location of each device with its general nomenclature is shown, for the rebars, in Figure 24, and for concrete, in Figure 25. It is common for concrete strain gauges to be generally installed on the top of the elements to facilitate instrumentation and observation. However, in this case, they were only installed on the bottom and long-lateral surfaces to avoid disturbing the pictures that the cameras were going to be capturing for the DIC analysis.

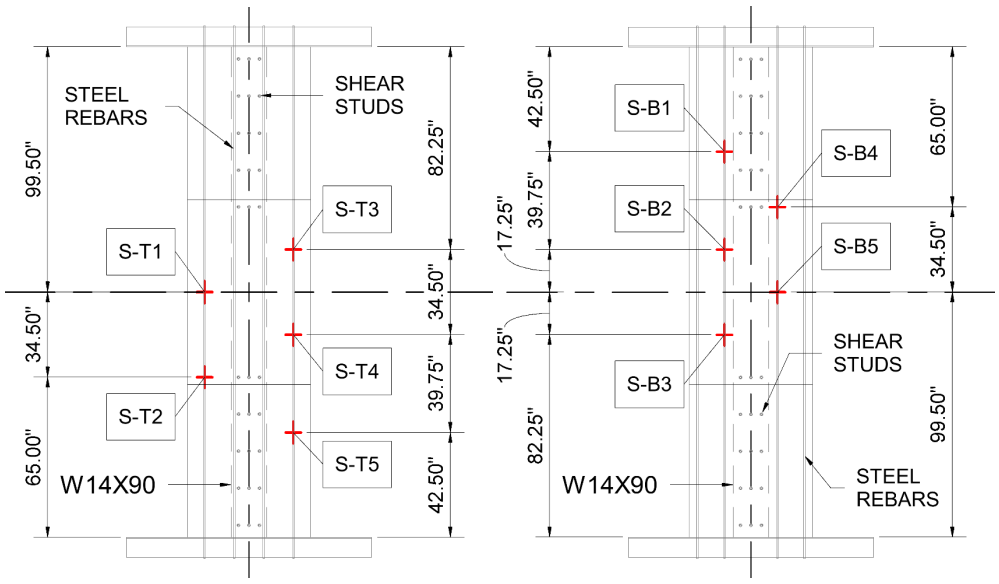

A. Top layer of rebars. B. Bottom layer of rebars.

Figure 24. Illustrations. Strain gauges installed on both layers of the steel reinforcing bars.

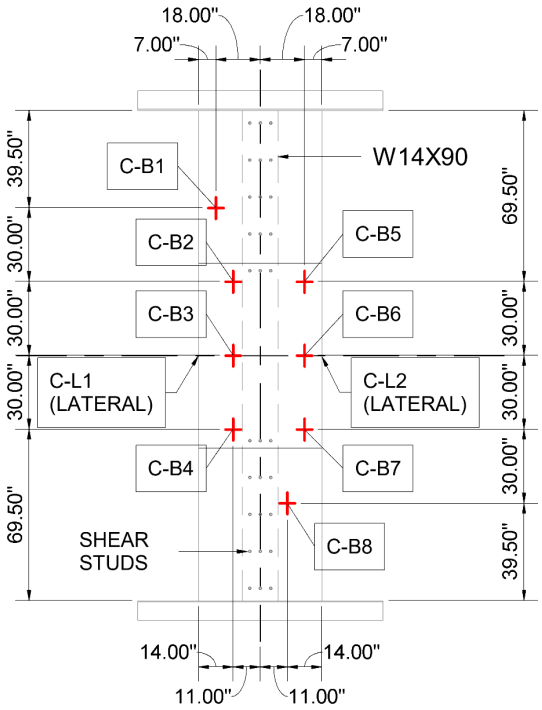

Figure 25. Illustration. Strain gauges installed on the bottom and side surfaces of the concrete decks.

The measurements provided by the strain gauges were recorded by an assembly of hardware manufactured by National Instruments Corp. This equipment consisted of the main chassis and a set of input modules and front-mounting terminal blocks. The data was stored and displayed using SignalExpress 2015, version 15.0.0.

TEST RESULTS

A total of 129 pictures were taken since the speckle dot pattern was applied on the surface of the specimens, five days after casting. The photographs were referenced as shown in Figure 26.

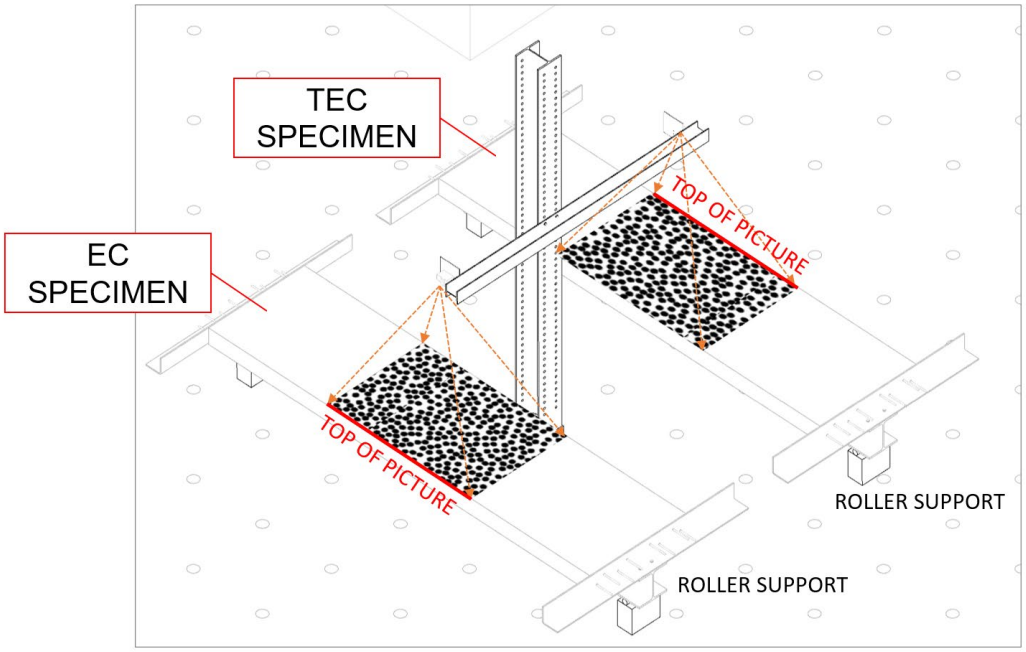

Figure 26. Illustration. Reference of DIC photographs in both specimens.

The complete set of pictures was divided into three periods. The final strain distribution that occurred in the speckle dot region at the end of the last shrinkage monitoring stage is shown for both specimens in Figure 27. In addition, the detailed progression of the strain at this stage is presented in Appendix A. The longitudinal strain, ε_{xx}, is reported in the figures because, based on the aspect ratio of the decks, major changes were expected in that direction in particular. Microstrains, calculated as the value of strain times 10^6, were the units adopted for the plots and contour diagrams. The positive values were associated with tension, while negative values were with compression.

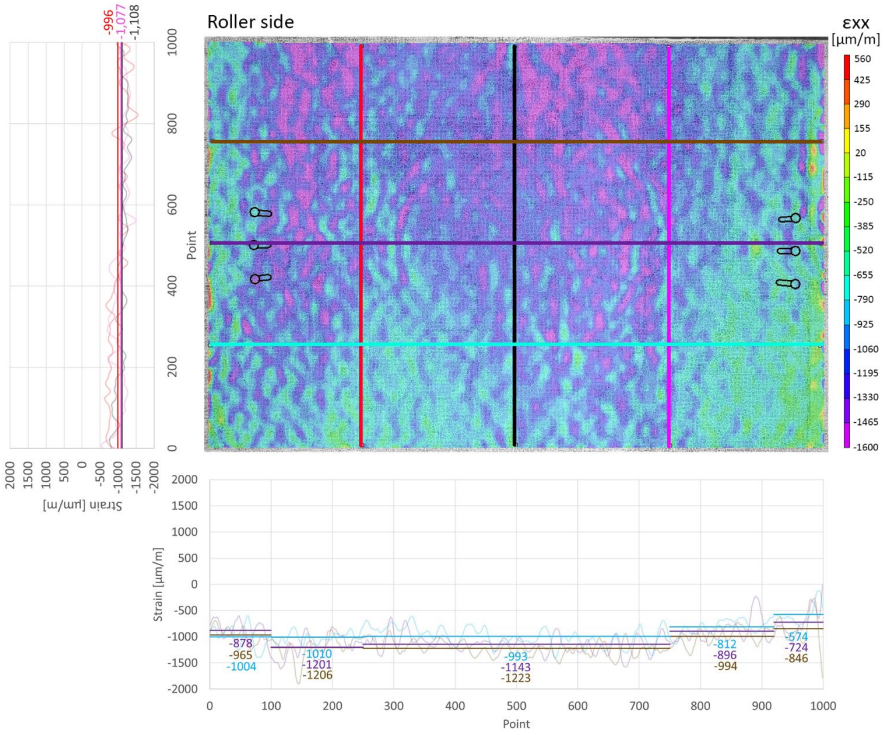

A. EC specimen.

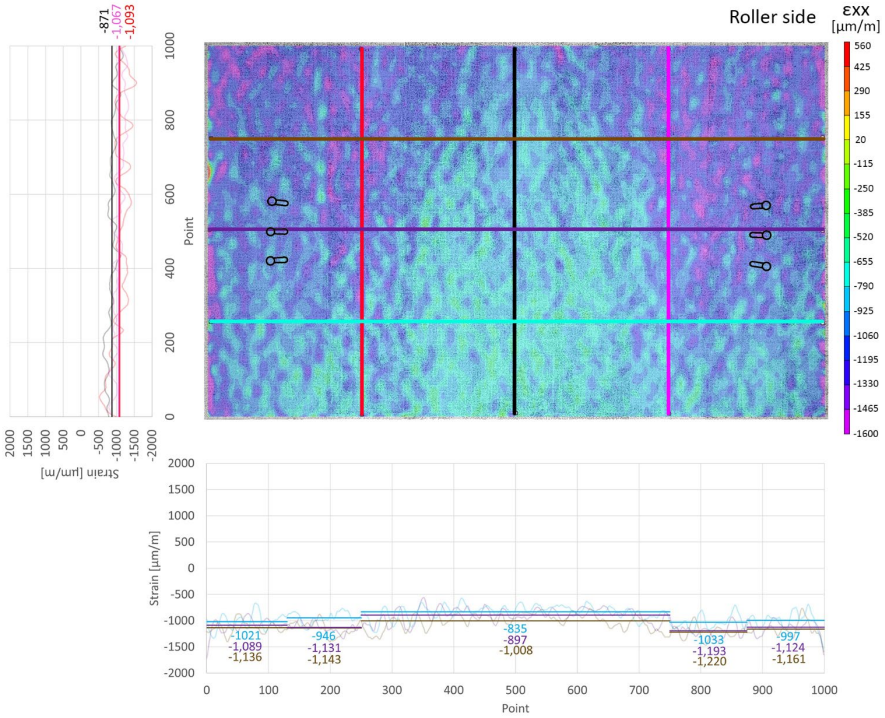

B. TEC specimen.

Figure 27. Illustration. Final strain distribution of specimens in DIC stage 3.

The previous images included the first rows of shear connector studs as seen from the perspective of the cameras. They were referenced using pictures taken from the instrumentation frame prior to casting the concrete. In addition, a total of six straight lines—three vertical and three horizontal—each made out of a thousand points and different colors, were incorporated within the photographs. The strain values that coincided with these lines were illustrated, according to their color code, in the plots that accompany every picture at its bottom and left sides. Precisely, the left plot showed the results for the vertical lines and the bottom one for the horizontal lines. The dimly colored curves of the plots corresponded to the magnitude of ε_{xx} obtained from the DIC analysis, while the dark, solid delineations represented the average of those values. As witnessed from the figures, the vertical and horizontal lines were positioned over each photograph such that they approximately divide their length and width into quarters. This was intended to create a general description of the shrinkage behavior of the specimens in their middle region, where the action coming from the shear connectors was interrupted and the effects of the coating on the bond behavior mainly influenced the development of strain. Because the horizontal lines intercepted areas where significant changes were expected, it was deemed appropriate to split them into segments and calculate the averages individually. Thus, the first range comprised the middle 50% of the picture, the second range represented the values outside the first range until reaching the first row of studs, while the third range was for the values outside the second range until reaching the edge of the image. Likewise, the scale located at the right side of the contour plots was established according to the envelope of all the values reported by the DIC analysis on both specimens throughout the entire monitoring period.

The results shown in Figure 27 were not symmetric as logically expected. This could be due to deviations on the rebars at the time of casting, small differences in the alignment of the cameras with respect to the horizontal surface of the decks, or irregularities on the concrete surfaces that slightly changed the distance from the camera to the area of interest. As Correlated Solutions, Inc. (2020b) stated, accurate 2D correlation depends on the specimen being planar and parallel to the camera sensor. However, overall, a clear difference was perceived between both specimens.

In this test, the results from the third stage of the DIC were primarily studied because they belonged to the longest monitoring period where the specimens did not have any restraint. To start, it is important to think about the characteristics and conditions of both concrete and steel bars. As per ACI 318-19, the concrete used in this research had a modulus of elasticity at 28 days of age, E_C, equal to 4,853 ksi (33,463 MPa), while that of steel, E_S, is normally considered as 29,000 ksi (200,000 MPa). This makes the reinforcing bars many times stiffer than the concrete. Furthermore, the steel rebars had a high degree of local restraint at the end angles of the setup. This avoided significant rigid body motions and let deformations throughout the concrete mass build up on them according to the mechanisms of force transferring described in Chapter 1. The concrete, in contrast, was strongly constrained at both shear-connector-stud regions. Also, it had a small amount of restraint coming from the chemical adhesion and friction with the steel at the girder and end angles interfaces.

For analyzing the results, the way the specimens shrink and the role of the steel bars in controlling it should be evaluated. As discussed earlier, it was expected that shrinkage created compression forces on the decks that would try to shorten them, especially in the longitudinal direction of their middle region. If bond did not exist, the concrete will be free to shrink. Conversely, if the rebars were

strongly engaged to the concrete, they should share a certain amount of strain coming from the shrinkage action. This rationale could not be verified with the measurements obtained from the concrete strain gauges, because no comprehensive depiction of the shrinkage effects could be interpreted from the values. This could have happened because, as seen in Appendix A, shrinkage is a tridimensional phenomenon that originates in the cement matrix of the concrete. However, the strain recorded on the middle region of the reinforcing bars strengthened this observation. Figure 28 presents the strain values from the rebars towards the end of the monitoring period. These results were illustrated in plots that identified the reinforcement layer on which the devices were installed. In addition, the left and right plots correspond to the strain gauges installed on those sides of the specimen reference diagram, respectively. Also, the ordinate of each displayed value in every plot matches with the installation position of the strain gauges. This can be conveniently verified by extending horizontal lines from each vertex of the plot and corroborate that they coincide with the points on the diagram. During the data acquisition, strain gauge EC-S-B3 (Figure 24) started to show erratic readings. Therefore, the information reported from it was not considered. The reference diagram is the result of superposing the strain gauges indicated in Figure 24 and Figure 25. It demonstrates that the devices were closely grouped in four major areas at each side of the steel girder: studs region, studs and no-studs interfaces, and the middle of the no-studs region.

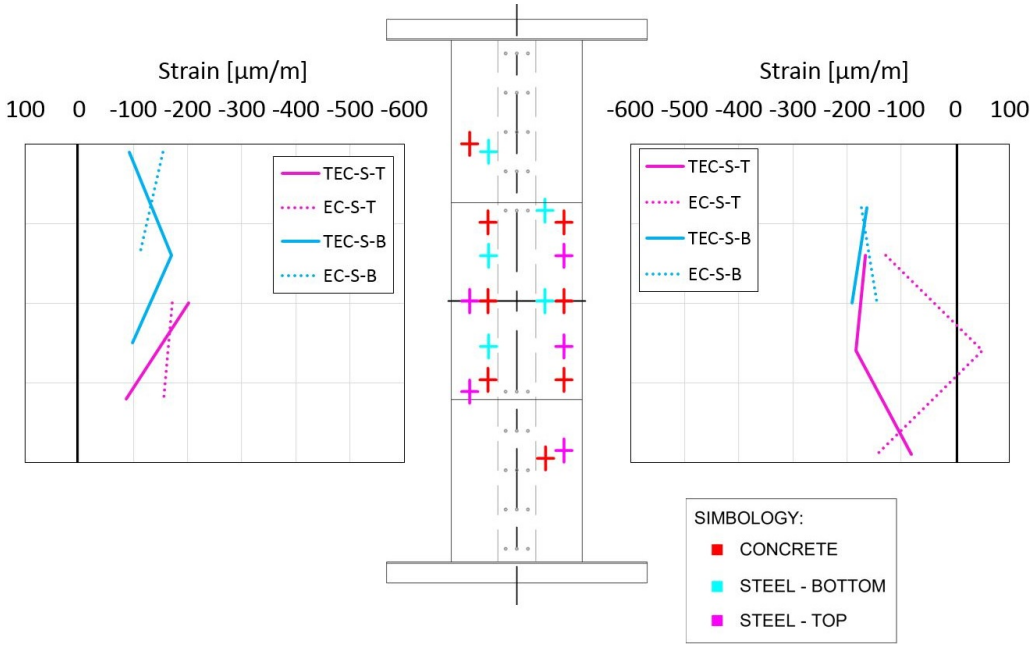

Figure 281. Graph. Strain gauges values from the reinforcing bars of EC and TEC specimens.

As seen in Figure 28, in the middle region of the specimens, where the coating principally influenced the behavior, the strain recorded on the TEC rebars was greater than that recorded on the EC rebars. This shows that more resistance was proportioned by this reinforcement against the shrinking action. Figure 27 supports this observation because it shows that the deformations on the middle region of the TEC specimen were, on average, 21% smaller than those displayed by the EC specimen.

CHAPTER 6: TEMPERATURE EFFECT SIMULATION TEST

According to the National Centers for Environmental Information (NCEI), in Illinois, 70°F (39.0°C) was the difference between the mean maximum and mean minimum temperatures achieved in 2020 (NCEI, 2020). This variation does not have the same effects on the concrete and steel elements of a bridge structure. Although it is well known that increasing the temperature usually causes an increase in the volume of solids and vice-versa, steel and concrete have a major difference in the way they transfer their associated heat. Thermal conductivity is defined as the rate at which heat is conducted through a body (Boyes, 2010). Concrete has a low thermal conductivity, which, in the studied scenario, produces a slow movement of energy from the surface to the interior of the deck. On the contrary, the thermal conductivity of steel is several times higher (Young & Freedman, 2016), giving the opposite result. Hence, in those cases where the ambient temperature increases, steel expands more rapidly than concrete, generating tensile thermal strains and stresses along the deck that represent the major cause of transverse cracks. Additionally, the response of bridge decks is not only affected by the nature of the materials, but also by the interaction of the different constraints these elements possess, such as the boundary conditions or the position of shear connectors, which influence the development of significant internal stresses.

TEST SETUP

This part of the experimental program studied the behavior and tendency of both specimens to crack under a similar variation in temperature. The test was conducted after the drying shrinkage monitoring period ended, once it had already been verified that the specimens had developed their design strength capacity. The boundary conditions were the same as the ones specified previously in Chapter 5.

The temperature difference was simulated by applying a thermal load on the half of the steel girder adjacent to the roller support. It was important to apply it in a way that prevented extreme upwards or downwards deflections of the specimens that could create additional forces acting on the concrete deck. For example, had the heat been concentrated only on the lower region of the steel girder cross-section, the element would have exhibited a concave-upward shape as the thermal expansion came into effect. Based on this premise, the test was accomplished using four 60 in. long (1.50 m) T-shaped stainless-steel burners placed on both sides of the girder web, supported on custom-made metal stands. They were grouped in two pairs. In every pair, each of these elements was connected to one propane tank through a 12 ft long (3.66 m) hose and split tee adaptor. This distribution was beneficial to convey the heat and produce mostly longitudinal strains, avoiding the undesired effects of significant deflected shapes explained above. A cross-section of the arrangement is shown in Figure 29-A, and a lateral elevation is shown in Figure 29-B. The burners were then kindled and heated the W-shape section until its upper part reached 150°F (65.6°C), which could represent the temperature of a member receiving intense sunlight in the summer season. During the heating process, which took approximately 6 hours, the amount of gas was regulated by the valves located at the tanks, so that small-sized flames emanated from the burners. Once the heating time was completed, the propane tank valve was closed, and the specimens were allowed to cool down.

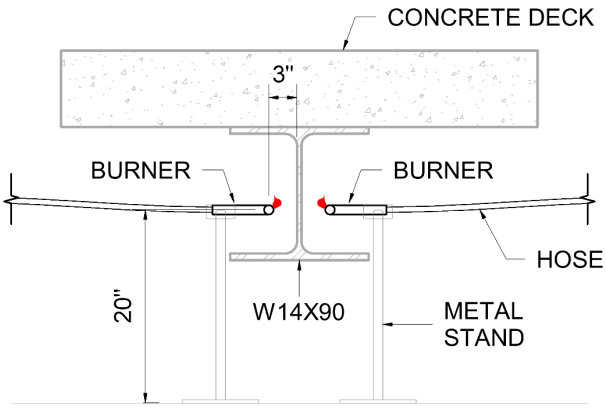

A. Cross-section detail of the middle portion of the specimen.

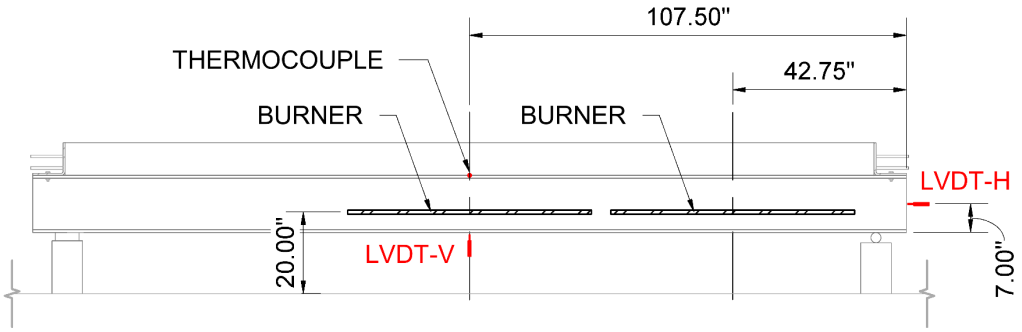

B. Lateral elevation detail of the specimen.

Figure 29. Illustrations. Temperature effect simulation test diagrams.

As also shown in Figure 29-B, besides the instrumentation described for the drying shrinkage test, a thermocouple and two LVDTs were included in this test. The thermocouple was installed at the middle span of each specimen, in contact with the upper region of the top flange of the W-shape sections. The data recorded by the thermocouple was complemented by the data provided using a handheld, noncontact, digital infrared thermometer pointed at different regions of the steel and concrete elements at different stages of the test. Immediately before turning the gas tanks off, readings were taken with the thermometer around the strain gauge areas in order to make the corresponding adjustments due to their temperature sensitivity. Regarding the LVDTs, LVDT-V was vertically centered under the steel girder to measure any deflection induced by the increment in temperature. On the roller-side end, LVDT-H was installed to measure the horizontal expansion of the steel girder's longitudinal axis. Additionally, the rate of capturing photographs for the DIC differed from the previous test. In this case, pictures were taken every increment of 10°F (5.55°C) or approximately every 3 minutes, whichever happened first. While the burners were on, an insulation foam sheet was used to protect the column of the instrumentation frame holding the cameras. Finally, Figure 30 representatively illustrates the heating process of the test.

Figure 30. Photo. On-site temperature effect simulation test.

TEST RESULTS

The strain distribution and the associated cracks that occurred in the speckle dot region once the heating time was completed are shown, for both specimens, in Figure 31. The residual strain distribution, recorded 24 hours after the test concluded, is presented for both specimens in Figure 32. Appendices B and C contain the detailed progression of the strain throughout the tests for the EC and TEC specimens, respectively. In all cases, the photographs of these figures were referenced as indicated previously in Figure 26.

Similar to the shrinkage test, some line references were positioned on the pictures to track the evolution of strain along them. In this particular test, they were vertically located over the cracks and were indicated on the outside of the images to avoid any visual interruption with the results. Specifically, the EC specimen had one line, while the TEC specimen had three lines, each made out of a thousand points. The strain values that coincided with them were illustrated, according to their color code, in the plot that accompanies every picture on its left side. The dimly colored curves of the plots corresponded to the magnitude of ε_{xx} obtained from the DIC analysis, while the dark, solid delineations represented the average of those positive and negative values independently.

Besides the reasons explained in Chapter 5 for the nonsymmetric results coming from the DIC analysis, in this test, variations in the position of the burners could have also influenced the values illustrated in the contour plots. However, a remarkable difference was noticeable between both specimens.

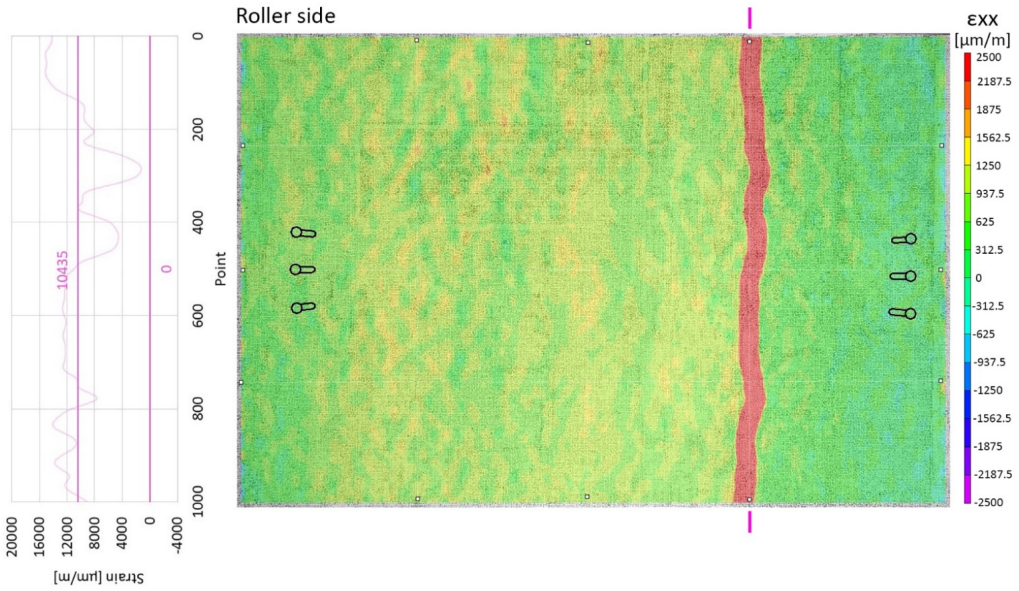

A. EC specimen.

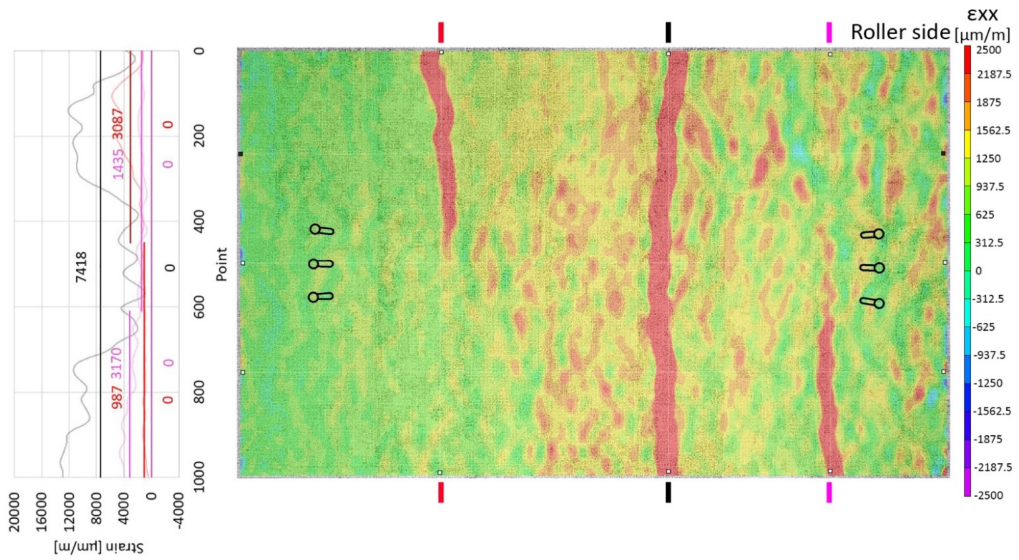

B. TEC specimen.

Figure 31. Illustration. Final strain distribution once the heating time was completed.

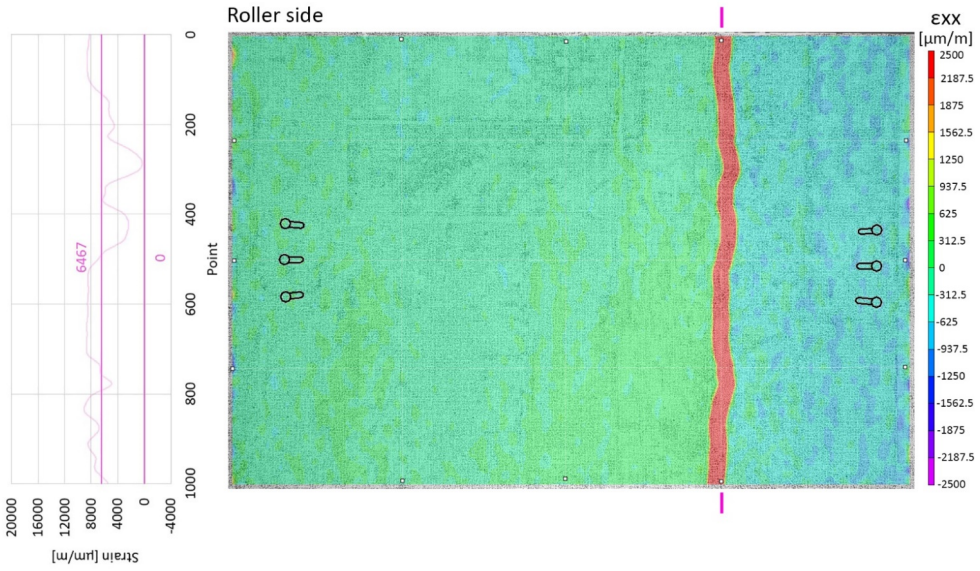

A. EC specimen.

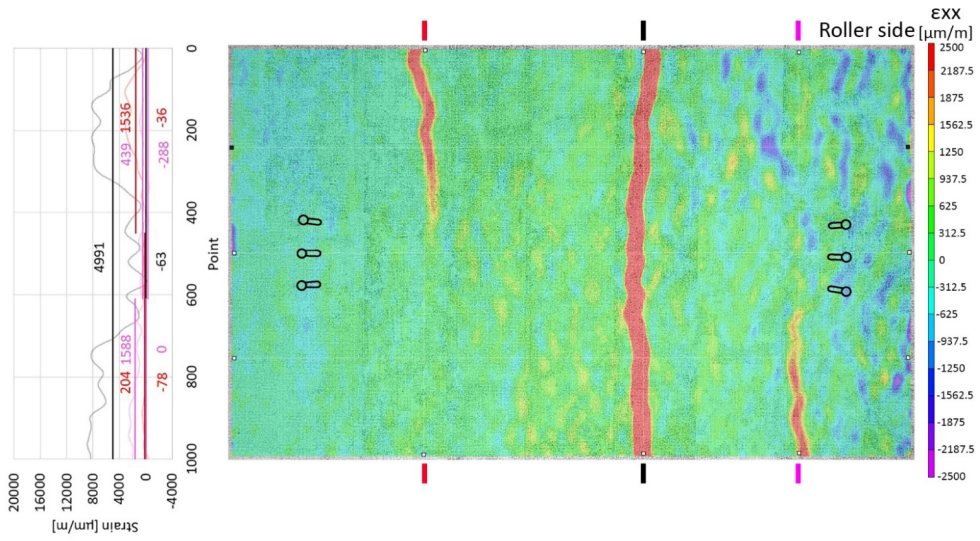

B. TEC specimen.

Figure 32. Illustration. Residual strain distribution 24 hours after the heating was terminated.

As the previous figures evidenced, cracks developed when the concrete stress caused by the induced heating reached its tensile strength at a particular cross-section. They were captured by the DIC as regions with excessive positive strains. This strategy proved to be a useful technique to identify cracks that were difficult to see by visual inspections.

Figure 33 illustrates the location and length of the cracks developed in both specimens. All cracks occurred perpendicularly to the main stress direction. The summary of their widths when the heat

was applied (open) and when room temperature was reached again after the test concluded (close) is presented in Table 5. Crack 2 developed in the TEC specimen was so small that it was not detected until the DIC analysis was run. Therefore, the value when it was open was not recorded (NR).

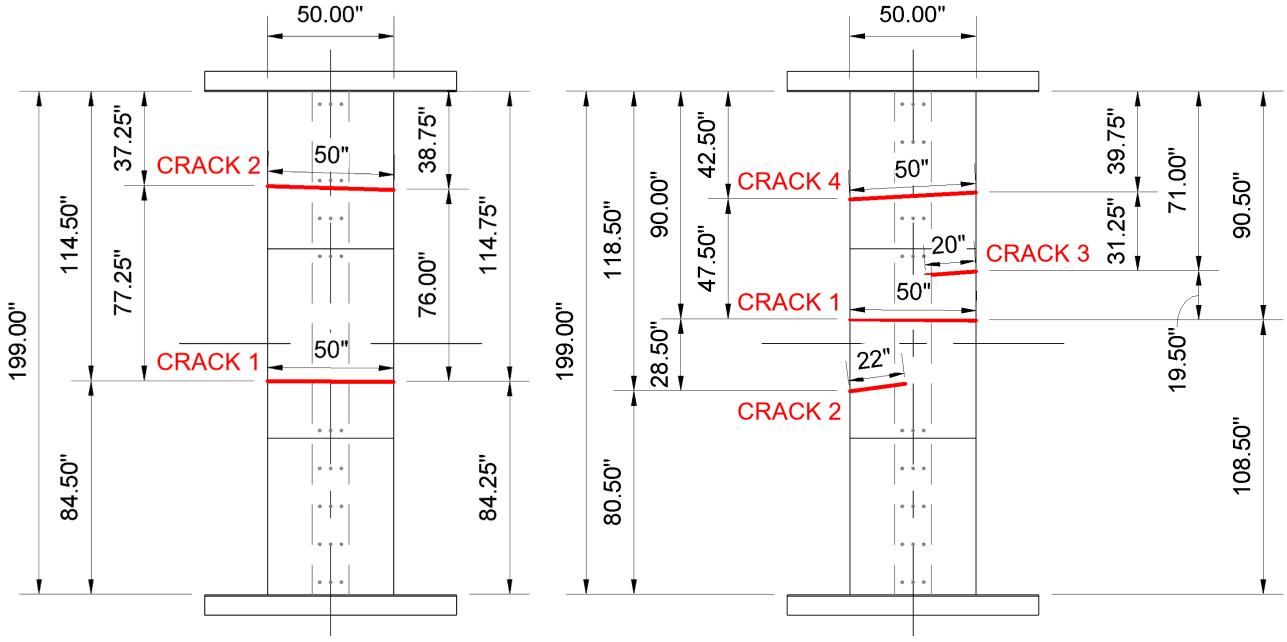

A. EC specimen. B. TEC7 specimen.

Figure 33. Illustrations. Cracks generated in the temperature effect simulation test.

Table 5. Crack Width Comparison between Specimens

	TEC		EC		TEC / EC ratio	
	Open	**Close**	**Open**	**Close**	**Open**	**Close**
First crack	0.012 in. (0.30 mm)	0.004 in. (0.10 mm)	0.015 in. (0.38 mm)	0.008 in. (0.20 mm)	0.80	0.50
Second crack	NR	0.002 in. (0.05 mm)	–	–	–	–
Third crack	0.003 in. (0.08 mm)	0.002 in. (0.05 mm)	–	–	–	–
Last crack	0.006 in. (0.15 mm)	0.003 in. (0.08 mm)	0.010 in. (0.25 mm)	0.005 in. (0.13 mm)	0.60	0.60

The information above shows the EC specimen contained fewer but wider cracks than the companion TEC specimen. As Gilbert (1992) explained, crack widths depend primarily on the amount of bonded reinforcement crossing the crack. Therefore, the greater slip accredited to the low bond that exists between the EC rebars and the concrete at the vicinity of the cracks could have been the reason for this observation. Figure 33 showed that the open area due to cracks of the EC specimen when it

recovered room temperature (close state) was 0.65 in.^{2}, while that of the TEC specimen was 0.43 in.^{2}. This represented a reduction of 33% in the cracked surface by using the new textured epoxy-coating, which also would imply less exposure to external agents that can compromise the integrity of the reinforcement.

Likewise, it is important to evaluate the spacing and number of cracks. In the EC specimen, cracks were widely spaced in comparison to those of the TEC specimen. This might be attributable to the loss of adhesion originated by the traditional epoxy-coating, which makes the rebars need more distance to effectively transmit the stresses to the concrete. Similarly, the greater number of cracks exhibited by the TEC specimen could have been originated from the significantly higher resistance to slip and crack widening provided by this type of coating. Specifically, the increased stiffness of the deck due to the bond may have caused the thermal load to impact the steel girder first. This, in turn, would have caused more restraint on the shear connector studs. The greater values of strain showed between the cracks in Figure 31-B evidenced that the concrete and steel bars sustained more demand on these regions.

CHAPTER 7: FLEXURAL TEST

In this study, the flexure test was intended to monitor and compare the development of strain on both specimens under flexural stresses caused by a tandem arrangement. Differences in the magnitude or patterns of the strain can indicate how good the bond between the reinforcement and concrete is and how the steel rebars, particularly the bottom layer, influence it.

TEST SETUP

The setup described in the previous chapters was modified for this test. The W-shape section was now supported on one end by a hinged block and on the opposite end by a steel rod, simulating a pinned-roller simply supported boundary condition, as shown in Figure 34.

A. Pinned support. B. Roller support.

Figure 34. Photo. Boundary conditions for the flexural test.

For instrumentation purposes, as will be explained later, these supports rested on 6 ft tall (1.83 m) reinforced concrete L-shaped elements, anchored to the testing floor using DYWIDAG threaded bars. Additionally, a reaction frame was assembled to hold the actuator in charge of applying the load. This frame consisted of two columns, made out of two MC10 × 28.5 sections each, and one top beam, made out of a double W18 × 119 section. Bolted connections were used at the joints to attach these members. Also, it was not necessary to alter the length that the top beam possessed because, to match the distribution of holes on the testing floor and be able to anchor the concrete blocks that were providing support, the longitudinal axis of the specimen was moved to one side of the frame, as illustrated in Figure 35-A. The force applied by the actuator was distributed through a pair of spreader W10 × 49 beams reinforced with stiffeners. To simulate the tandem vehicle spacing, two plates with a 4.50 × 2.75 in. (114.3 × 69.9 mm) cross-section and a length of 55.0 in. (1.40 m) were centered on the specimens, maintaining 4.0 ft. (1.22 m) between each other's centerline in the longitudinal direction, as illustrated in Figure 35-B.

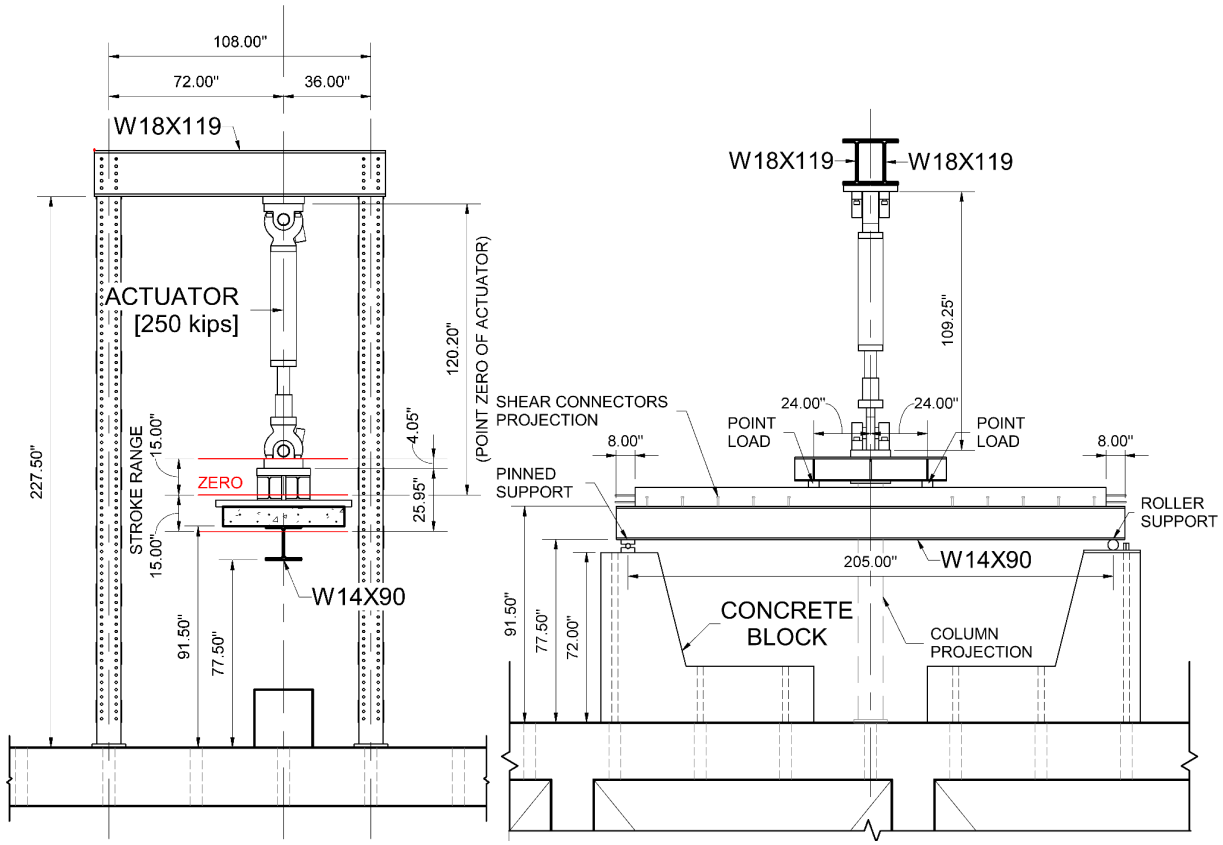

A. Front view. B. Lateral elevation view.

Figure 35. Illustration. Flexural setup diagrams.

An additional advantage of the simulated tandem vehicle was that it presupposed a four-point bending lineup. Therefore, in the region between the two loading plates, uniform bending moment occurred without the interaction of shear components. This helped provide insight into the bond behavior of both types of rebars under pure bending stresses.

Although the steel angles on both ends of the specimens were not removed, the restraint they provided was not expected to alter the bond behavior of the bars because the development length of the reinforcement, l_d, calculated as 35.6 in. (0.90 m) for the EC rebars, according to ACI Committee 318 (2019), was smaller than the distance between the point of load and the edge of the deck. Figure 36 summarizes the principal stages of building the setup described above.

For the loading procedure, a displacement-control protocol was adopted. Precisely, the servo-controlled hydraulic actuator employed for the test applied the load in a way that allowed the gradual development of strain and the appreciation of potential cracks. The selected rate was 0.10 in./min. (2.54 mm/min.). Because it was desired to compare the behavior between both specimens under conventional traffic loads, the maximum force that was evaluated was 64.0 kips (284.7 kN), which represents a tandem load of 32.0 kips (142.4 kN) per axle. This value resembled the design magnitude of tandem vehicles after the distribution and load combination factors are applied.

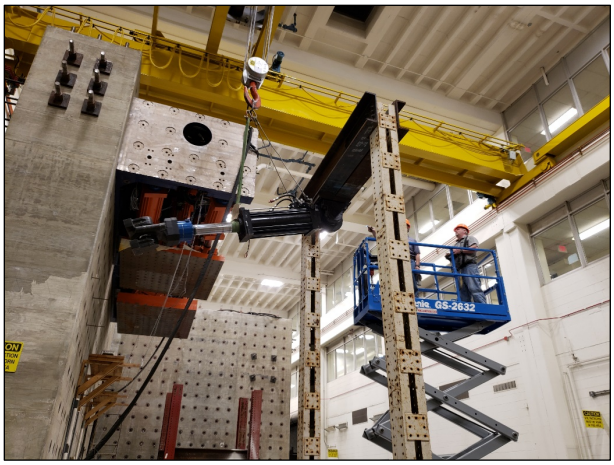

A. Installation of the actuator.

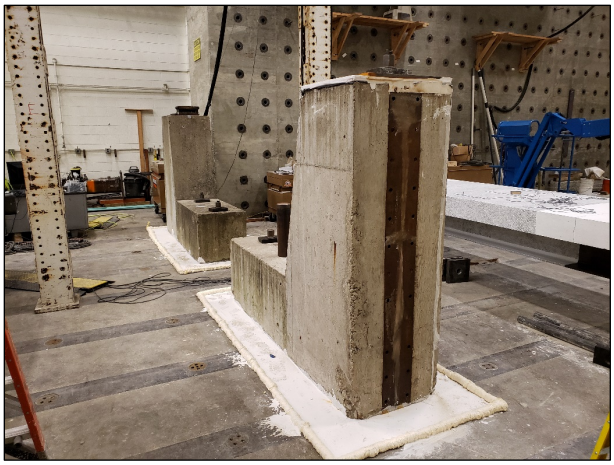

B. Placement of concrete blocks.

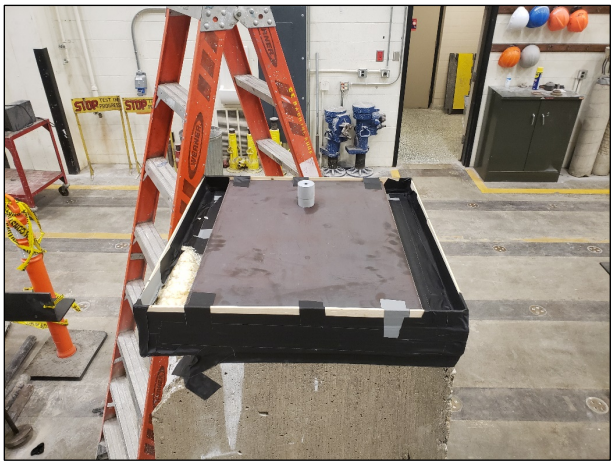

C. Preparation of support surfaces.

D. Movement of specimens.

Figure 36. Photo. Flexural setup construction.

Instrumentation

For the instrumentation, strain gauges, LVDTs, cable-extension position transducers (CEPT), and DIC were incorporated. The DIC was intended to measure the development of strain on the critical surfaces of the specimens, examine the behavior of the existing cracks, and track any generation of new cracks, even those that might not be appreciable to the bare eye. In this case, the regions of interest were the bottom of the deck and one side of the specimen. The former, shown in Figure 37-A, comprised the areas located at both sides of the steel girder, while the latter, shown in Figure 37-B, comprised the lateral face of the deck and the steel girder's web. After removing the strain gauges from the previous tests that coincided with the painted areas, the speckle dot pattern was applied as described in Chapter 5. For this test, three Nikon D90 cameras were used. The first camera was aimed at the bottom of the deck, the second one at the lateral surface of the deck, and the third one at the lateral surface of the steel girder. Because the same dot diameter was adopted, all cameras were separated approximately 68 in. (1.73 m) away from the target regions. This was the reason behind

using the concrete blocks to keep the specimens in an elevated position. Also, four light stands were used to keep the speckle dot pattern illuminated during the photograph acquisition period.

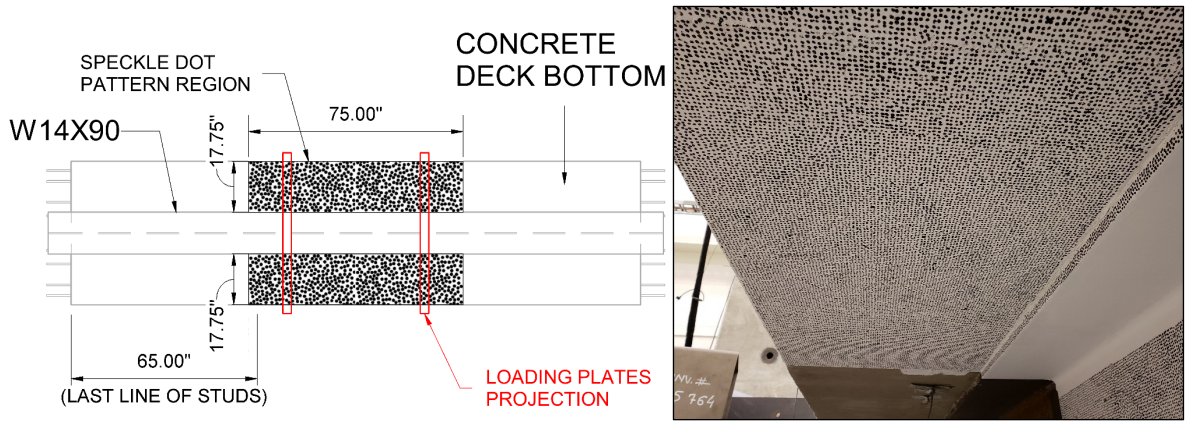

A. Typical diagram for the bottom DIC (left) and applied speckle dot pattern on the underside of the deck (right).

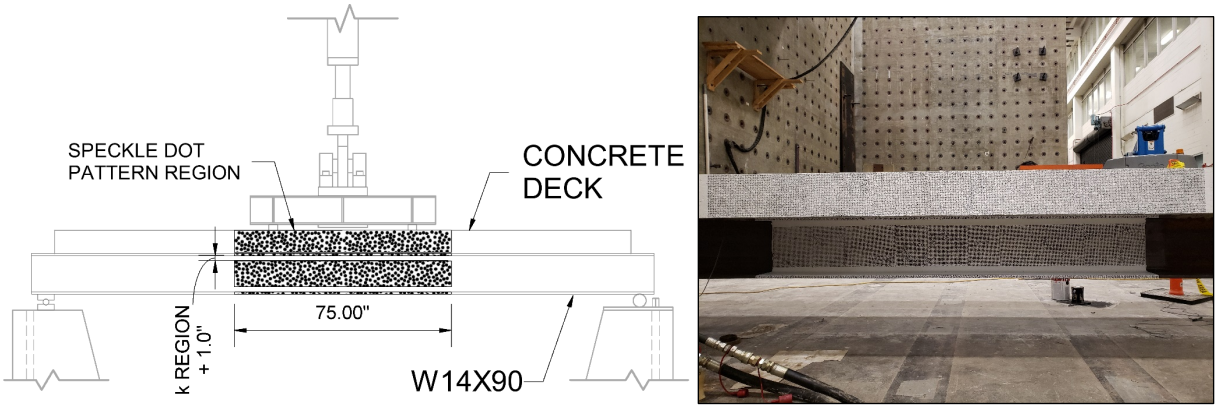

B. Typical diagram for the side DIC (left) and applied speckle dot pattern on the lateral faces of the specimen (right).

Figure 37. Illustration and photo. DIC regions for the flexural test.

Regarding the instruments used to measure displacement, Figure 38 shows the location of the CEPTs used in the test. CEPT-V1 and CEPT-V2 measured the midspan deflection of the specimen at the center and at one side of the W-shape section, respectively. CEPT-V1 was the direct reference to monitor and the level of deflection attained in each loading cycle. CEPT-V2 was incorporated so that, when compared with the readings of CEPT-V1, any twisting of the specimen could be identified. CEPT-H1 was intended to measure any out-of-plane movement of the reaction frame on the column that experienced the highest demands. In addition to CEPT-H1, two LVDTs were installed to verify the correct alignment of the setup during the test. The first one measured any vertical movement on the frame beam happening due to the readjustment of the bolts within the beam-column connection. This was useful to confirm that any sudden, temporary drop in the load was originated entirely by the behavior of the specimen or the development of cracks. The second one measured any horizontal

displacement of the roller support to ensure that any slip occurred between the rod and the bottom flange of the steel girder.

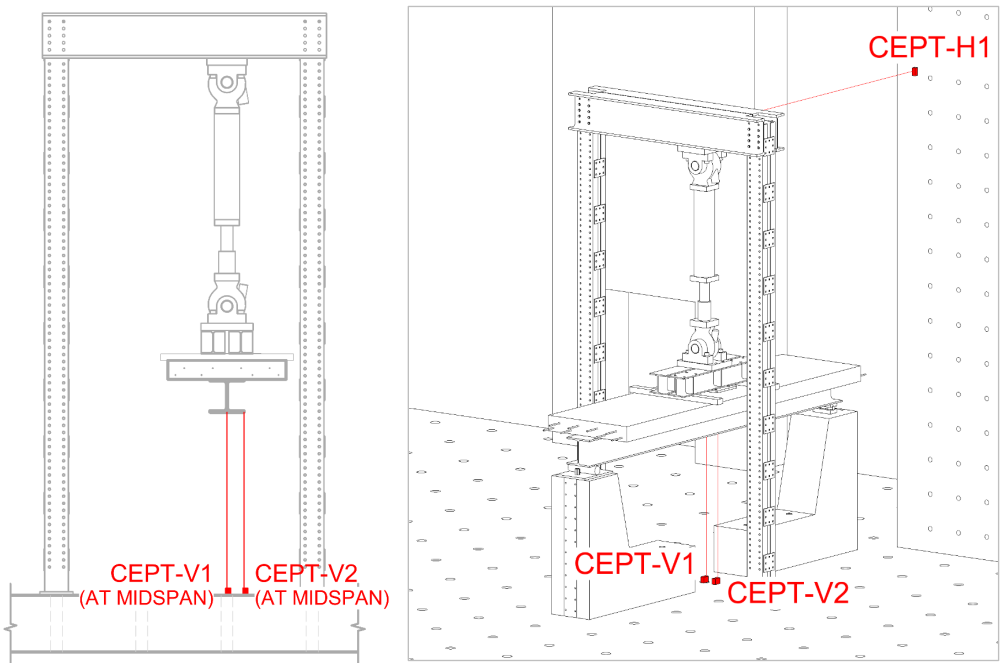

A. Front view. B. 3D view.

Figure 38. Illustration. Instrumentation to measure displacements.

Strain gauges, in turn, were installed on the top surfaces of the decks. As seen in Figure 39, they were distributed along the middle line of the specimens such that the strains generated by the shear lag were captured. The readings were recorded using the same data acquisition equipment as in the previous tests.

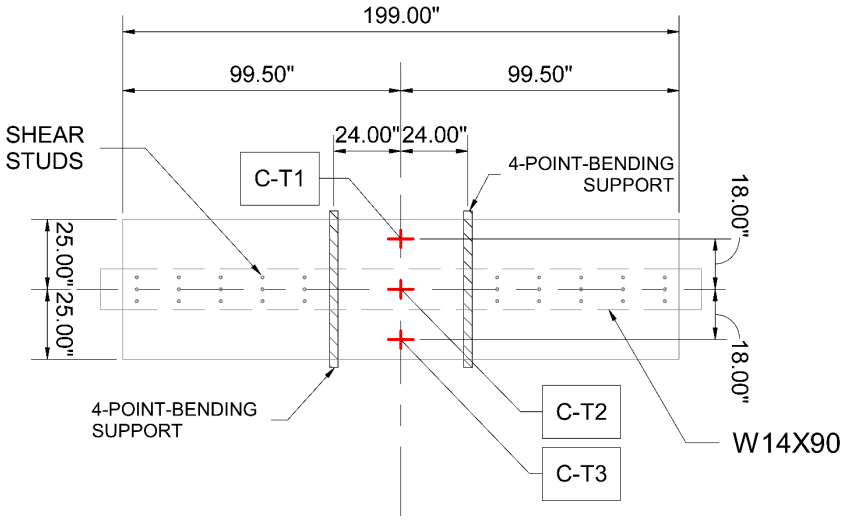

Figure 39. Illustration. Strain gauges ID on the top surfaces of concrete decks.

Finally, Figure 40 shows the complete setup assembled in the laboratory before starting the test.

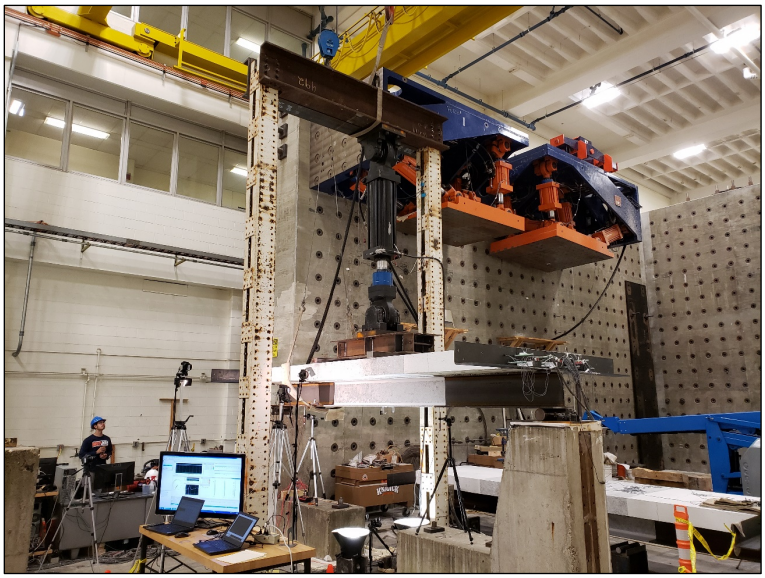

Figure 40. Photo. Flexural test setup.

TEST RESULTS

From the readings of the strain gauges installed on the transverse axis of the specimens, it was possible to obtain the strain distribution across the depth of the concrete deck of the composite sections. Pictorially, Figure 41 shows the strain distribution on both specimens for an applied load of 64.0 kips (284.7 kN), equivalent to a tandem axle load of 32.0 kips (142.4 kN).

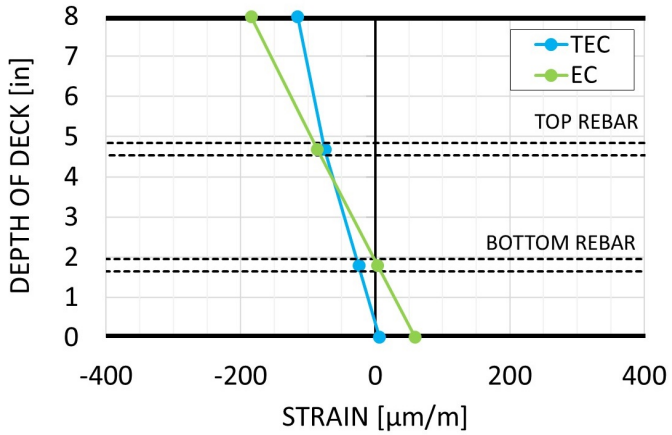

Figure 41. Graph. Strain distribution across the depth of the concrete deck.

From this result, both specimens showed a linear response, which meant that no plastic deformations were induced in the concrete deck. Between them, the EC specimen experienced more deformation than the TEC counterpart. In other words, the TEC specimen was stiffer. By using the results of Figure 41, it is possible to calculate the curvature of the composite sections to corroborate numerically the

previous observation. Thus, at this level of load, the curvature of the EC specimen, ϕ_{EC}, was 3.0×10^{-5} in.$^{-1}$ (1.20×10^{-6} mm^{-1}), while that of the TEC specimen, ϕ_{TEC}, was 1.5×10^{-5} in^{-1} (6.0×10^{-7} mm^{-1}).

The comparison of the load-deformation behavior of the specimens could also be verified by constructing a moment-curvature plot from the different points of the loading protocol. In this case, Figure 42 shows the curves for both the EC and TEC specimens. From the results, it is possible to corroborate the fairly linear response exhibited by both composite sections at this level of load. Also, by evaluating their slope, the one corresponding to the EC specimen is less steep than that of the TEC specimen. This difference reaffirms the observation stated above about the greater flexibility revealed by the EC specimen.

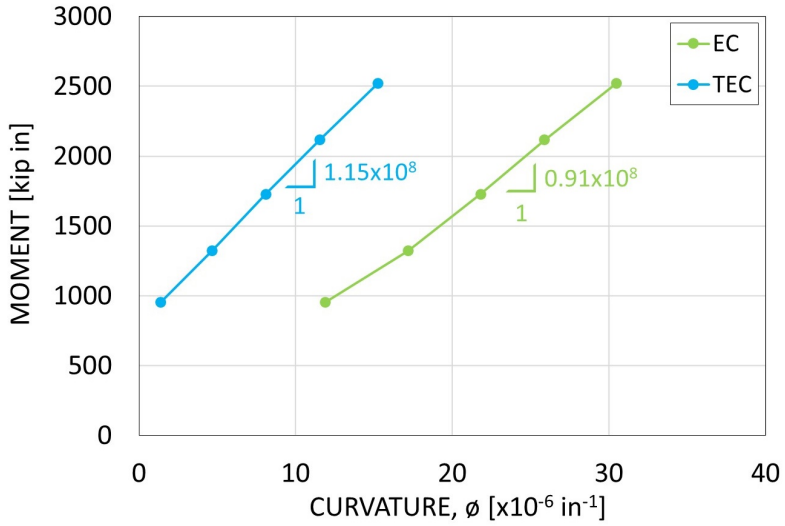

Figure 42. Graph. Moment-curvature plot from EC and TEC specimens.

For the DIC, pictures were captured at turning points, when each target displacement was attained. However, it was not possible to take the reference photographs at the same level of load used for the previous plots. Thus, the contour plots shown next in Figure 43 and Figure 44 were generated from the pictures taken at the nearest possible force level, which, in this case, occurred at 40.0 kips (177.9 kN). Specifically, Figure 43 shows the results for the bottom face of the deck, while Figure 44 shows the results for the side face of the deck. The DIC analysis was considered acceptable because the purpose of the test was to study the differences in the distribution of strain between both specimens in the elastic range, at load levels similar to those conferred by conventional traffic.

In Figure 43, some dashed reference lines were marked on the central transverse axis of both specimens. Along these lines, the average value of strain of the TEC specimen was 25% lower than that of the EC specimen. It is believed that this is the result of the lower bond capacity of the EC reinforcement; hence, a certain degree of longitudinal slippage occurred between the rebars and the adjacent concrete. Consequently, EC bars do not absorb the stress that TEC bars do and, instead, require the concrete to be more engaged in actively resisting the tension caused by the flexural demand.

Figure 44, in turn, revealed that the vicinity of Crack 1 of the EC specimen was surrounded by a greater region of compressive strains than the vicinities of Crack 1 and Crack 3 of the TEC specimen. This meant that, as expected, the cracks were being closed as the flexural action was developed at the upper elements of the composite section. Overall, Crack 1 and Crack 3 from the TEC specimen reported 60% and 74% less strain in comparison to Crack 1 of the EC specimen, respectively. The higher strain from the EC specimen might be attributable to a greater partial bond breakdown region around the crack resulting from the deficient interaction of the rebar surface and concrete. In this case, the lack of engagement of the concrete in these regions may have also subjected the steel bars to higher levels of stress that may have been translated into greater deformations. These observations showed agreement with the flexibility exhibited by this specimen in Figure 41.

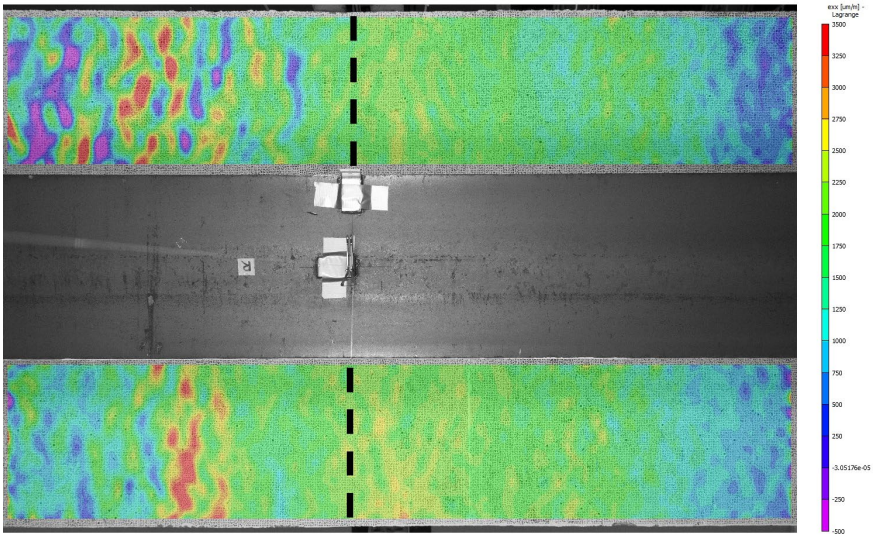

A. EC specimen.

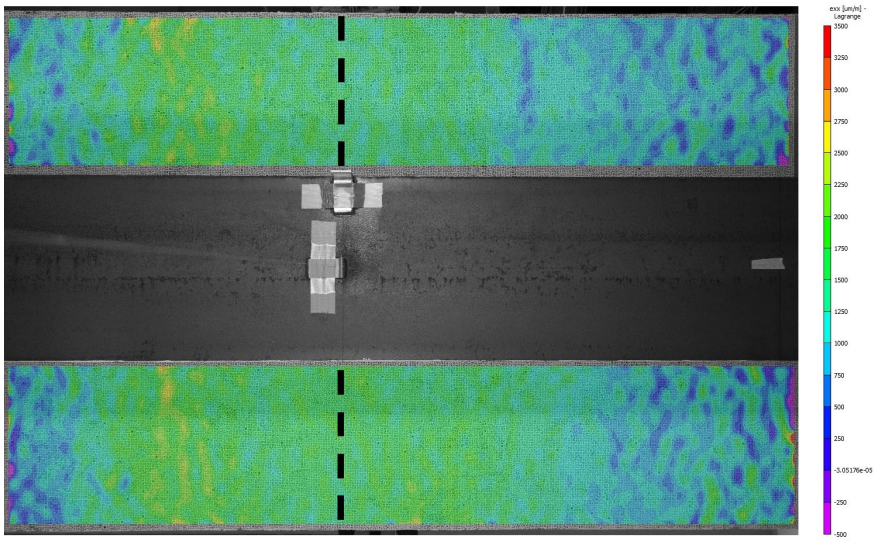

B. TEC7 specimen.

Figure 43. Illustration. DIC analysis on the bottom side of the concrete deck of the specimens.

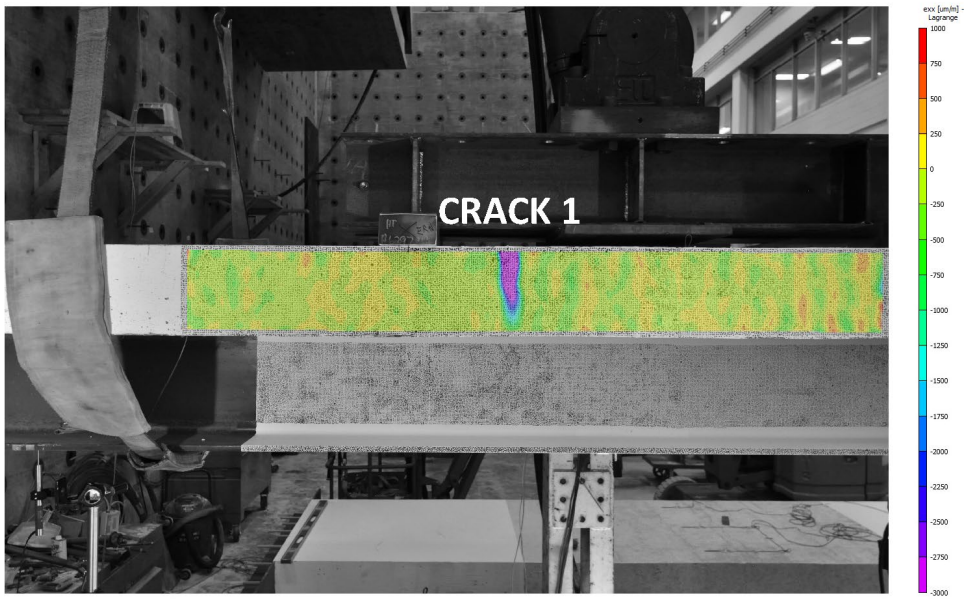

A. EC specimen.

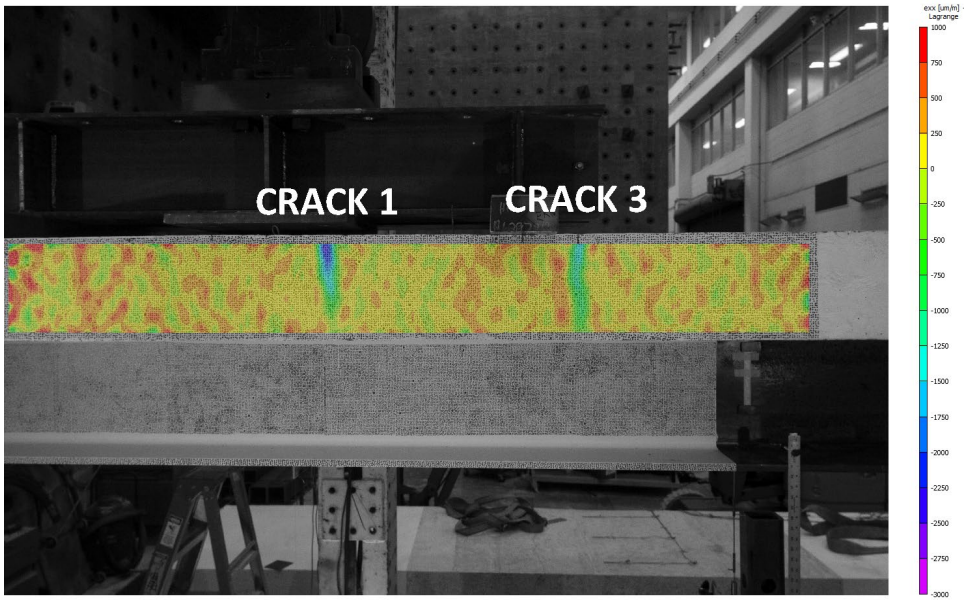

B. TEC7 specimen.

Figure 44. Illustration. DIC analysis on the lateral side of the concrete deck of the specimens.

CHAPTER 8: EMPIRICAL ROUGHNESS METHOD

As explained in the previous chapters, different types of TEC rebars, classified according to their surface characteristics, have been studied in this project. The structural performance of these bars is impacted by their roughness properties, which are determined from 2D or 3D profile analysis. However, conducting these analyses is expensive, time-consuming, and requires specialized equipment that may not be readily available at the job site.

This part of the experimental program represented the first approach to establish an empirical method for determining the suitability of the roughness of TEC bars in practical cases. Although it will likely always be required to document some roughness parameters to meet the quality control plan, this assessment could be useful as a preliminary criterion to determine, for instance, the acceptance of a batch of rebars delivered in the field.

TEST METHODOLOGY

The procedure that was conceived started by weighing the amount of solution residue that remained adhered to the surface of a piece of rebar after both being put into contact. At first, two types of solutions were studied: potable water and a mixture of potable water with different volume concentrations of ASTM C150/C150M-20 (ASTM, 2020a) Portland cement type I/II. Nonetheless, the latter option was discarded because the cement particles settled easily, creating a nonhomogenous balance.

All specimens that were evaluated belonged to a special batch of TEC rebars produced for this test and were classified into three main levels of roughness: fine, medium, and coarse. The batch consisted of 36 30 in. long (0.76 m) bars, distributed in 3 groups of 12 according to the roughness classification stated above. For every roughness level, the reinforcement sizes ranged from No. 5 to No. 8. so that three rebars corresponded to each diameter, as presented representatively in Figure 45. From each bar, two 12 in. long (0.30 m) pieces were cut in the “as-delivered” condition, making a total of six samples per case of study. The cut was done using a chop saw, trying to complete it as fast, clear, and precise as possible to avoid burning the coating. Additionally, for identification purposes, a descriptive nomenclature was adopted for the samples. First, it included the size of the rebar, second the type of the coating, third the level of roughness it belonged to, and lastly a correlative number. From the correlative number, it was also possible to recognize the bar where each sample was cut from because they were organized in pairs, such that samples 1 and 2 came from the first bar, 3 and 4, from the second one, and 5 and 6 from the third one.

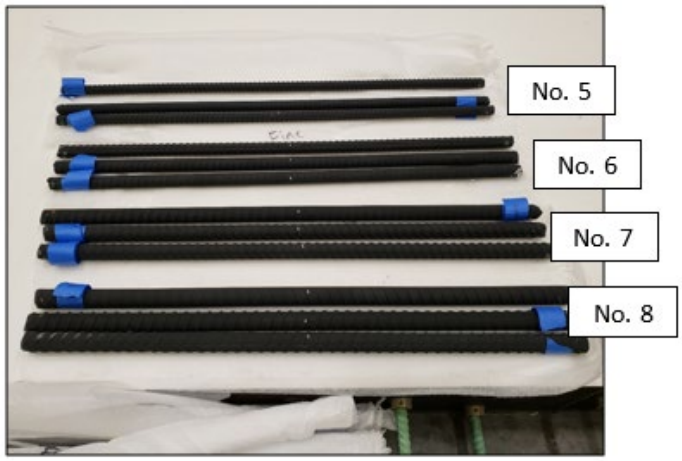

Figure 45. Photo. "As-delivered" reinforcement for the empirical roughness test.

Before starting the test, potable water was poured into a plastic container and was stored for 8 hours until it reached a room temperature of approximately 73.0°F (22.8°C). To register the temperature, a thermometer was dipped in the water for 2 minutes until the reading stabilized. Once the solution was ready, the test began by recording the dry weight of each sample. Soon after, the steel bars, individually, were completely immersed for 120 seconds in the container. After the immersed time elapsed and handling the sample with only a metallic pinch-off tool, the sample was removed from the container and allowed to drain the excess of water for 60 additional seconds, keeping it motionless in a vertical position. The metallic tool was useful because it did not absorb water, and most of these tools are wide enough so that the rebar is held by touching only some of the outer faces of the ribs. However, care must be taken not to subject the sample to excessive accelerations that may cause the loss of adhered water or to apply too much pressure that could damage the coating and alter the weight. The combination of immersion / drain times previously mentioned proved the clearest tendency, although other options, such as 60 seconds immersed / 60 seconds drained and 60 seconds immersed / 30 seconds drained, were studied. Last, the wet sample was weighed over a plastic sheet to avoid any loss of solution, and the difference between the wet and dry results, ΔW, was compared to the initially reported weight to obtain the corresponding ratio of increment. Some of the previously described steps are illustrated in Figure 46.

After the weighing procedure was concluded, the next step was to determine the roughness parameters of the samples. The procedure described in Chapter 2 was adopted using the same equipment. For the samples, one 3 in. long (76.2 mm) piece was cut from specimens 1, 3, and 5 belonging to each size and roughness level. Finally, when both the roughness parameters and ΔW values were obtained, any existing correlation between them could be evaluated.

A. Water temperature.

B. Sample immersed into the solution.

C. Draining process of the sample.

D. Wet weight of the sample.

Figure 46. Photos. Representative steps of the empirical roughness test.

TEST RESULTS

As explained before, the ΔW ratio was calculated for each of the six rebars samples based on the difference between their dry and wet weights. The average of these values, in percentage, for each type of bar is presented in Figure 47. In addition, the maximum and minimum results are incorporated in the plot as well as the 68% middle interval of the normal distribution of values corresponding to the mean, μ, and one standard deviation, σ.

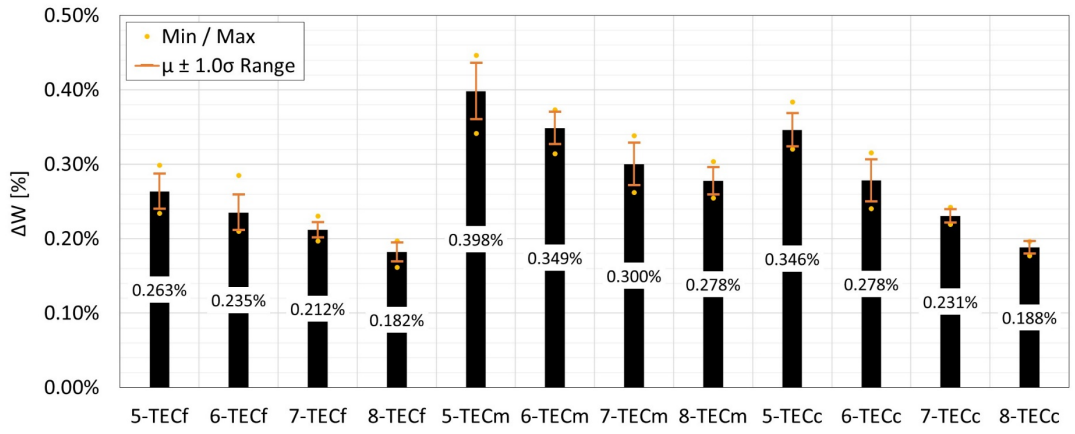

Figure 47. Graph. ΔW ratio of the rebars.

As seen in Figure 47, each level of roughness appeared to have a similar trend: as the bar size decreased, the water adhering to the surface was more significant with respect to its weight. For example, No. 5 rebars had the highest values in every case and by comparing them with No. 8 rebars, they had ratios 45%, 43%, and 84% greater than the latter for the fine, medium, and coarse roughness, respectively.

The evaluation of the roughness parameters was centered on R_a and S_a because they are more representative of the surface characteristics than R_{max} and S_{max}, which are easily skewed by outliers. Therefore, the average results obtained on each type of rebar for R_a and S_a are shown in Figure 48 and Figure 49, respectively. Again, these plots incorporate the maximum, minimum, and the 68% middle interval of the normal distribution of values.

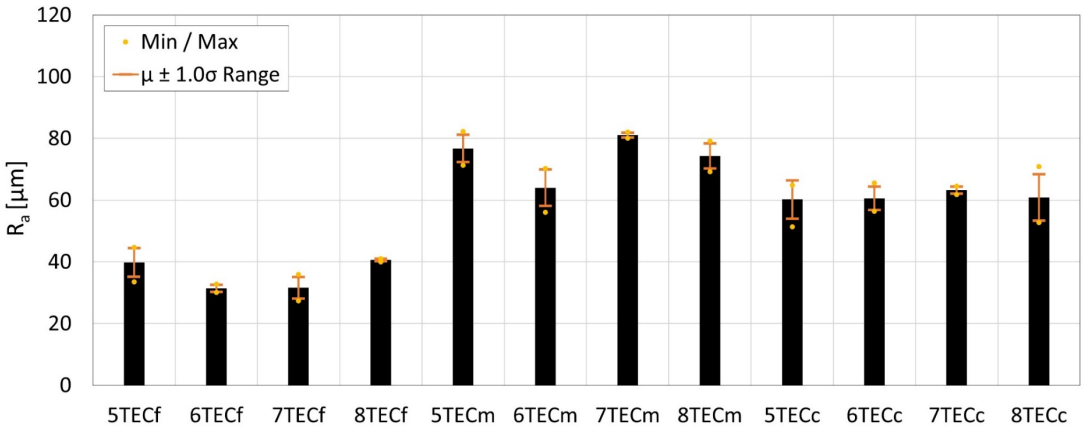

Figure 48. Graph. Roughness parameter R_a of the studied rebars.

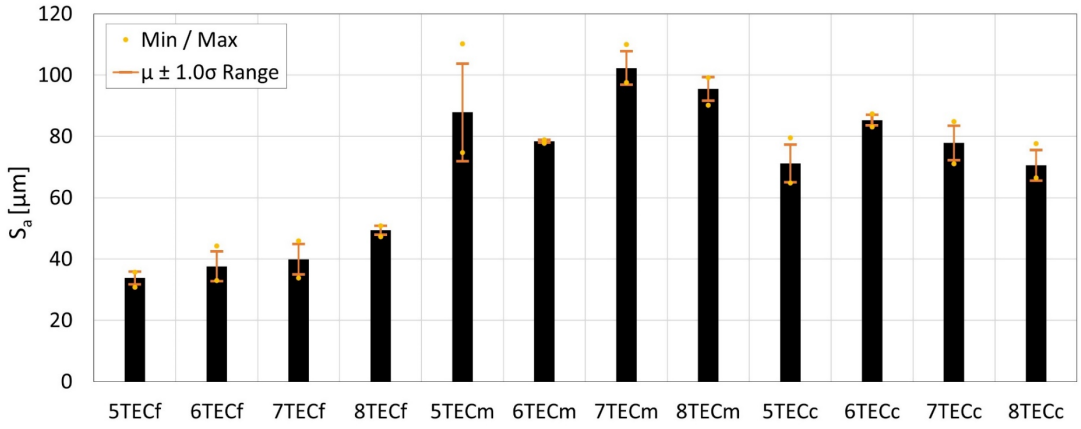

Figure 49. Graph. Roughness parameter S_a of the studied rebars.

From both figures, it is possible to see that, counterintuitively, the medium level of roughness possessed higher R_a and S_a values than the coarse level. This can be originated by factors associated with the size of the grain that provides the texture, its dispersion during the manufacturing process, or a combination of both. Next, the average values of R_a and S_a per level of roughness are presented in Figure 50 and Figure 51, respectively.

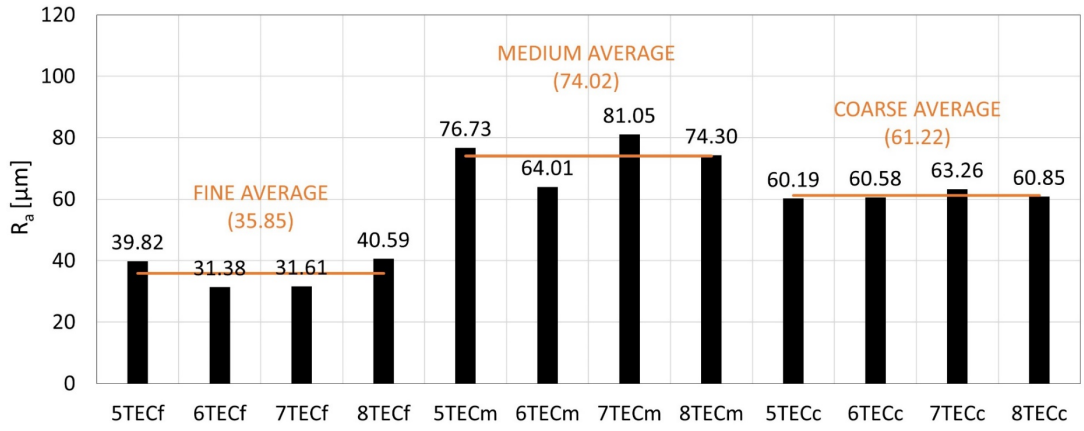

Figure 50. Graph. Roughness parameter R_a including the average value per level of roughness.

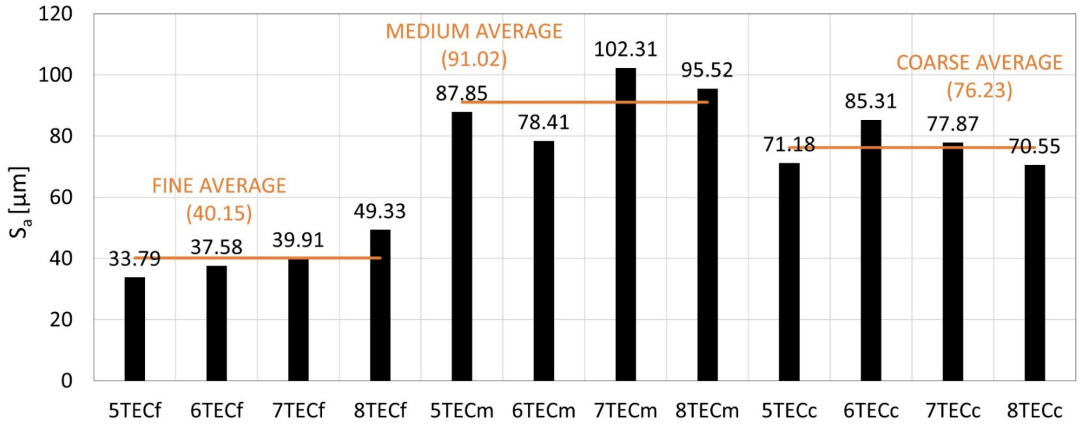

Figure 51. Graph. Roughness parameter S_a including the average value per level of roughness.

According to these results, the standard deviation of R_a for the fine, medium, and coarse levels of roughness was 4.36 μm, 6.27 μm, and 1.20 μm, respectively, and for S_a, 5.73 μm, 8.90 μm, and 5.98 μm, respectively. In both parameters, the medium level of roughness had the most scattered values, which can indicate less uniformity in the coating manufacturing conditions. In addition, R_a had less disseminated values overall, which are associated with a highly condensed coarse level of roughness. The previous plots were superimposed in Figure 52 to demonstrate the contrast they keep with each other.

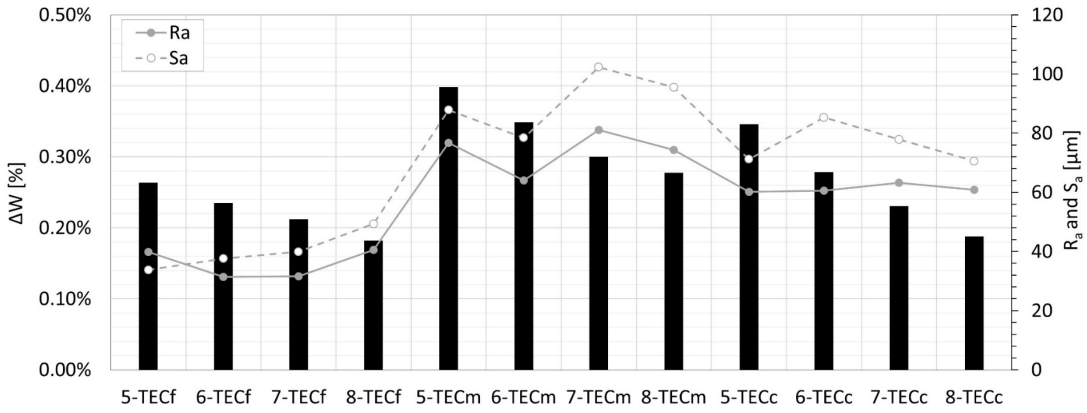

Figure 52. Graph. R_a and S_a parameters for each ΔW ratio corresponding to the studied rebars.

One of the main purposes of this test was to determine a range of ΔW that corresponded to an acceptable level of roughness. Between the analyzed roughness parameters, it was more convenient to work with R_a because, as stated above, less dispersion surrounded the results. Moreover, this test has the advantage of being straightforward and fast. S_a tests, in contrast, are more time-consuming, and the complexity to satisfactorily conduct them is higher. From the previous figure, no clear pattern of R_a can be identified per level of roughness. Therefore, rebars should be approached differently to evaluate any existing correlation.

The results presented in Figure 52 are isolated in Figure 53 for the No. 5 bars. In this case, the pattern followed by ΔW and R_a is promising because they show agreement. Regarding the acceptance threshold of the values, because TEC7 reinforcement was developed based on the characteristics of TEC2, TEC3, and TEC6 rebars, their corresponding R_a values should represent a compelling range for a satisfactory bond behavior. From Figure 4, the R_a values for TEC2, TEC3, and TEC6 bars were 44.69 µm, 42.82 µm, and 46.38 µm, respectively. Also from the same figure, TEC7 rebars had an average R_a of 67.26 µm, including the results of the reinforcement used in the pull-out tests of the present report. Based on this, it is reasonable to set 40 µm and 70 µm as the acceptable lower and upper limits, respectively, for R_a. However, these limits are established exclusively from research performed on No. 5 bars. Because of the differences in the nominal geometry, weight, and deformation dimensions of the different rebar sizes included in the current test, it is deemed inappropriate to draw solid conclusions by extrapolating the behavior of these samples to other reinforcement diameters. Therefore, further research is necessary to complement the study for rebar sizes other than No. 5.

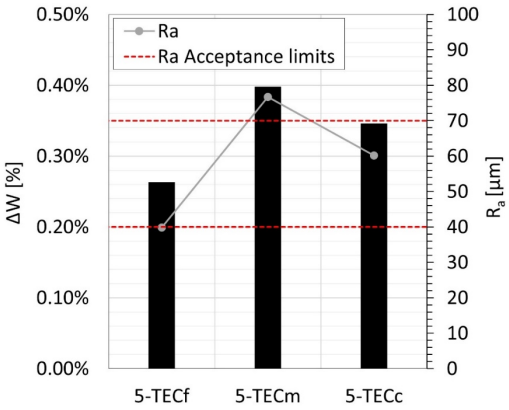

Figure 53. Graph. R_a parameter for each ΔW ratio corresponding to the studied No. 5 rebars.

As seen in Figure 53, the previously established lower R_a acceptance limit corresponds to a ΔW ratio of 0.20%. Similarly, the upper R_a acceptance limit corresponds to a ΔW ratio of 0.35%. Although the ΔW limits assessed look congruent, more experimental data needs to be included to grant more precision to the test method described herein.

CHAPTER 9: SUMMARY AND CONCLUSIONS

The experimental program of this research was designed to point out the major differences between using EC rebars against TEC rebars in laboratory bridge deck specimens subjected to different demands. These demands were defined based on representative conditions that bridge superstructures typically encounter during their service life. In particular, it was desired to examine the role of the coating in the development of strain and how it affected the bond behavior, especially at low levels of slip (initial slip resistance). For that purpose, after conducting a qualitative, quantitative, and bond-slip characterization of the textured reinforcement, two large-scale bridge deck specimens were tested under shrinkage, thermal gradient, and flexural loads. Finally, an empirical roughness measurement methodology was driven as a means of having a practical way to classify TEC bars on the job site, without incurring the need for costly and time-consuming tests. The following main conclusions can be made from the study:

CONCLUSIONS

1. The TEC bars evaluated in this study had R_a and R_{max} values three to eight times greater than those of UC bars. This exemplifies the difference in the magnitude of the surface roughness conferred by the textured epoxy-coating. Among all the coating types, TEC7 rebars exhibited the greatest surface roughness.

2. Based on the results of the current investigation, the use of polymeric powder to add roughness to the surface of epoxy-coated bars did not necessarily have a major impact on increasing their bond strength. On the contrary, the pull-out tests showed that most of the TEC specimens exhibited lower bond strengths than the UC and EC counterparts. However, more in-depth research is needed to validate this observation because the stress state induced in a pull-out test differs from that experienced by actual reinforced concrete members.

3. The TEC bars used in this study generally manifested higher initial slip resistance than UC and EC bars. TEC2, TEC6, and TEC7 pull-out specimens showed promise in improving the initial slip resistance when compared to the specimens reinforced with traditional UC rebars.

4. In this research, strong variation was observed in the pull-out tests that incorporated TEC7 reinforcement. This observation suggests the manufacturing process still needs to be optimized to provide reliable uniformity in the textured coating.

5. The microscopic examination performed on the TEC1–TEC6 rebars used in this study revealed that, with the exception of TEC1, all the surfaces possessed voids of various sizes and densities. These voids were likely to help in improving the initial slip resistance of the TEC bars because, at low levels of slip, only TEC1 exhibited an unsatisfactory performance. However, it was not evident if the presence of voids had any impact on the roughness parameters or the bond strength of the rebars.

6. The FE model of the pull-out specimen that was developed in this investigation could simulate the experimental force-slip results. Also, it was able to adequately capture the stress distribution at

the interfaces of interest (coating-steel and coating-concrete) and the damage progression of the coating layer with the surrounding concrete.

7. The results of the drying shrinkage test showed that TEC7 rebars had a more appropriate interaction with concrete under this type of demand. In particular, the TEC7 bars displayed greater values of compressive strain in the middle region of the specimen in comparison to the EC bars. This behavior suggests that the reinforcement from the TEC7 specimen was more actively resisting the shrinkage stresses induced by the concrete. The DIC results supported this observation as the concrete on the middle region of the TEC7 specimen seemed more relieved of stress than in the companion EC specimen.

8. Based on the results of the temperature effect simulation test, it is believed that bridge decks reinforced with TEC bars may sustain finer cracks than those reinforced with EC bars. Although slightly more cracks were observed in the specimen reinforced with TEC bars, the width of the cracks was as low as 50% of that of the specimen reinforced with EC bars. Furthermore, TEC bars reduced the area of the cracked surface (crack's width × length) by 33% compared to EC bars, which would imply less exposure to external agents that can compromise the integrity of the reinforcement.

9. The results of the flexural tests demonstrated that TEC bars possessed significantly higher resistance to slip and crack widening. The percentage of reduction in the strain at the vicinity of the cracks was significantly higher (as high as 74%) in the TEC specimen with respect to the EC specimen. In addition, similarly to the case of the shrinkage test, concrete had lower levels of stress because the reinforcement was more engaged to it. This observation was supported by the DIC contour plots, where a reduction of 25% in the strain was visible on the central transverse axis of the bottom layer of the deck of the TEC specimen compared to that of the EC specimen.

10. This investigation represents the first step in studying the influence of the textured epoxy coating protection system on large-scale models. To further this novel technology, more research is needed to evaluate the performance of TEC bars subjected to, for example, fatigue demands, repetitive cycles of thermal loading, flexural capacity at the ultimate state, aging, etc.

11. According to the empirical roughness methodology developed in this study, No. 5 rebars that were capable of retaining between 0.20% and 0.35% of water compared to their dry weight are likely to present an adequate roughness for structural purposes. However, the number of samples in each of the studied subsets was not statistically significant to provide a solid confidence level. Therefore, more tests are needed to complement these results and evaluate reinforcement with greater diameters.

REFERENCES

ACI Committee 209. (2005). *ACI 209.1R-05: Report on factors affecting shrinkage and creep of hardened concrete*. American Concrete Institute.

ACI Committee 209. (2008). *ACI 209.2R-08: Guide for modeling and calculating shrinkage and creep in hardened concrete*. American Concrete Institute.

ACI Committee 318. (2019). *ACI 318-19: Building code requirements for structural concrete*. American Concrete Institute.

ACI Committee 408. (2003). *ACI 408R-03: Bond and development of straight reinforcing bars in tension*. American Concrete Institute.

ACI-CT. (2020). *ACI concrete terminology*. American Concrete Institute.

American Association of State Highway and Transportation Officials. (2017). *AASHTO LRFD bridge design specifications*, 8th ed. AASHTO.

American Society of Civil Engineers. (2021). *2021 infrastructure report card*. Retrieved March 2021, from https://infrastructurereportcard.org/wp-content/uploads/2020/12/National_IRC_2021-report.pdf

Association for Materials Protection and Performance. (2021). *Highways and bridges*. Retrieved April 2021, from https://www.nace.org/resources/industries-nace-serves/highways-bridges

ASTM International. (2016). *A706/A706M-16: Standard specification for deformed and plain low-alloy steel bars for concrete reinforcement*. ASTM International. https://doi.org/10.1520/A0706_A0706M-16

ASTM International. (2017a). *C172/C172M-17: Standard practice for sampling freshly mixed concrete*. ASTM International. https://doi.org/10.1520/C0172_C0172M-17

ASTM International. (2017b). *C231/C231M-17a: Standard test method for air content of freshly mixed concrete by the pressure method*. ASTM International. https://doi.org/10.1520/C0231_C0231M-17A

ASTM International. (2017c). *C1064/C1064M-17: Standard test method for temperature of freshly mixed hydraulic-cement concrete*. ASTM International. https://doi.org/10.1520/C1064_C1064M-17

ASTM International. (2019a). *C31/C31M-19a: Standard practice for making and curing concrete test specimens in the field*. ASTM International. https://doi.org/10.1520/C0031_C0031M-19A

ASTM International. (2019b). *C511-19: Standard specification for mixing rooms, moist cabinets, moist rooms, and water storage tanks used in the testing of hydraulic cements and concretes*. ASTM International. https://doi.org/10.1520/C0511-19

ASTM International. (2020a). *C150/C150M-20: Standard specification for portland cement*. ASTM International.

ASTM International. (2020b). *A992/A992M-20: Standard specification for structural steel shapes*.

ASTM International. https://doi.org/10.1520/A0992_A0992M-20

ASTM International. (2020c). *C143/C143M-20: Standard test method for slump of hydraulic-cement concrete*. ASTM International. https://doi.org/10.1520/C0143_C0143M-20

ASTM International. (2020d). *C39/C39M-20: Standard test method for compressive strength of cylindrical concrete specimens*. ASTM International. https://doi.org/10.1520/C0039_C0039M-20

Babaei, K., & Fouladgar, A. (1997). Solutions to concrete bridge deck cracking. *Concrete International*, *19*(7), 34–37.

Boyes, W. (2010). *Instrumentation reference book*. Butterworth-Heinemann.

Cairns, J., & Abdullah, R. (1994). Fundamental tests on the effect of an epoxy coating on bond strength. *ACI Materials Journal*, *91*(4), 331–338. https://doi.org/10.14359/4040

Cairns, J., & Plizzari, G. (2003). Towards a harmonised European bond test. *Materials and Structures*, *36*, 498–506. https://doi.org/10.1007/BF02480826

Cleary, D. B., & Ramirez, J. A. (1991). Bond strength of epoxy-coated reinforcement. *ACI Materials Journal*, *88*(2), 146–149.

Correlated Solutions, Inc. (2020a). Application Note AN-1701: Speckle Pattern Fundamentals.

Correlated Solutions, Inc. (2020b). VIC-2D Testing Guide. VIC-2D Testing Guide. Retrieved from http://www.correlatedsolutions.com/supportcontent/Vic-2D-v6-Testing-Guide.pdf

DalSoglio, M. (2017). *Final report: Investigation of bridge decks*. Montana Department of Transportation.

Dassault Systèmes Simulia Corp. (2014). Abaqus, F.E.A. Analysis User's Manual 6.14. Providence, RI.

Federal Highway Administration. (2019). *Bridge condition by highway system 2019*. Retrieved March 2021, from https://www.fhwa.dot.gov/bridge/nbi/no10/condition19.cfm

Frosch, R., Gutierrez, S., & Hoffman, J. (2010). *Control and repair of bridge deck cracking*. Purdue University. https://doi.org/10.5703/1288284314267

Gadelmawla, E. S., Koura, M. M., Maksoud, T. M., Elewa, I. M., & Soliman, H. H. (2002). Roughness parameters. *Journal of Materials Processing Technology*, *123*(1), 133–145. https://doi.org/10.1016/S0924-0136(02)00060-2

Gencturk, B., Hossain, K., Kapadia, A., Labib, E., & Mo, Y.-L. (2014). Use of digital image correlation technique in full-scale testing. *Measurement*, *47*, 505–515. https://doi.org/10.1016/j.measurement.2013.09.018

Gilbert, R. I. (1992). Shrinkage cracking in fully restrained concrete members. *ACI Structural Journal*, *89*(2), 141–149.

Hognestad, E., Hanson, N., & McHenry, D. (1955). Concrete stress distribution in ultimate strength design. *Journal Proceedings*, *52*(12), 455–480.

Idun, E. K., & Darwin, D. (1999). Bond of epoxy-coated reinforcement: Coefficient of friction and rib face angle. *ACI Structural Journal*, *96*(4), 609–615.

Illinois Department of Transportation. (2016). *Standard specifications for road and bridge construction*. Illinois Department of Transportation.

International Organization for Standardization. (1996a). *ISO 3274: Geometrical Product Specifications (GPS) - Surface texture: Profile method - Nominal characteristics of contact (stylus) instruments*.

International Organization for Standardization. (1996b). *ISO 4288: Geometrical Product Specifications (GPS) - Surface texture: Profile method - Rules and procedures for the assessment of surface texture*.

International Organization for Standardization. (2011). *ISO 16610-21: Geometrical product specifications (GPS) - Filtration - Part 21: Linear profile filters: Gaussian filters*.

Krauss, P., & Rogalla, E. (1996). *Transverse cracking in newly constructed bridge decks*. Transportation Research Board.

Lundgren, K. (2005). Bond between ribbed bars and concrete. Part 1: Modified model. *Magazine of Concrete Research*, *57*(7), 371–382.

National Centers for Environmental Information. (2020). National Temperature and Precipitation Maps. Retrieved December 2020, from Temperature, Precipitation, and Drought: https://www.ncdc.noaa.gov/temp-and-precip/us-maps/1/202011?products[]=tmax#maps

RILEM. (1994). Bond test for reinforcement steel. 2. Pull-out test. In *s. d. Réunion Internationale des Laboratoires et Experts des Matériaux, RILEM Technical Recommendations for the Testing and Use of Construction Materials* (pp. 218–220). Taylor & Francis Group.

Saadeghvaziri, A., & Hadidi, R. (2005). Transverse cracking of concrete bridge decks: Effects of design factors. *Journal of Bridge Engineering*, *10*(5), 511–519. https://doi.org/10.1061/(ASCE)1084-0702(2005)10:5(511)

Salmanpour, A. H., & Mojsilović, N. (2013). *Application of Digital Image Correlation for strain measurements of large masonry walls*. Singapore.

Tazawa, E.-i., & Miyazawa, S. (1995). Experimental study on mechanism of autogenous shrinkage of concrete. *Cement and Concrete Research*, *25*(8), 1633–1638. https://doi.org/10.1016/0008-8846(95)00159-X

Treece, R. A., & Jirsa, J. O. (1989). Bond strength of epoxy-coated reinforcing bars. *ACI Materials Journal*, *86*(2), 167–174.

Xiong, Y., Wang, K., Liu, Z., & Yang, Z. (2016). Effect of coating thickness on bond behaviors of polymer cement coated plain steel bar with concrete and finite element modeling. *The Open Civil Engineering Journal*, 571–577.

Young, H., & Freedman, R. (2016). *University physics with modern physics*, 14th ed. Pearson.

APPENDIX A: STRAIN DEVELOPMENT OBTAINED FROM DIC AT STAGE 3 OF THE SHRINKAGE TEST

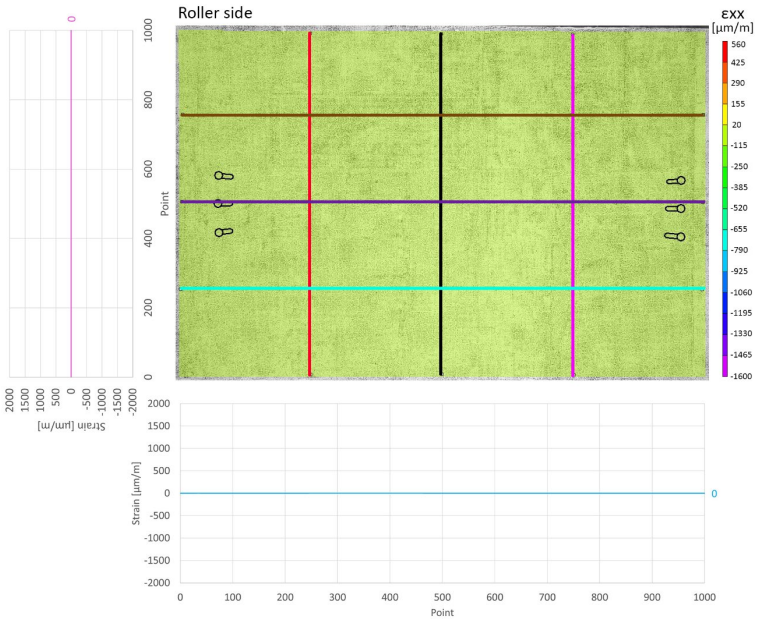

A. EC specimen.

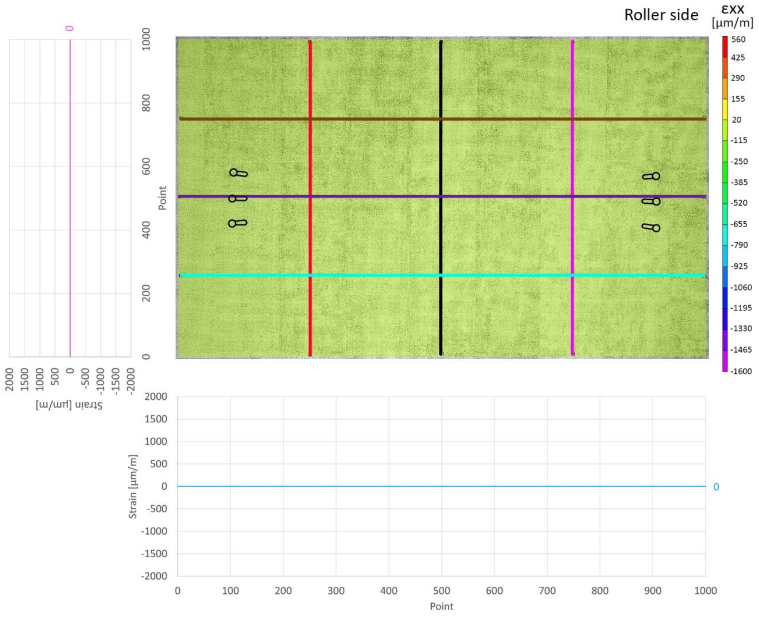

B. TEC specimen.

Figure 54. Illustration. Longitudinal strain values, ε_{xx}, at stage 3 of the drying shrinkage test. (Pictures taken in the evening of November 11, 2020.)

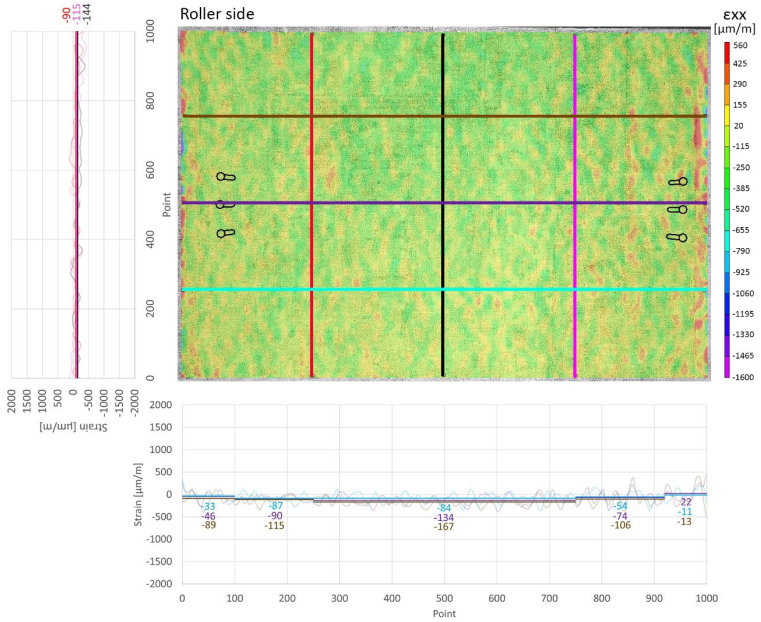

A. EC specimen.

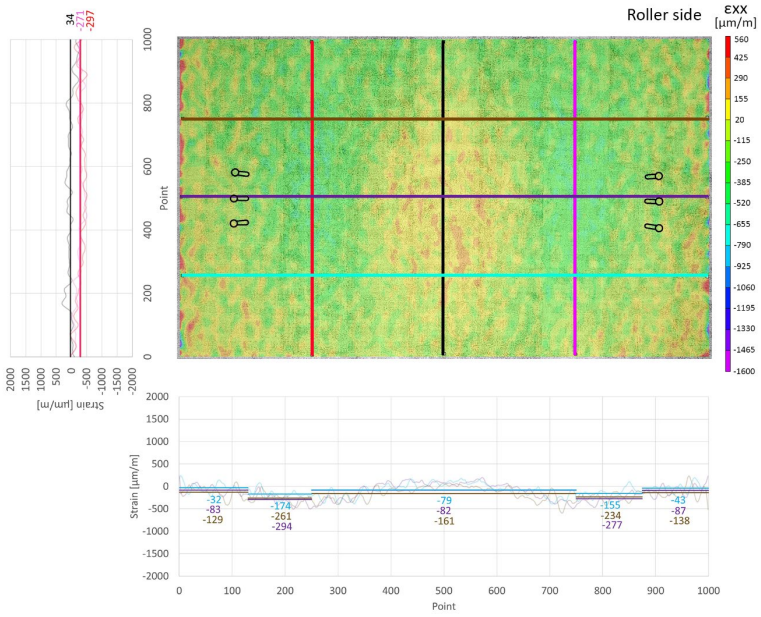

B. TEC specimen.

Figure 55. Illustration. Longitudinal strain values, ε_{xx}, at stage 3 of the drying shrinkage test. (Pictures taken in the morning of November 14, 2020.)

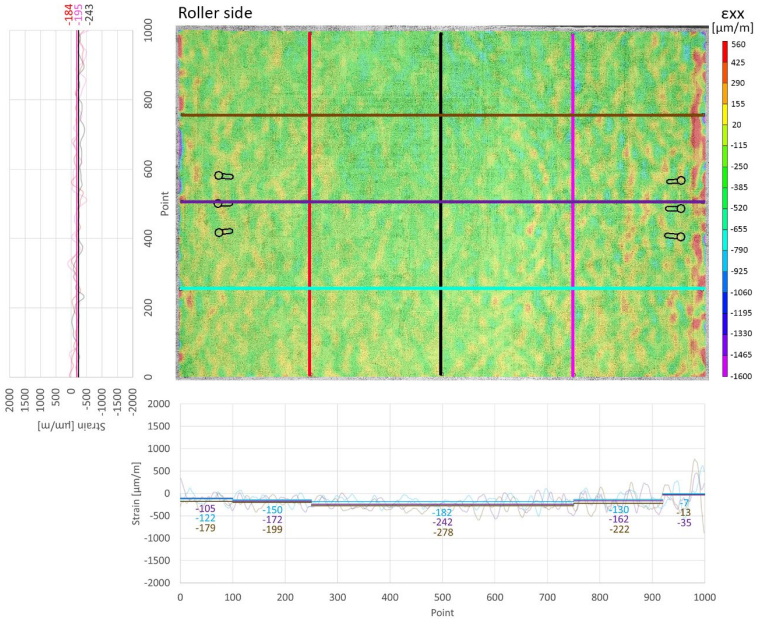

A. EC specimen.

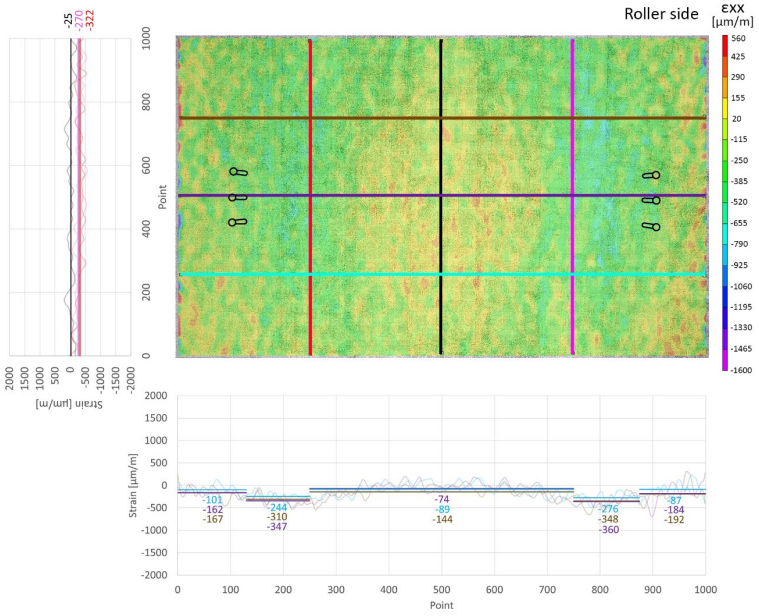

B. TEC specimen.

Figure 56. Illustration. Longitudinal strain values, ε_{xx}, at stage 3 of the drying shrinkage test. (Pictures taken in the morning of November 17, 2020.)

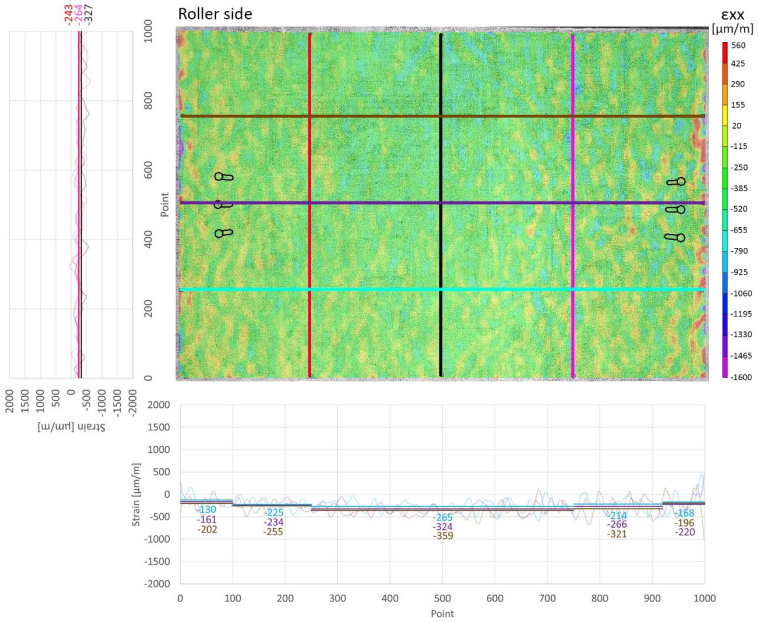

A. EC specimen.

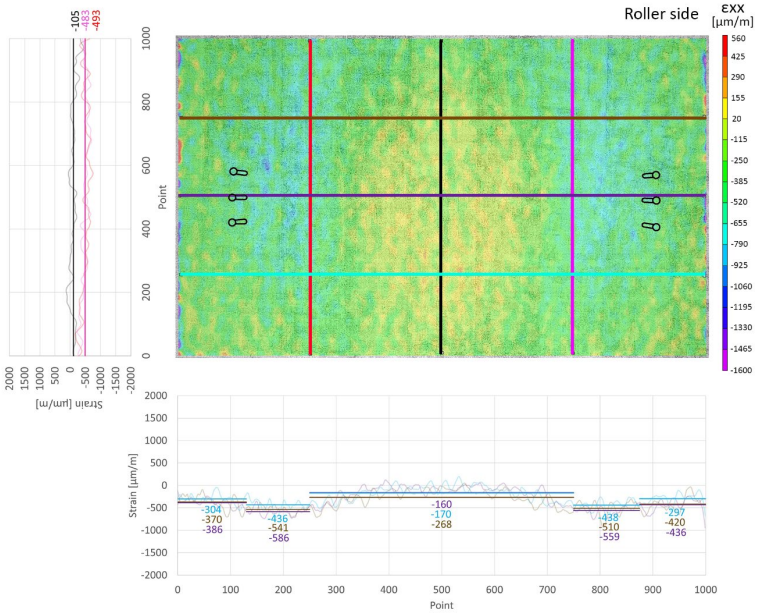

B. TEC specimen.

Figure 57. Illustration. Longitudinal strain values, ε_{xx}, at stage 3 of the drying shrinkage test. (Pictures taken in the morning of November 20, 2020.)

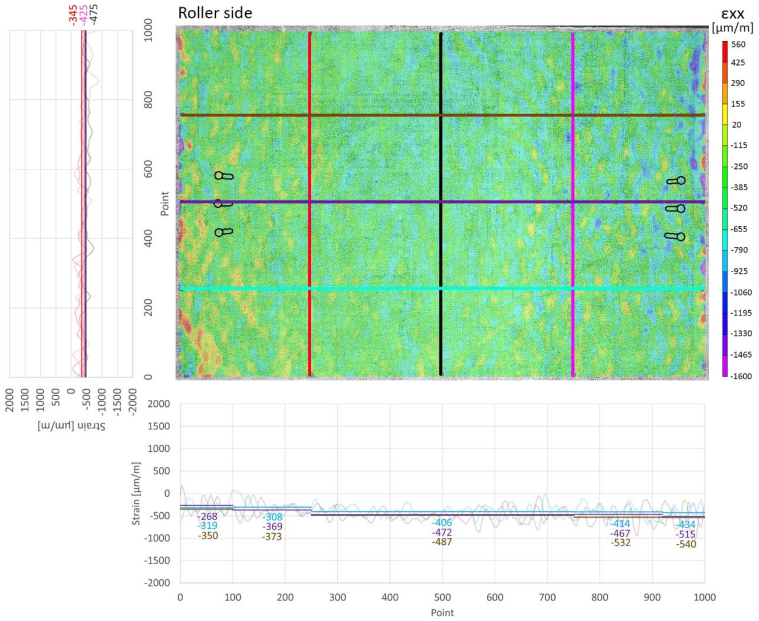

A. EC specimen.

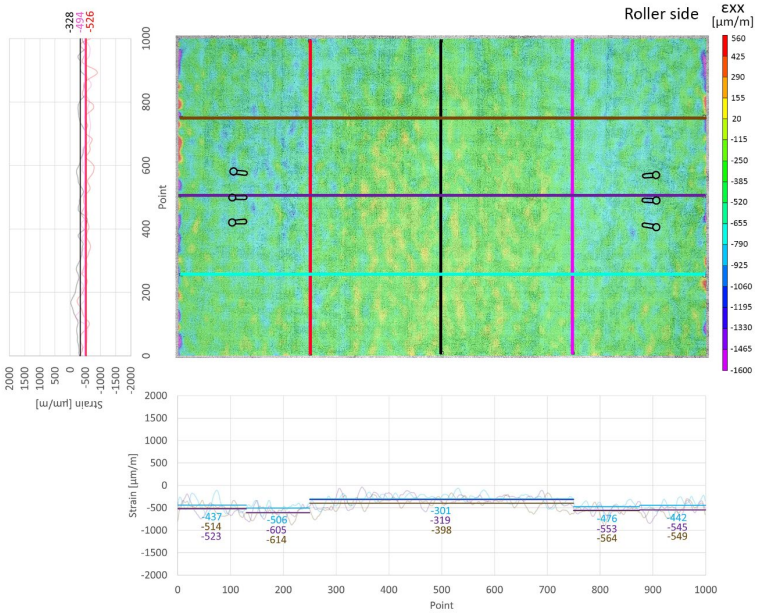

B. TEC specimen.

Figure 58. Illustration. Longitudinal strain values, ε_{xx}, at stage 3 of the drying shrinkage test. (Pictures taken in the morning of November 24, 2020.)

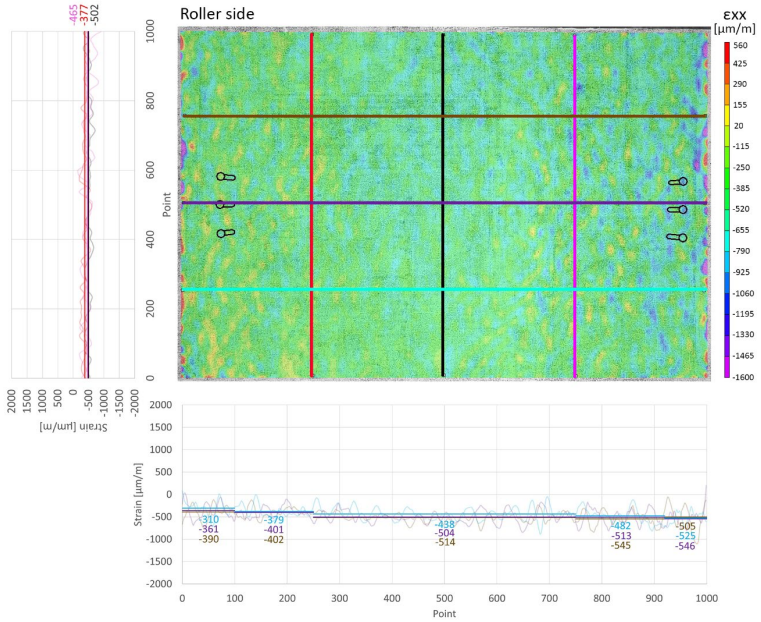

A. EC specimen.

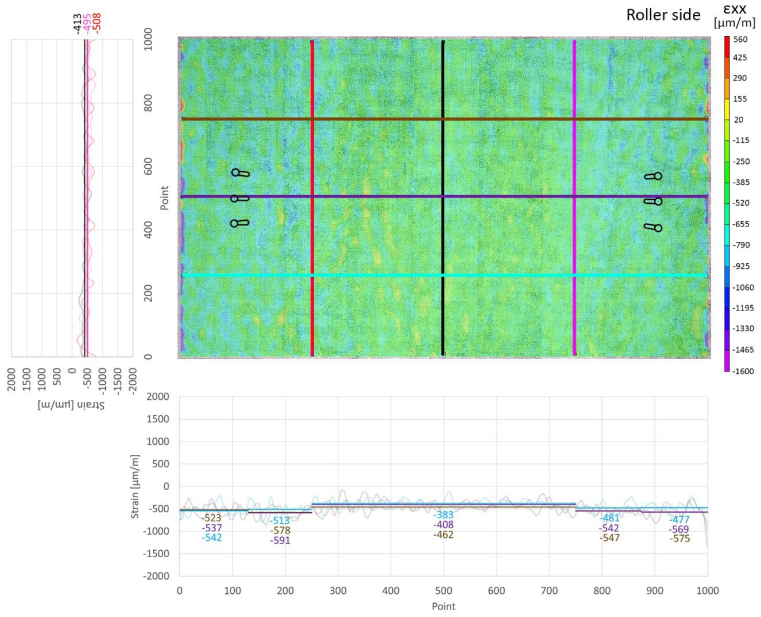

B. TEC specimen.

Figure 59. Illustration. Longitudinal strain values, ε_{xx}, at stage 3 of the drying shrinkage test. (Pictures taken in the morning of November 27, 2020.)

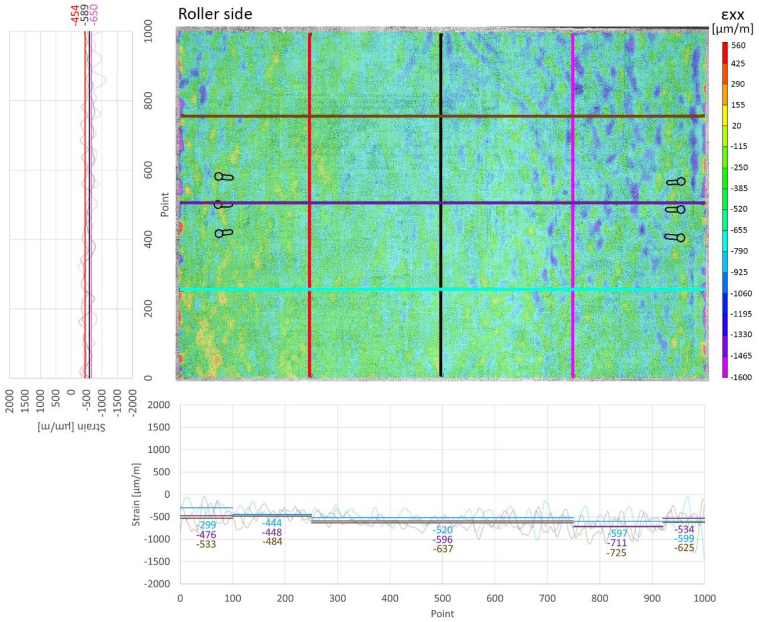

A. EC specimen.

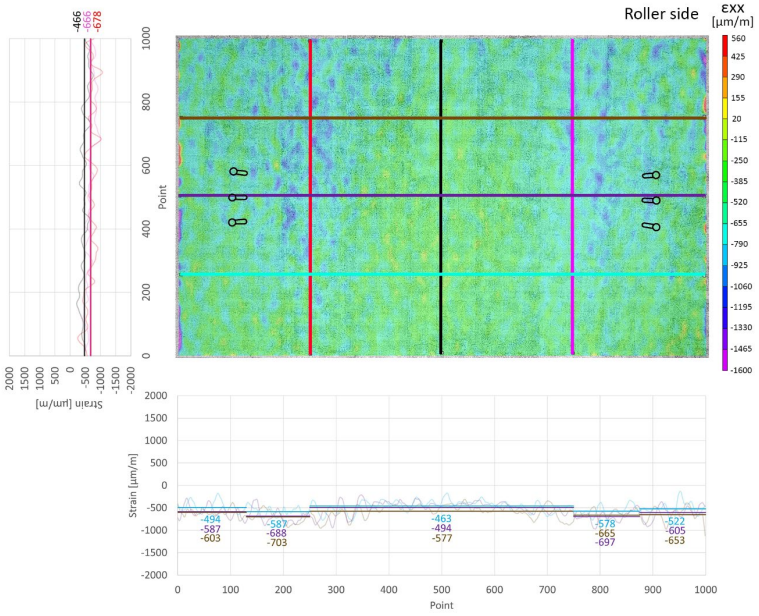

B. TEC specimen.

Figure 60. Illustration. Longitudinal strain values, ε_{xx}, at stage 3 of the drying shrinkage test. (Pictures taken in the morning of November 30, 2020.)

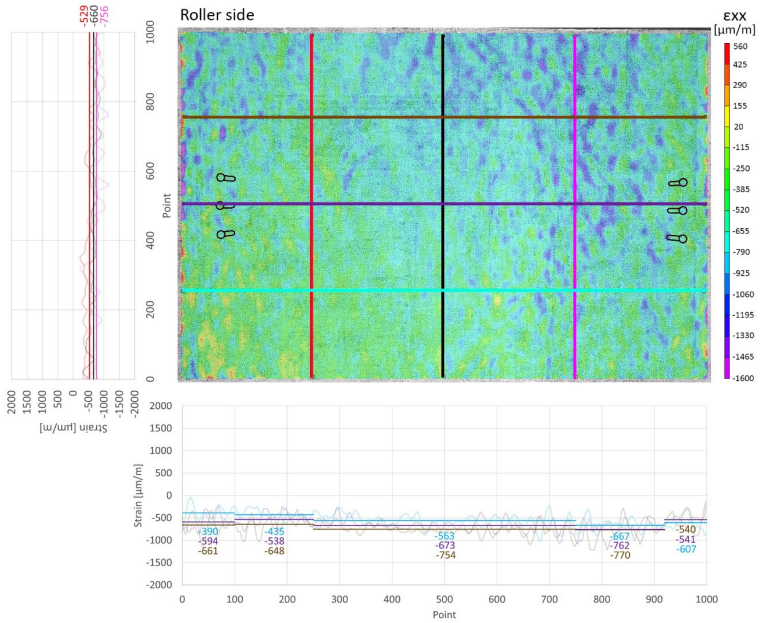

A. EC specimen.

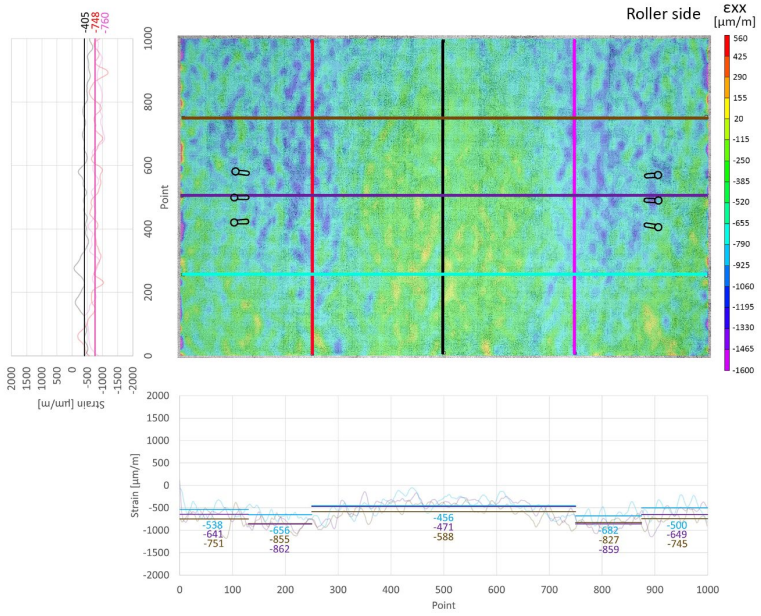

B. TEC specimen.

Figure 61. Illustration. Longitudinal strain values, ε_{xx}, at stage 3 of the drying shrinkage test. (Pictures taken in the morning of December 3, 2020.)

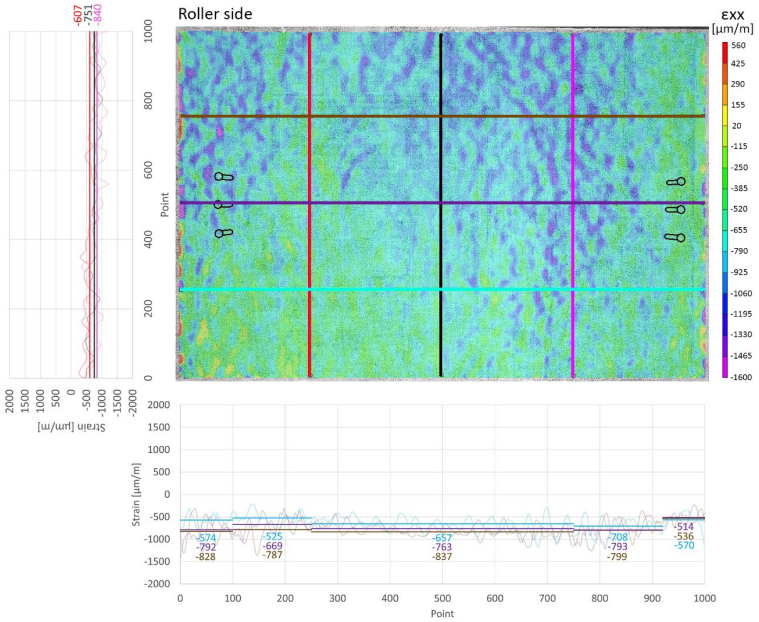

A. EC specimen.

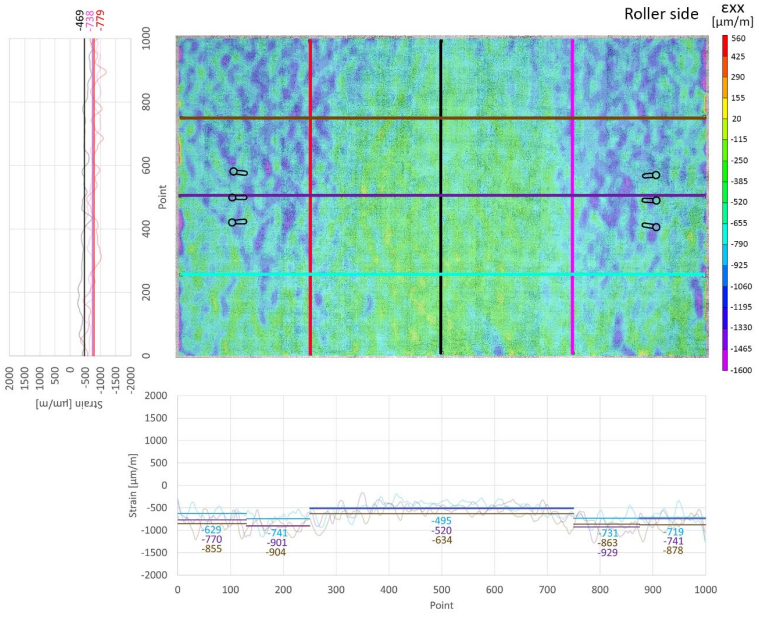

B. TEC specimen.

Figure 62. Illustration. Longitudinal strain values, ε_{xx}, at stage 3 of the drying shrinkage test. (Pictures taken in the morning of December 7, 2020.)

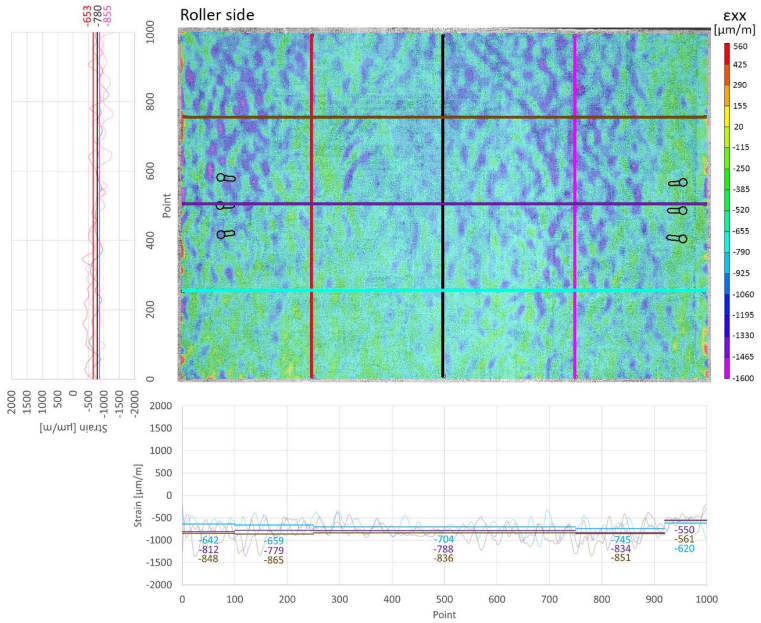

A. EC specimen.

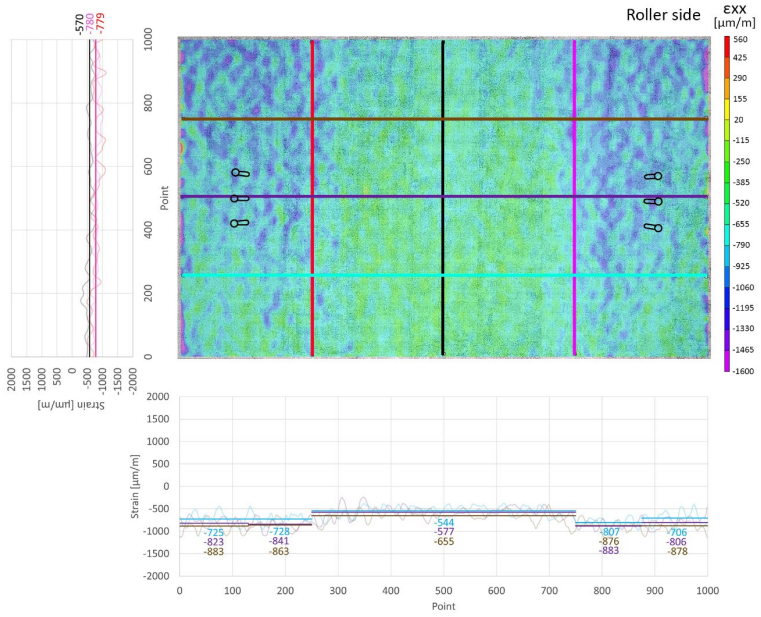

B. TEC specimen.

Figure 63. Illustration. Longitudinal strain values, ε_{xx}, at stage 3 of the drying shrinkage test. (Pictures taken in the morning of December 11, 2020.)

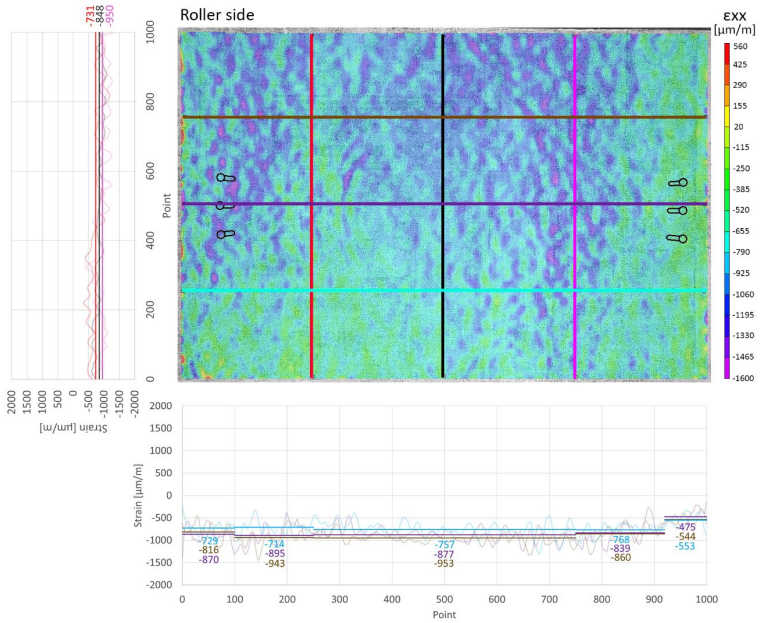

A. EC specimen.

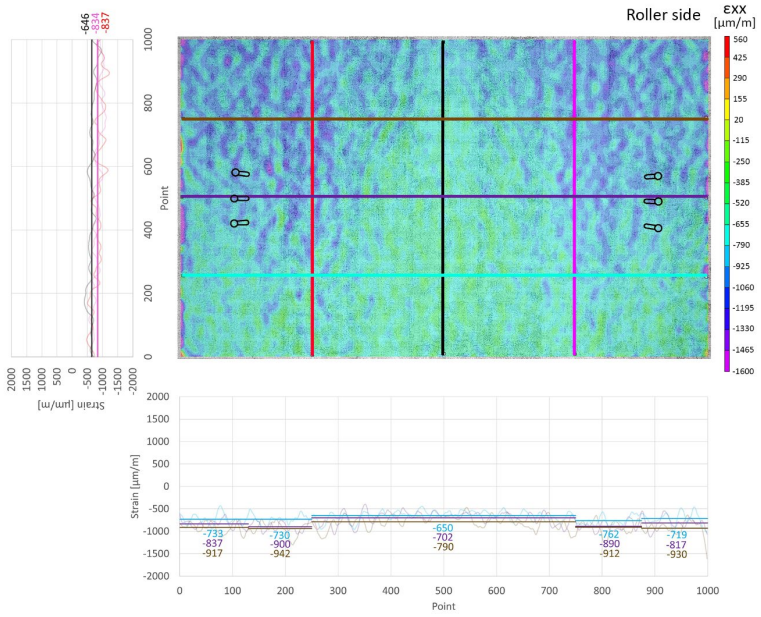

B. TEC specimen.

Figure 64. Illustration. Longitudinal strain values, ε_{xx}, at stage 3 of the drying shrinkage test. (Pictures taken in the morning of December 15, 2020.)

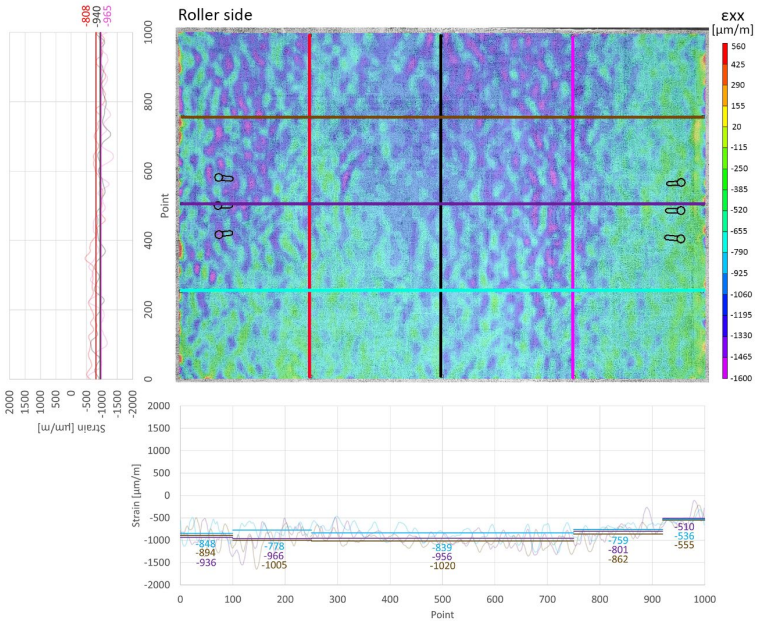

A. EC specimen.

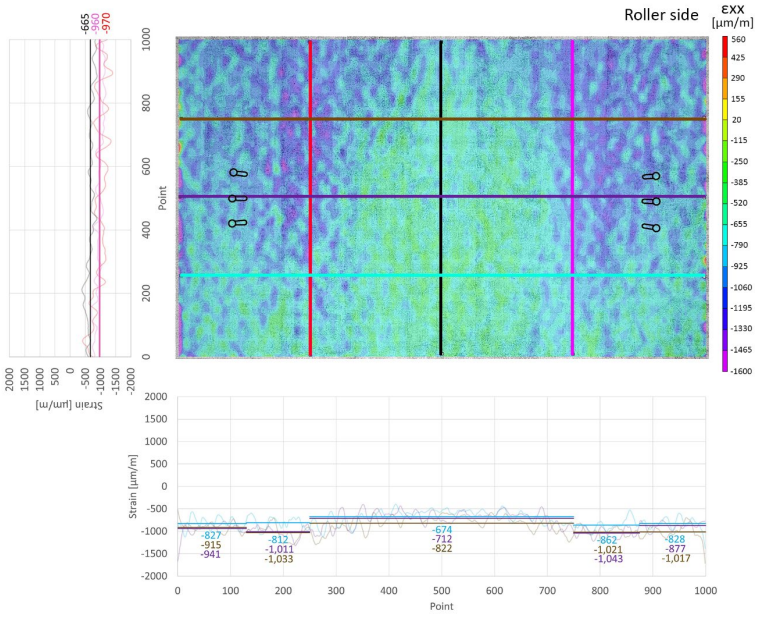

B. TEC specimen.

Figure 65. Illustration. Longitudinal strain values, ε_{xx}, at stage 3 of the drying shrinkage test. (Pictures taken in the morning of December 19, 2020.)

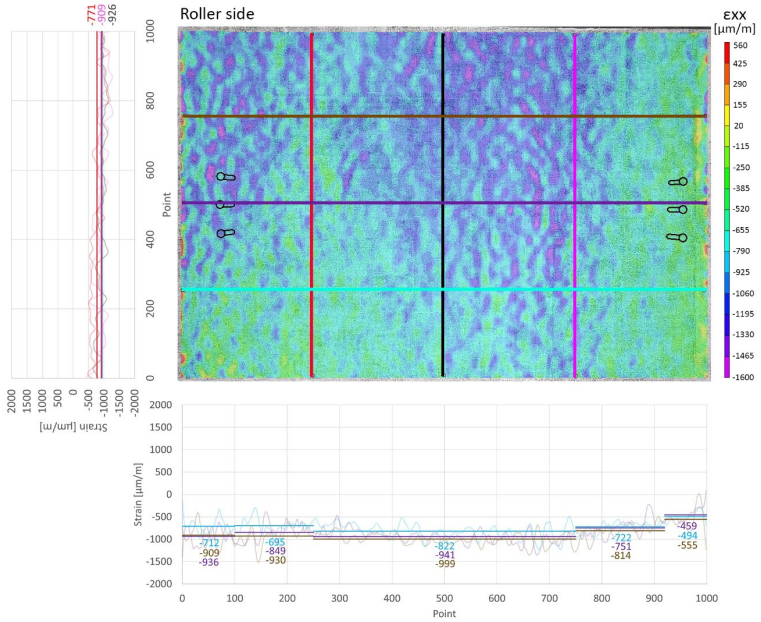

A. EC specimen.

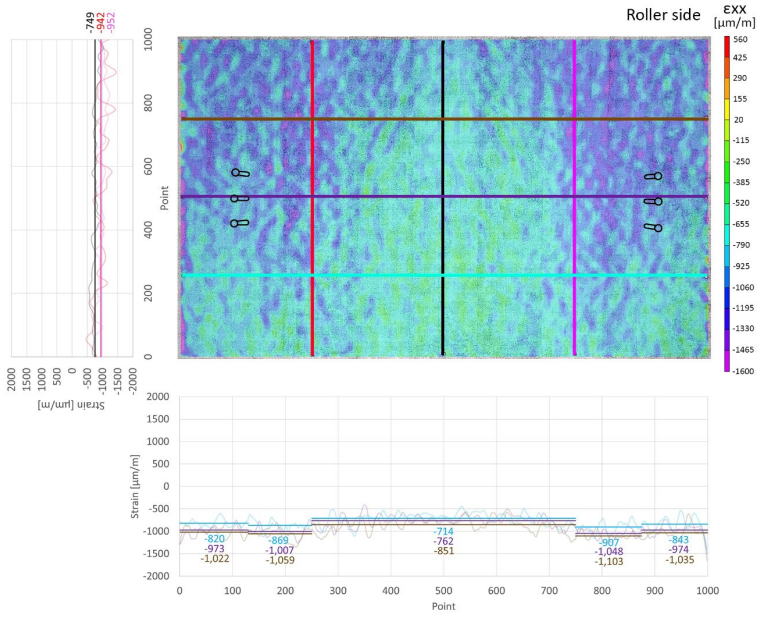

B. TEC specimen.

Figure 66. Illustration. Longitudinal strain values, ε_{xx}, at stage 3 of the drying shrinkage test. (Pictures taken in the morning of December 23, 2020.)

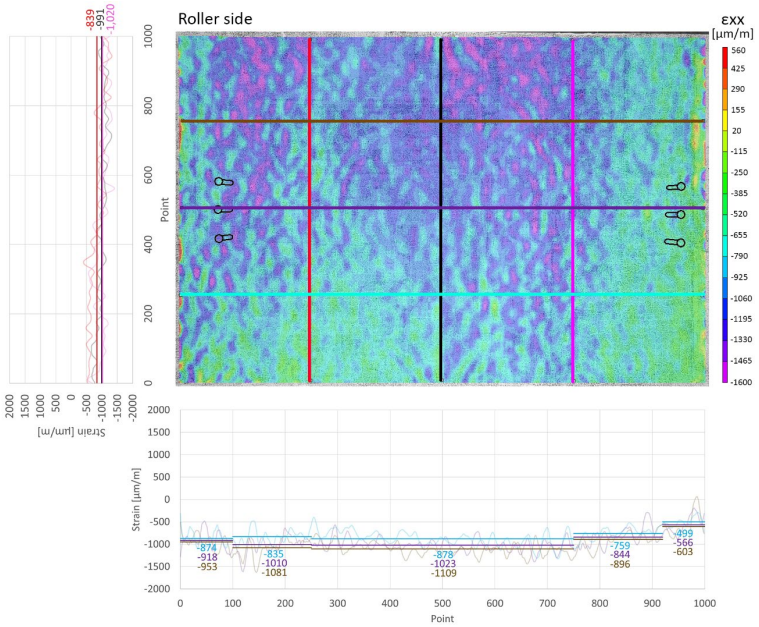

A. EC specimen.

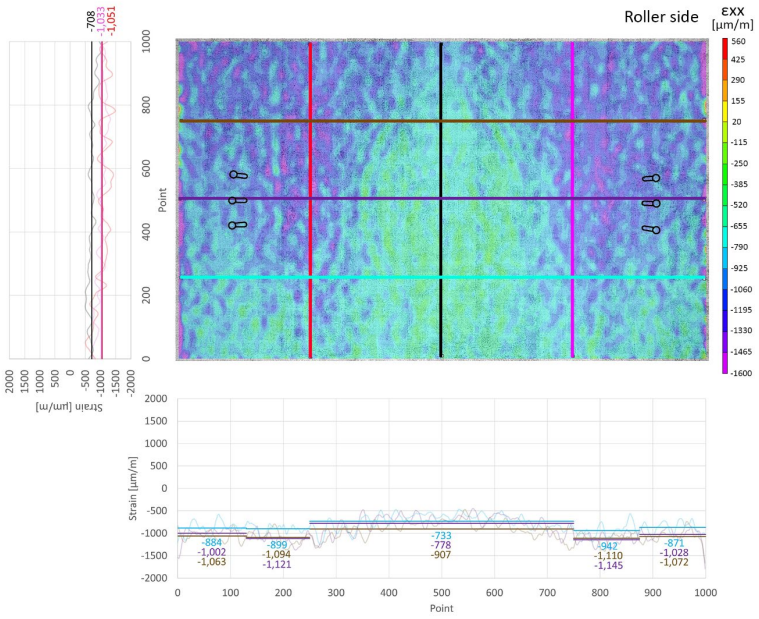

B. TEC specimen.

Figure 67. Illustration. Longitudinal strain values, ε_{xx}, at stage 3 of the drying shrinkage test. (Pictures taken in the morning of December 27, 2020.)

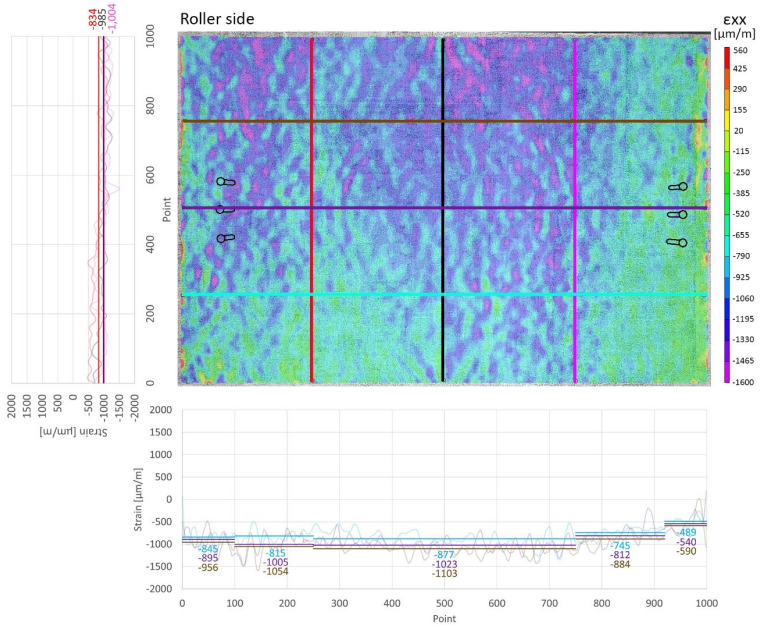

A. EC specimen.

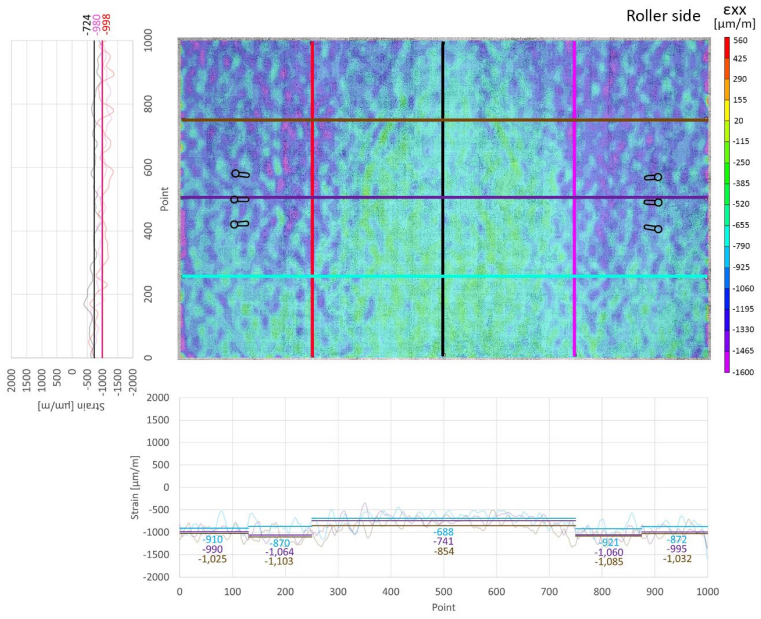

B. TEC specimen.

Figure 68. Illustration. Longitudinal strain values, ε_{xx}, at stage 3 of the drying shrinkage test. (Pictures taken in the morning of December 31, 2020.)

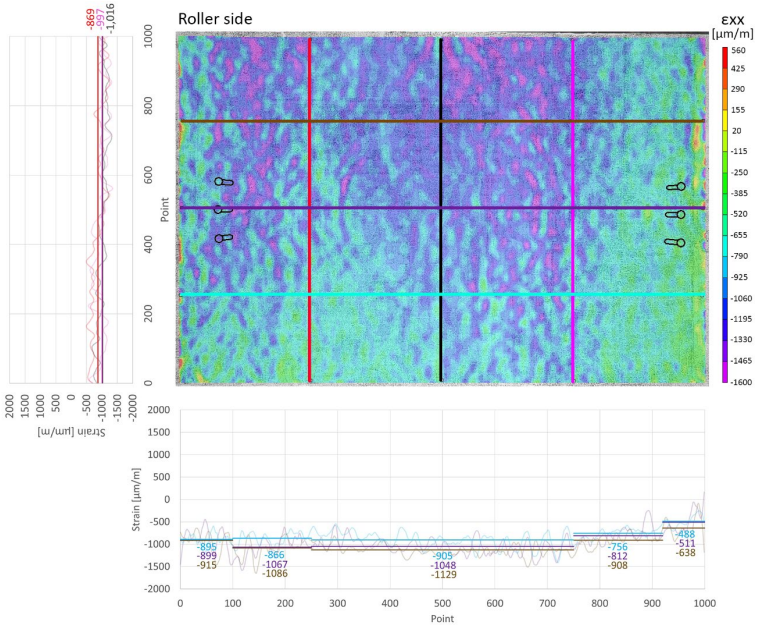

A. EC specimen.

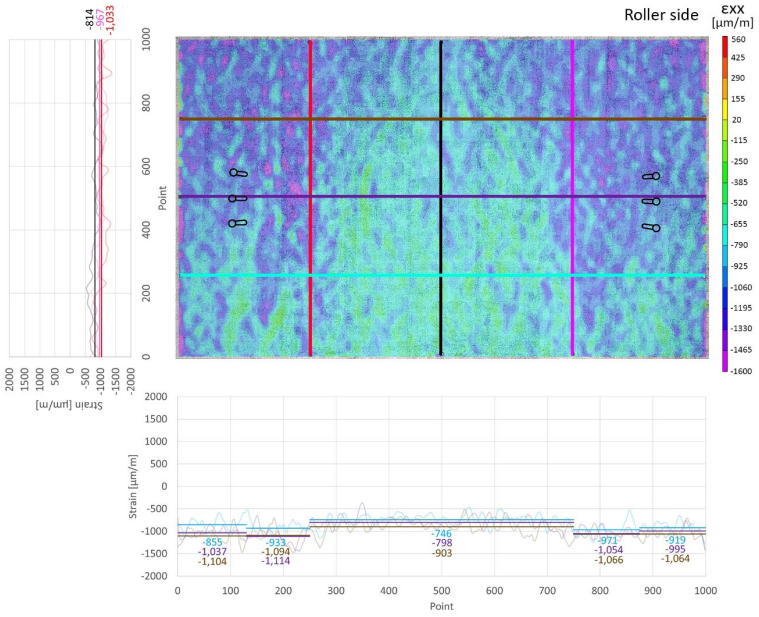

B. TEC specimen.

Figure 69. Illustration. Longitudinal strain values, ε_{xx}, at stage 3 of the drying shrinkage test. (Pictures taken in the morning of January 4, 2021.)

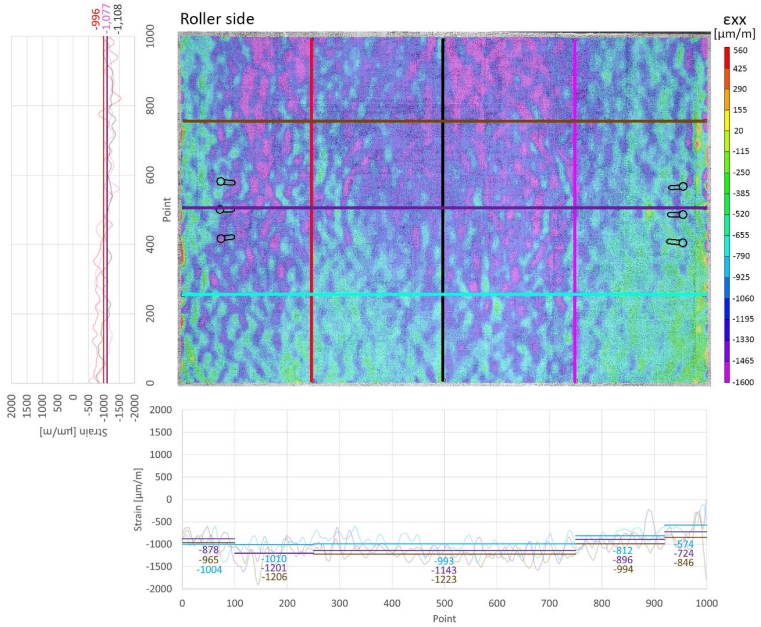

A. EC specimen.

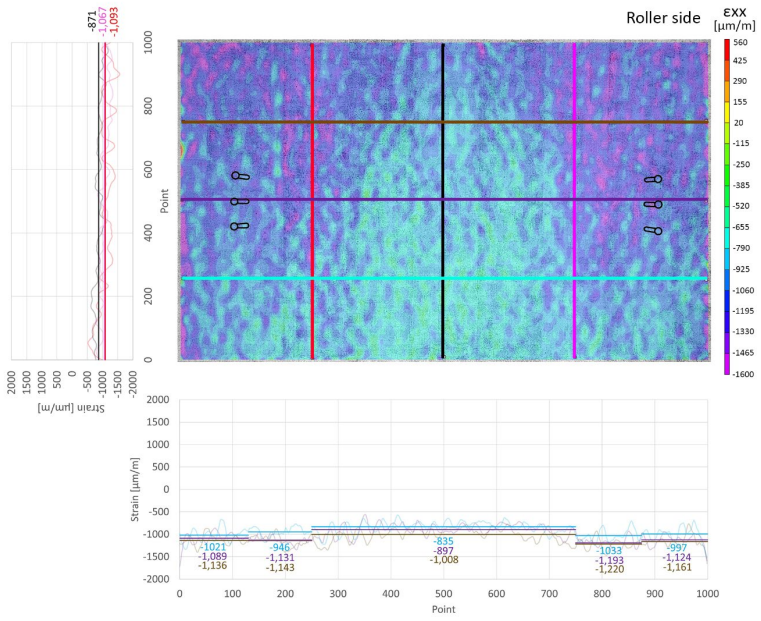

B. TEC specimen.

Figure 70. Illustration. Longitudinal strain values, ε_{xx}, at stage 3 of the drying shrinkage test. (Pictures taken in the morning of January 9, 2021.)

APPENDIX B: STRAIN DEVELOPMENT OF EC SPECIMEN OBTAINED FROM DIC DURING THE TEMPERATURE EFFECT SIMULATION TEST

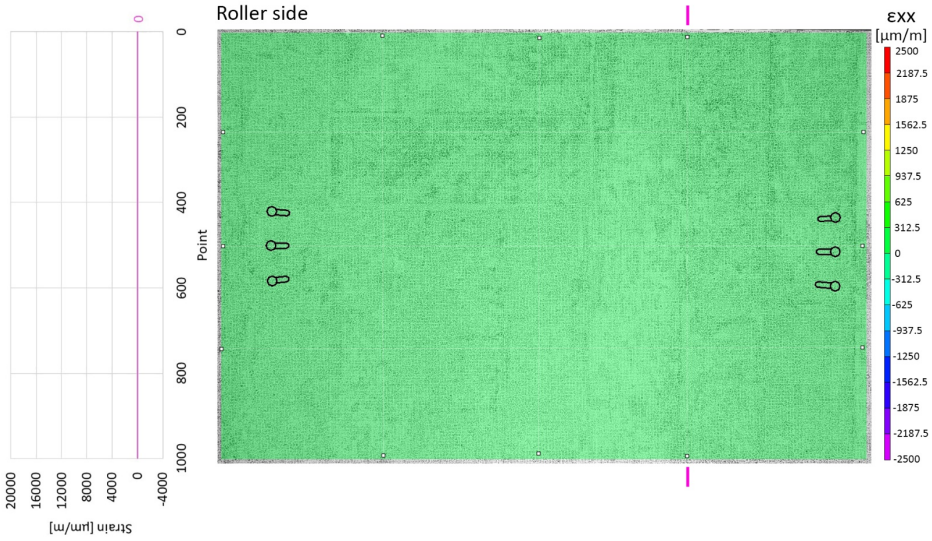

Figure 71. Illustration. Longitudinal strain on the EC specimen at 76.2°F (24.6°C).

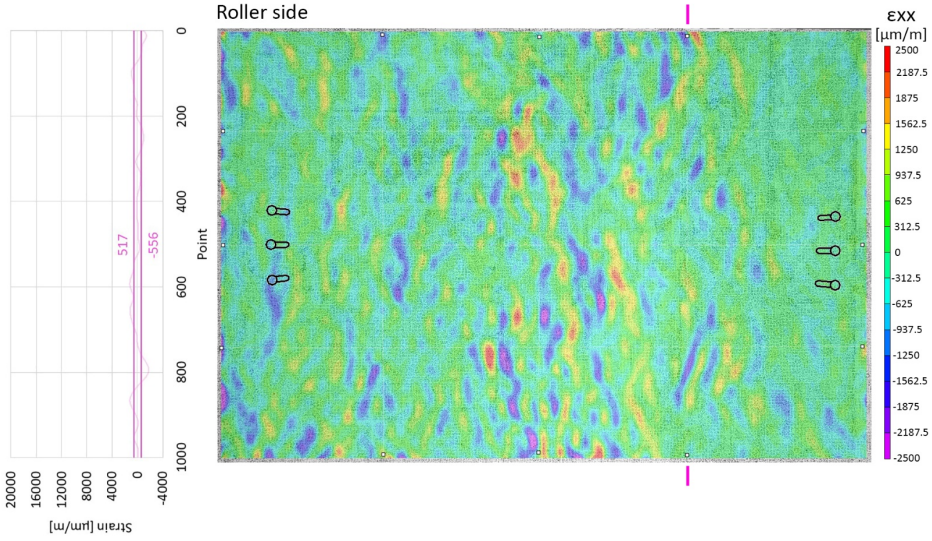

Figure 72. Illustration. Longitudinal strain on the EC specimen at 97.0°F (36.1°C).

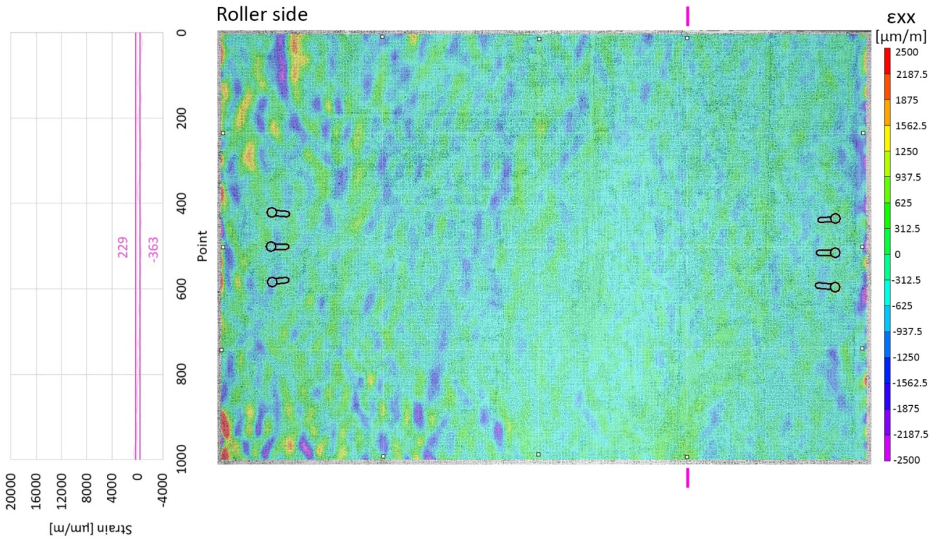

Figure 73. Illustration. Longitudinal strain on the EC specimen at 140.2°F (60.1°C).

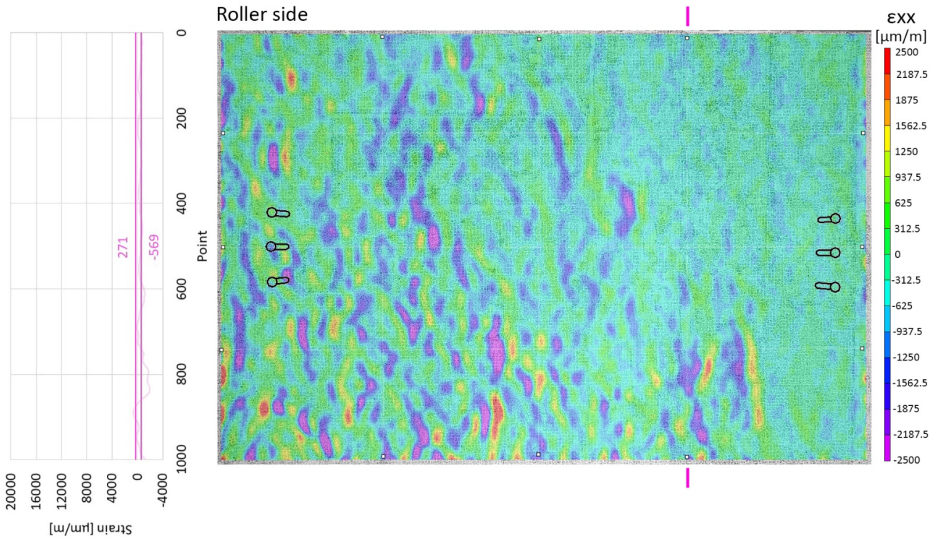

Figure 74. Illustration. Longitudinal strain on the EC specimen at 151.6°F (66.4°C).

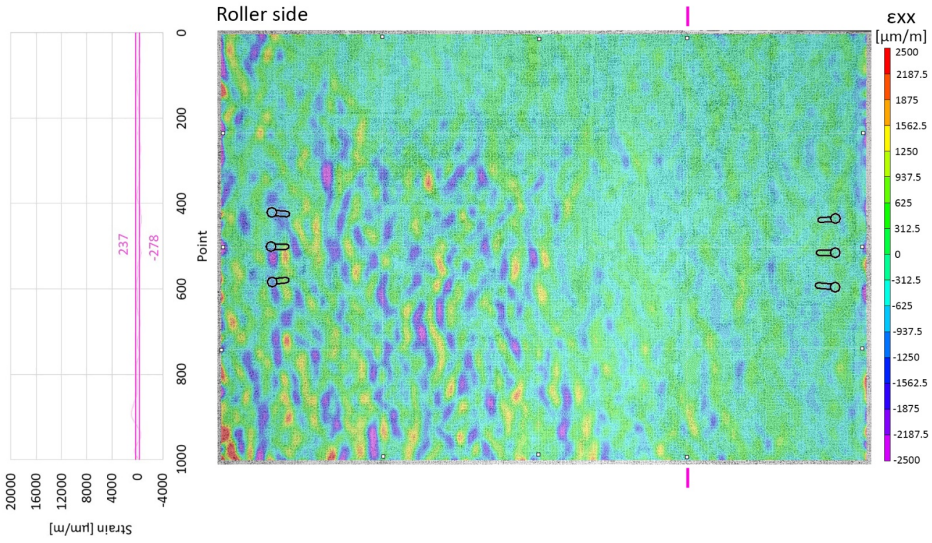

Figure 75. Illustration. Longitudinal strain on the EC specimen at 149.9°F (65.5°C).

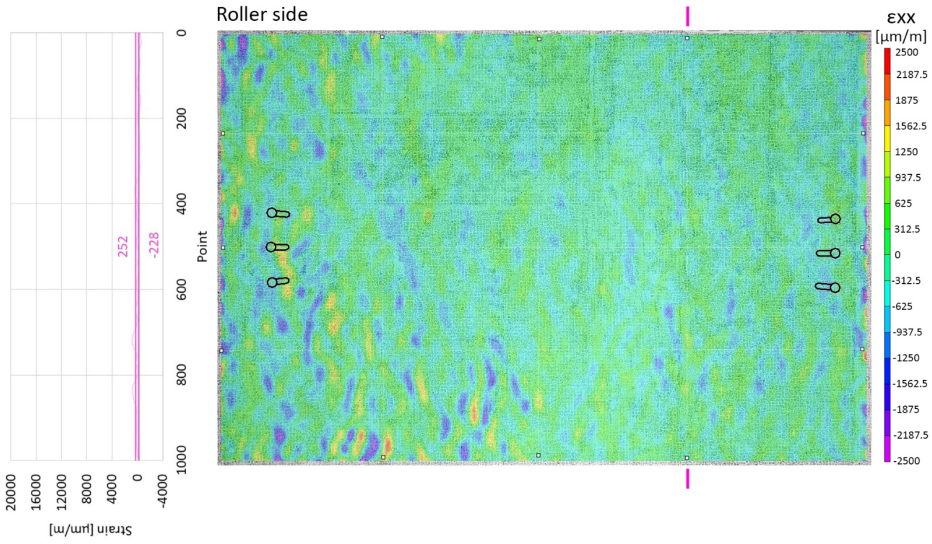

Figure 76. Illustration. Longitudinal strain on the EC specimen at 152.4°F (66.9°C).

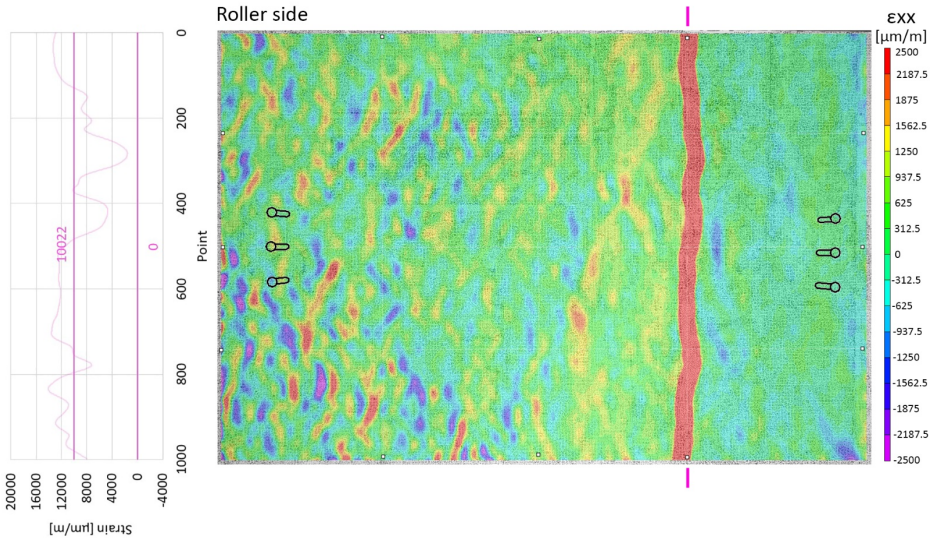

Figure 77. Illustration. Longitudinal strain on the EC specimen at 152.6°F (67.0°C), when the first crack occurred.

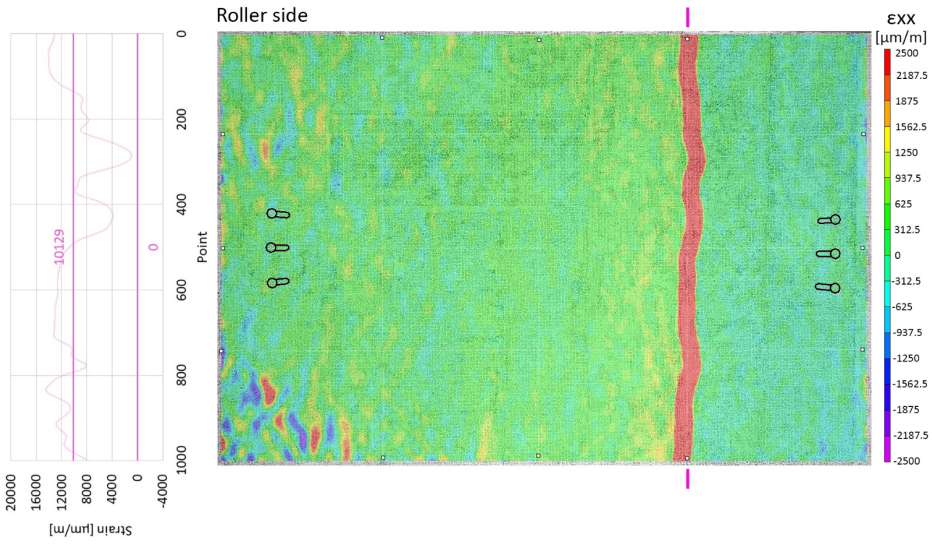

Figure 78. Illustration. Longitudinal strain on the EC specimen at 152.5°F (66.9°C).

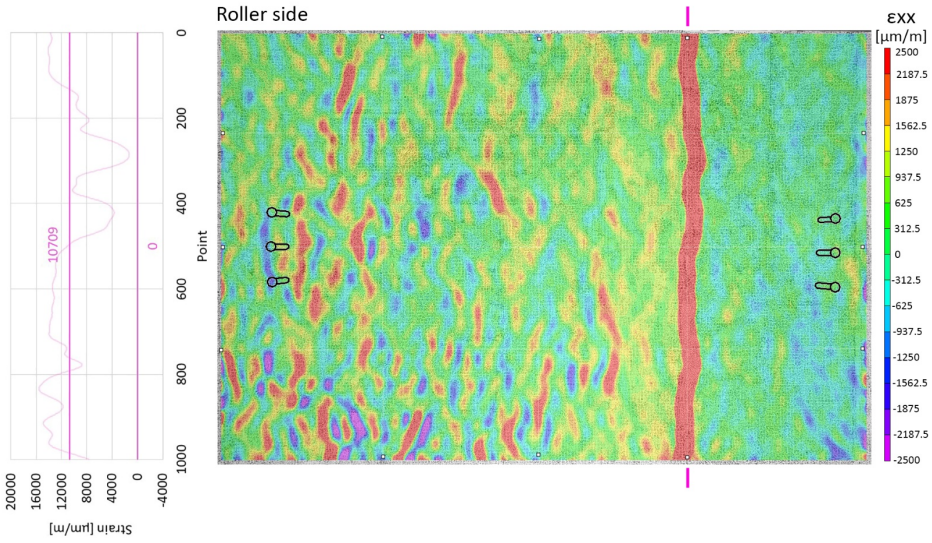

Figure 79. Illustration. Longitudinal strain on the EC specimen at 152.9°F (67.2°C), when the second crack occurred.

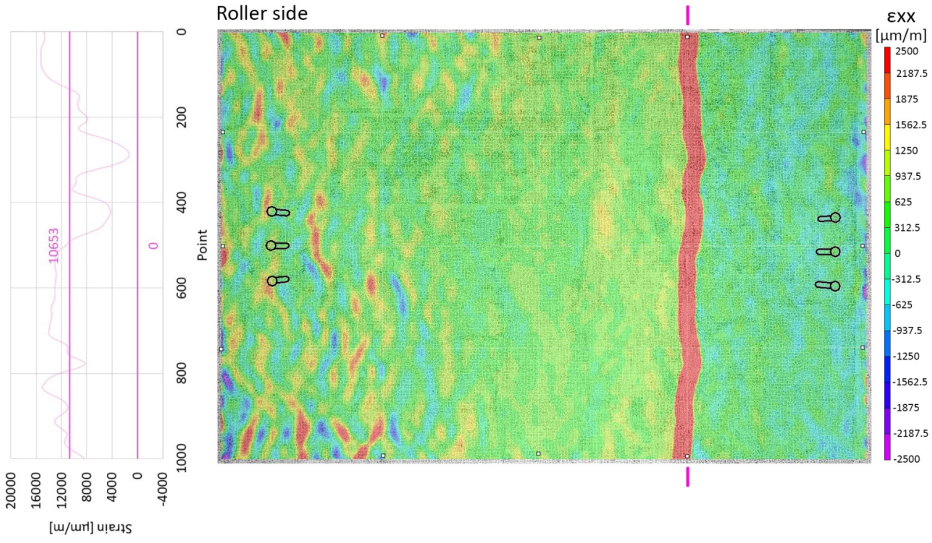

Figure 80. Illustration. Longitudinal strain on the EC specimen at 150.2°F (65.7°C).

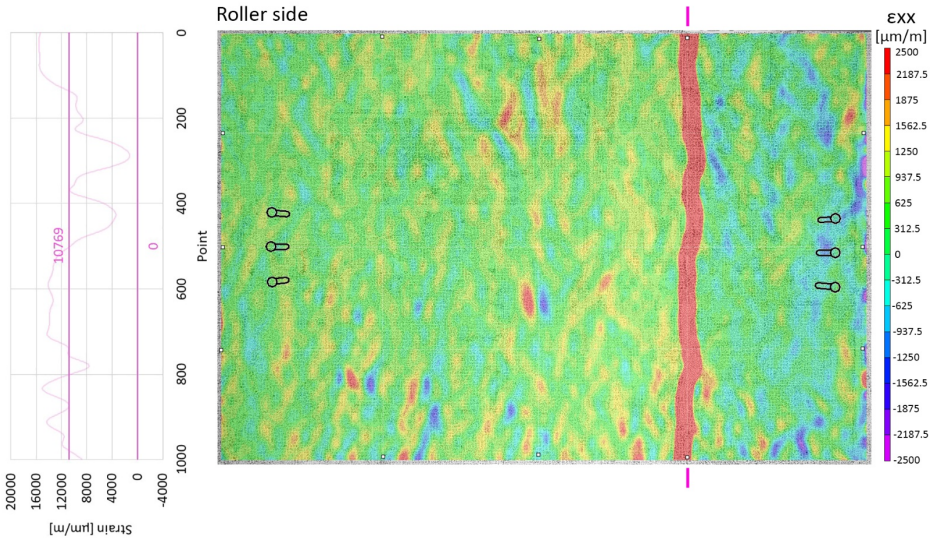

Figure 81. Illustration. Longitudinal strain on the EC specimen at 151.3°F (66.3°C).

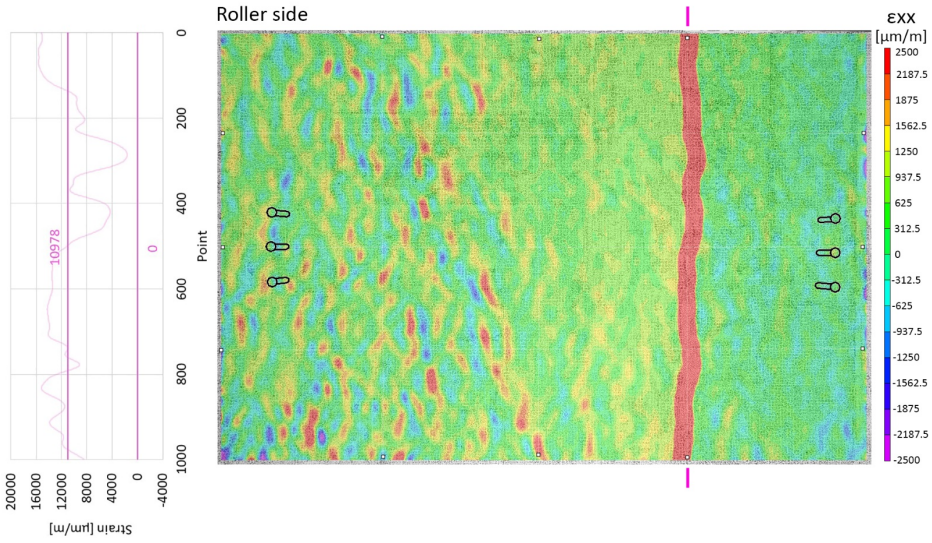

Figure 82. Illustration. Longitudinal strain on the EC specimen at 152.4°F (66.9°C).

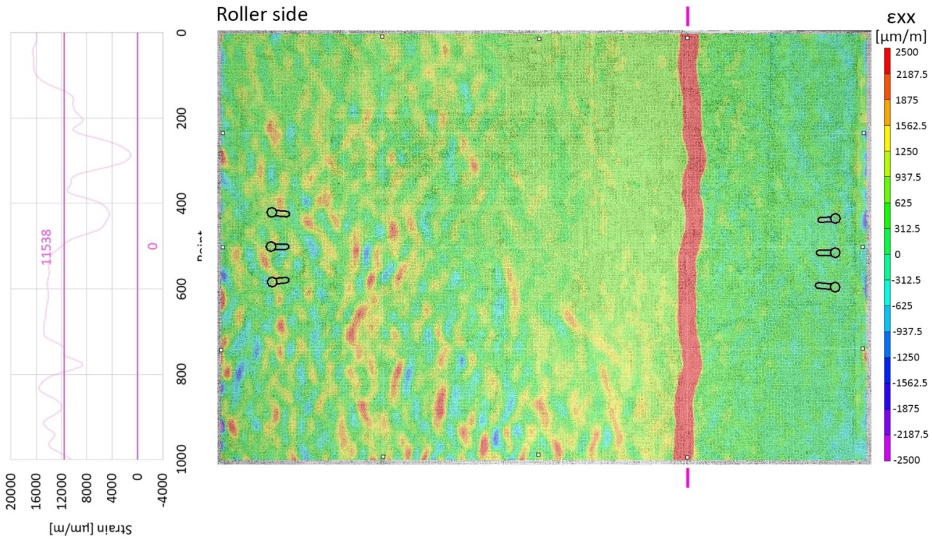

Figure 83. Illustration. Longitudinal strain on the EC specimen at 153.0°F (67.2°C), when the burners were turned off.

Figure 84. Illustration. Longitudinal strain on the EC specimen at 124.9°F (51.6°C), during the cooling stage.

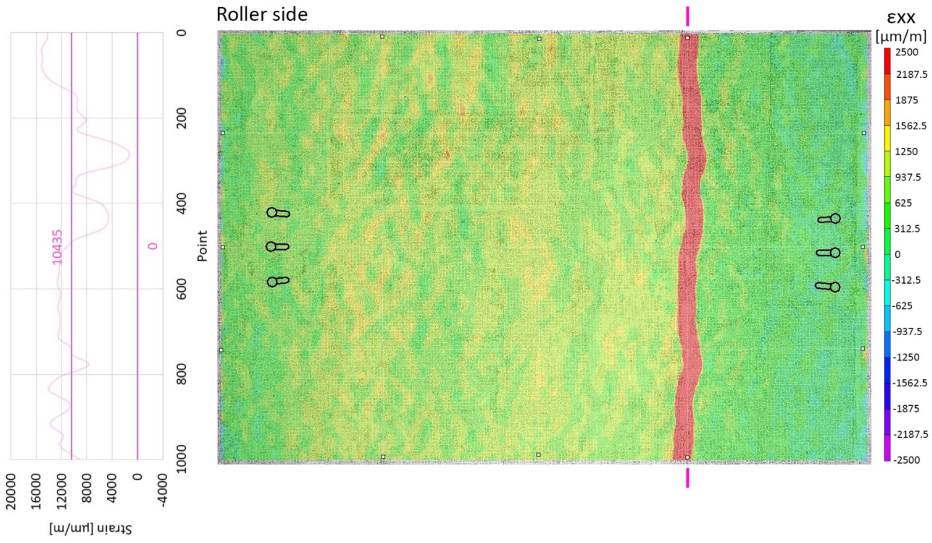

Figure 85. Illustration. Longitudinal strain on the EC specimen at 109.8°F (43.2°C).

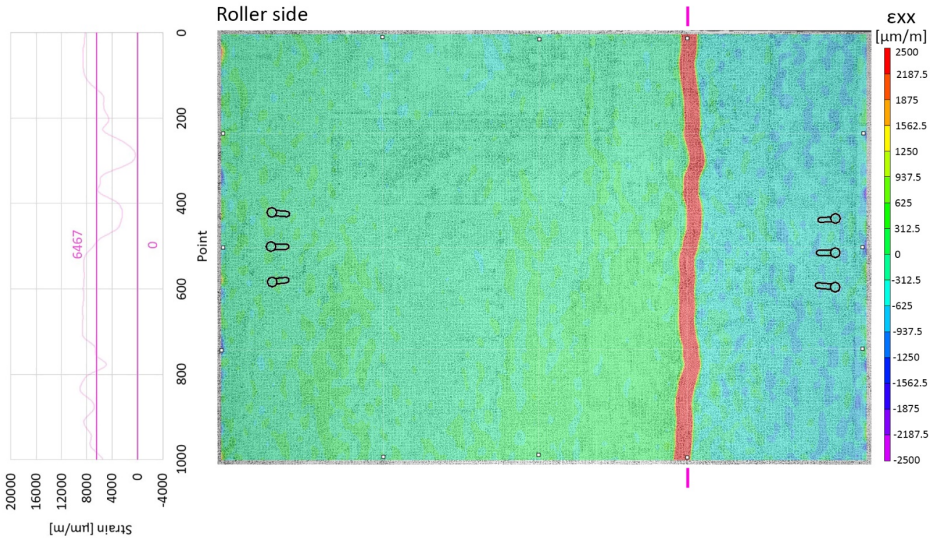

Figure 86. Illustration. Longitudinal strain on the EC specimen at 78.2°F (25.6°C).

APPENDIX C: STRAIN DEVELOPMENT OF TEC SPECIMEN OBTAINED FROM DIC DURING THE TEMPERATURE EFFECT SIMULATION TEST

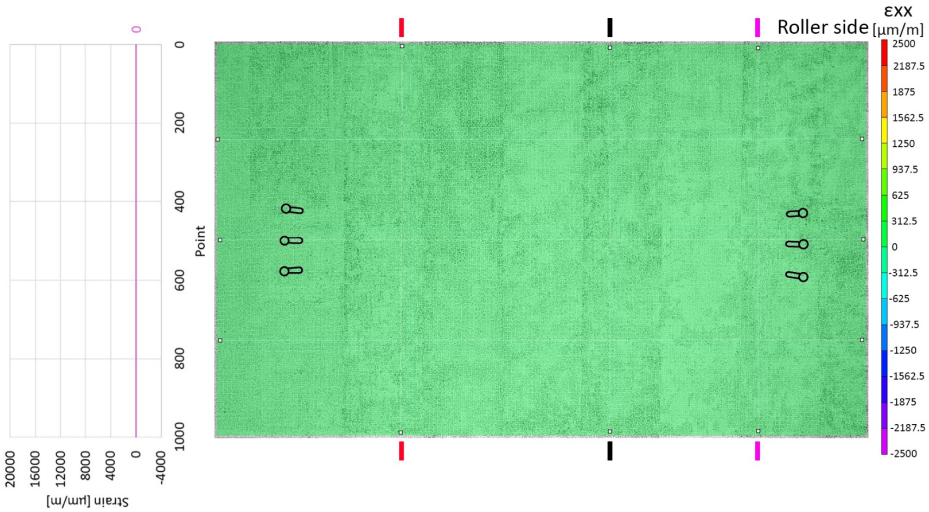

Figure 87. Illustration. Longitudinal strain on the TEC specimen at 80.2°F (26.7°C).

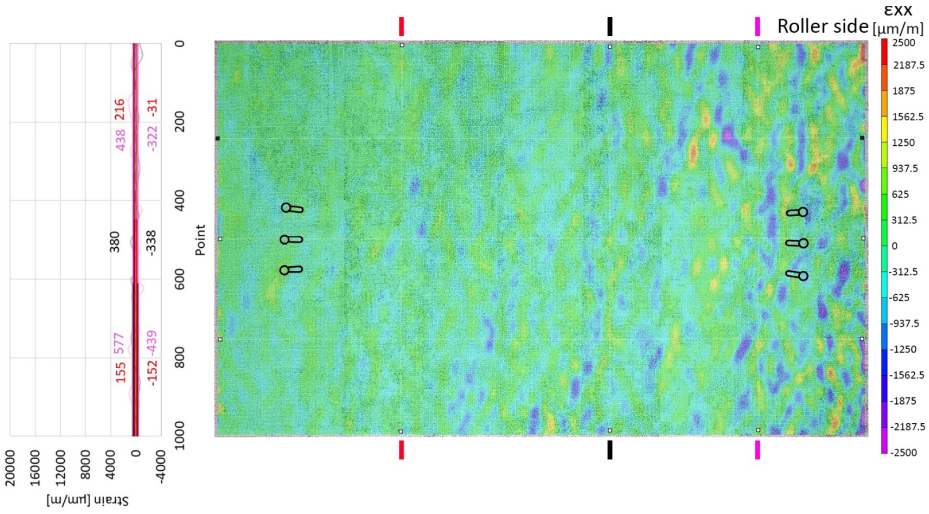

Figure 88. Illustration. Longitudinal strain on the TEC specimen at 99.8°F (37.6°C).

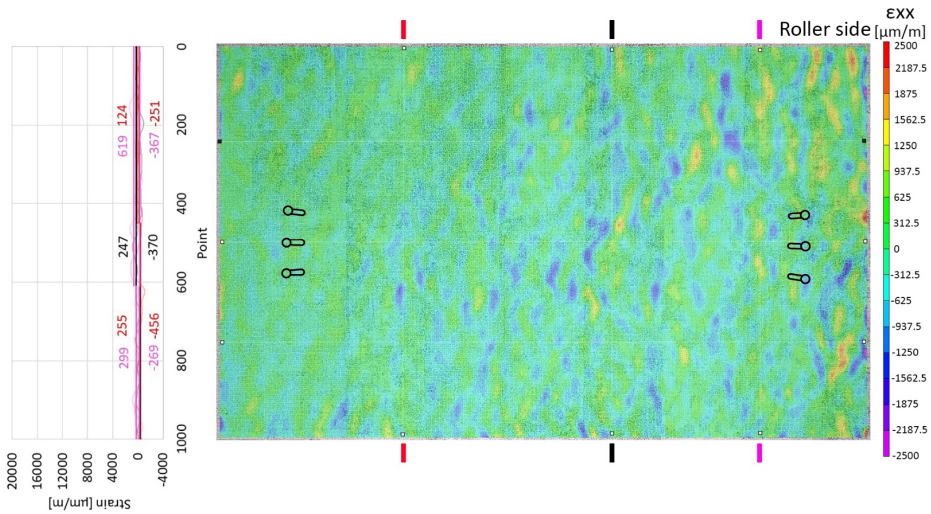

Figure 89. Illustration. Longitudinal strain on the TEC specimen at 132.3°F (55.7°C).

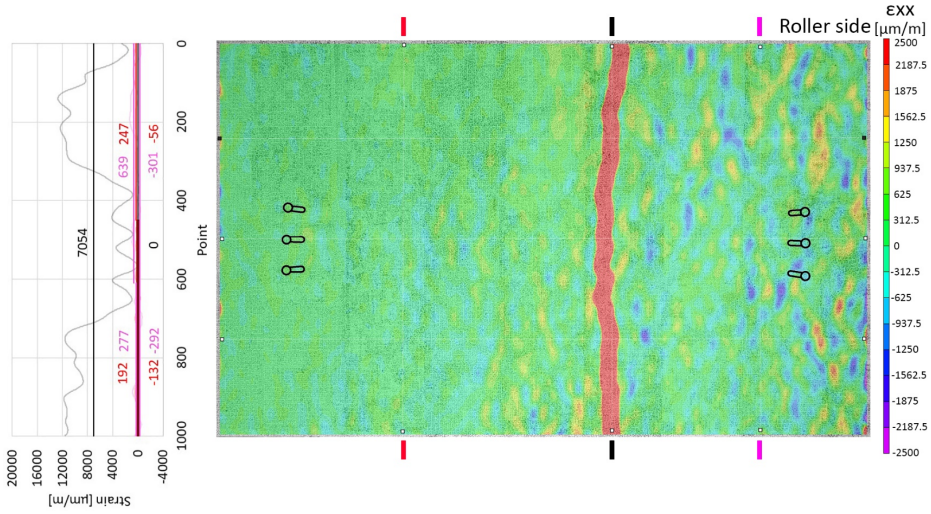

Figure 90. Illustration. Longitudinal strain on the TEC specimen at 133.3°F (56.3°C), when the first crack occurred.

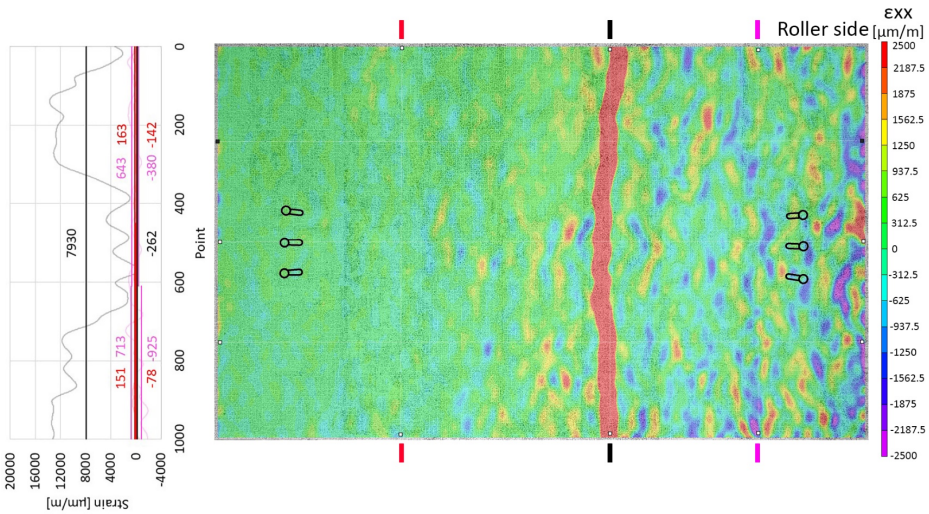

Figure 91. Illustration. Longitudinal strain on the TEC specimen at 137.4°F (58.6°C).

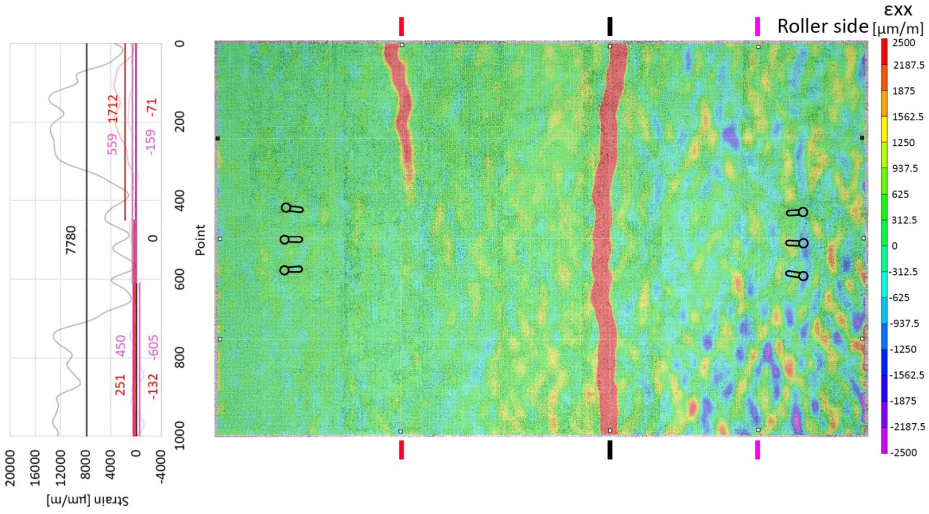

Figure 92. Illustration. Longitudinal strain on the TEC specimen at 137.6°F (58.7°C), when the second crack occurred.

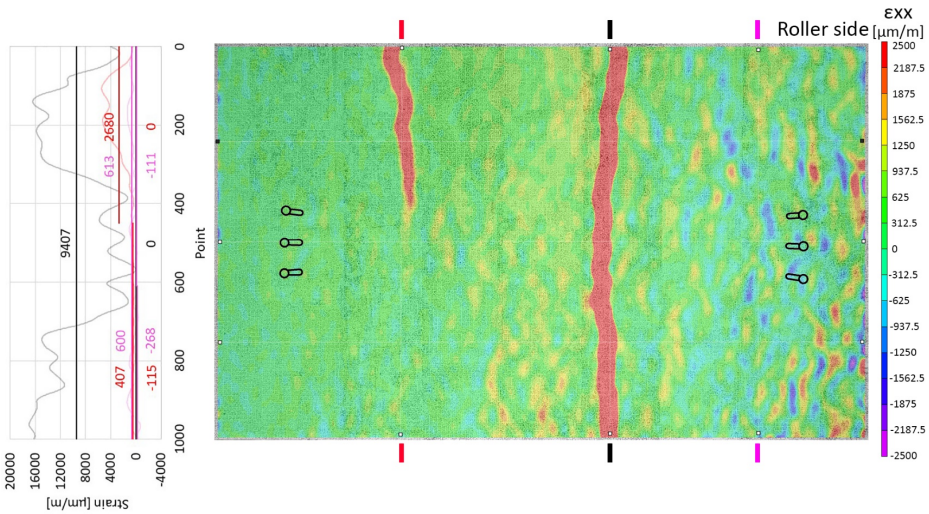

Figure 93. Illustration. Longitudinal strain on the TEC specimen at 152.3°F (66.8°C).

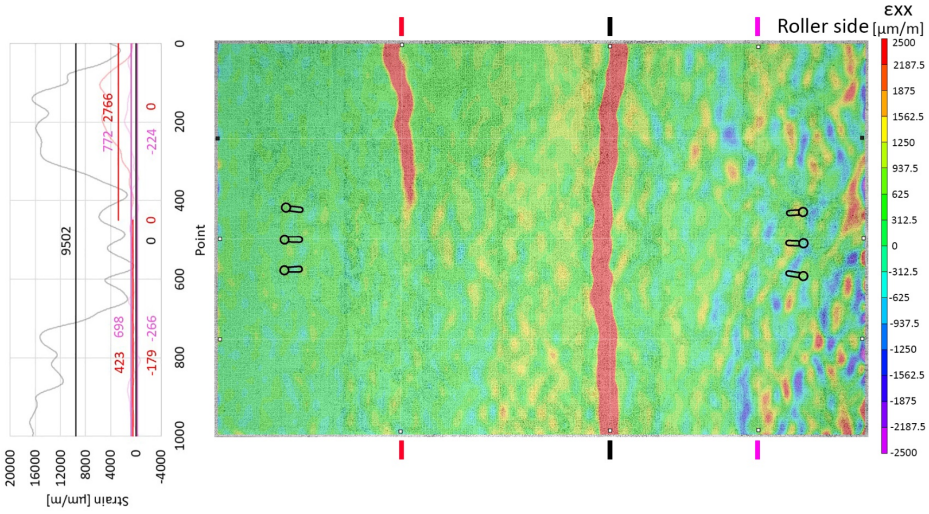

Figure 94. Illustration. Longitudinal strain on the TEC specimen at 152.4°F (66.9°C).

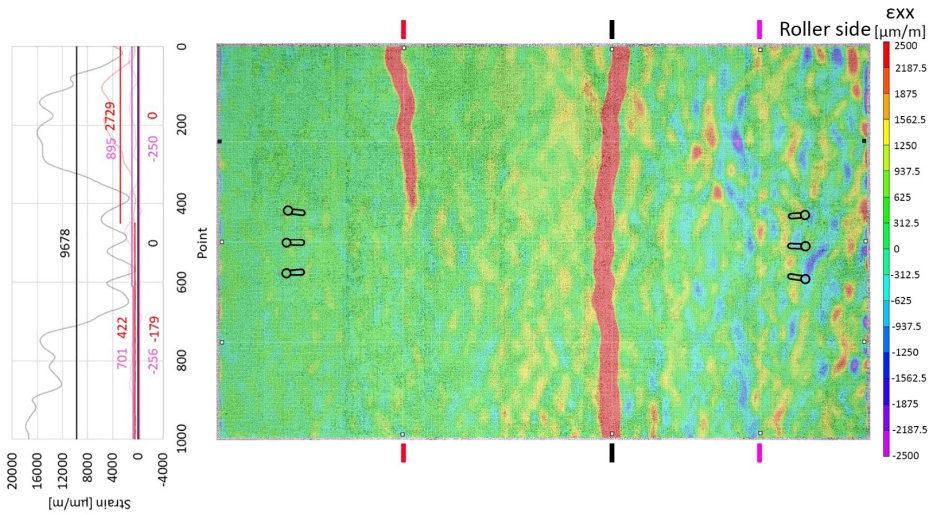

Figure 95. Illustration. Longitudinal strain on the TEC specimen at 152.2°F (66.8°C).

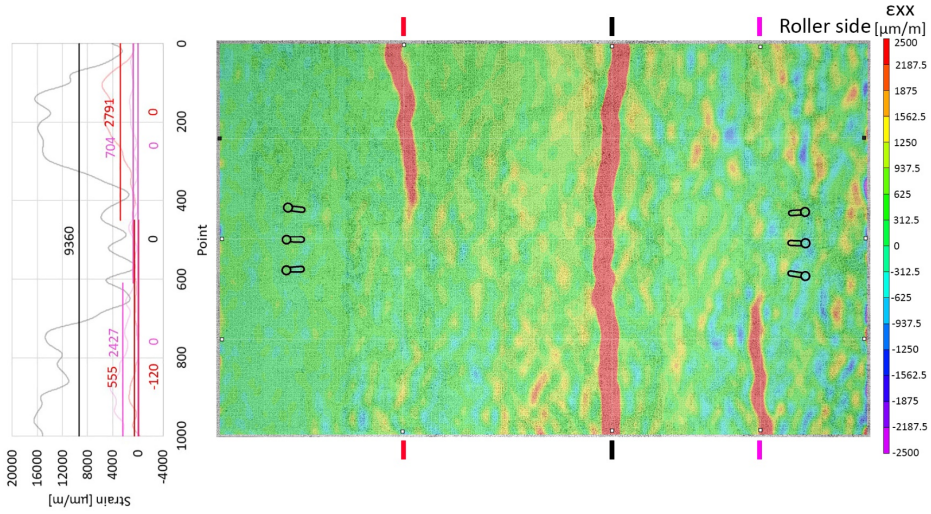

Figure 96. Illustration. Longitudinal strain on the TEC specimen at 152.7°F (67.0°C), when the third crack occurred.

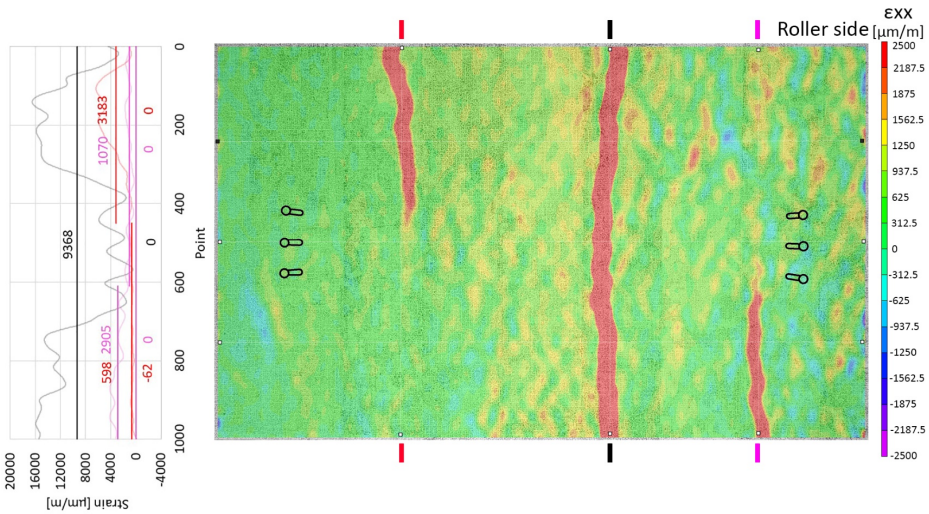

Figure 97. Illustration. Longitudinal strain on the TEC specimen at 145.4°F (63.0°C).

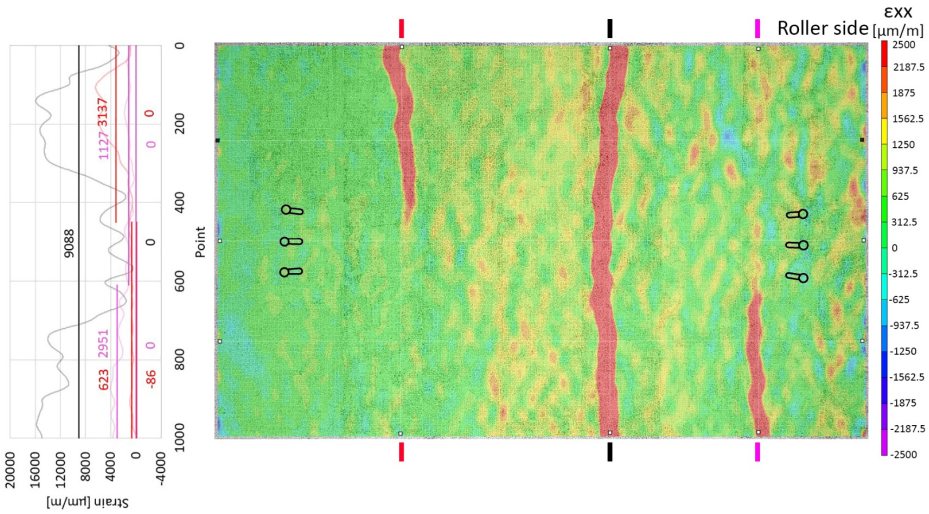

Figure 98. Illustration. Longitudinal strain on the TEC specimen at 144.7°F (62.6°C), when the fourth crack occurred and the burners were turned off.

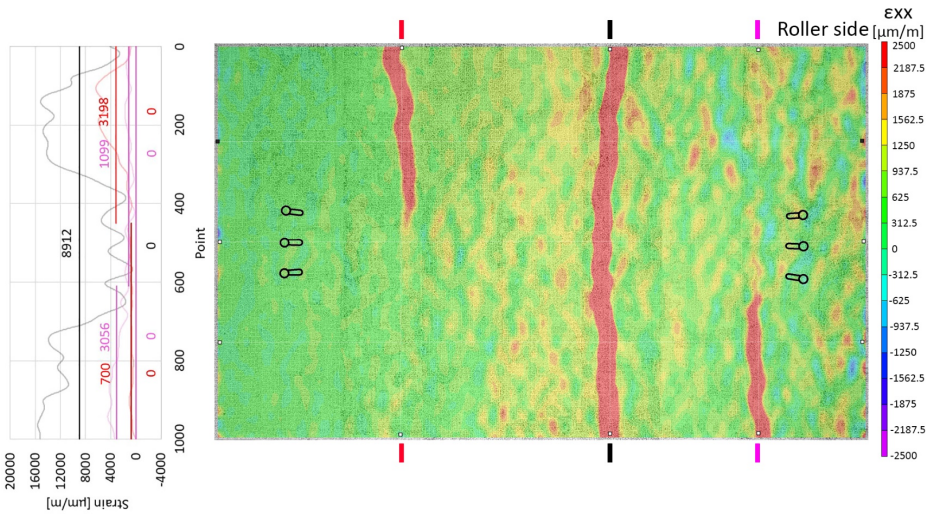

Figure 99. Illustration. Longitudinal strain on the TEC specimen at 139.3°F (59.6°C), during the cooling stage.

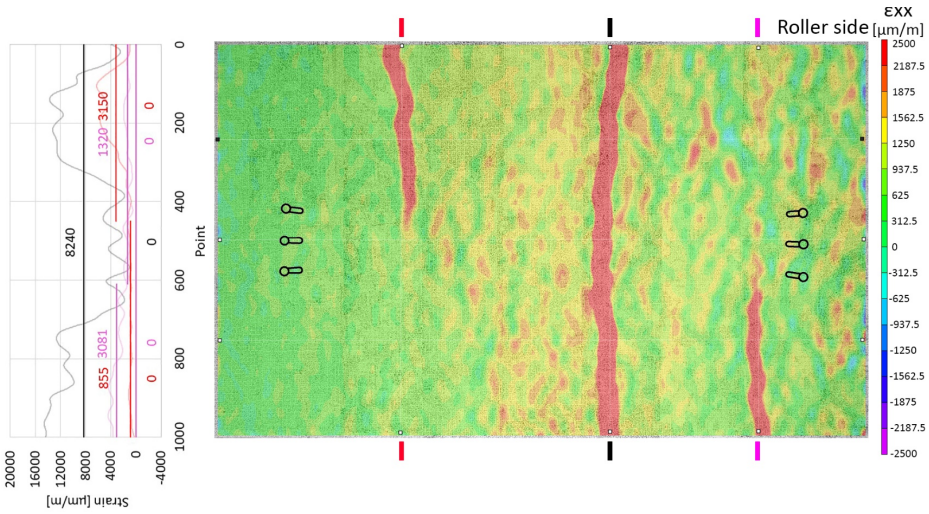

Figure 100. Illustration. Longitudinal strain on the TEC specimen at 125.1°F (51.7°C).

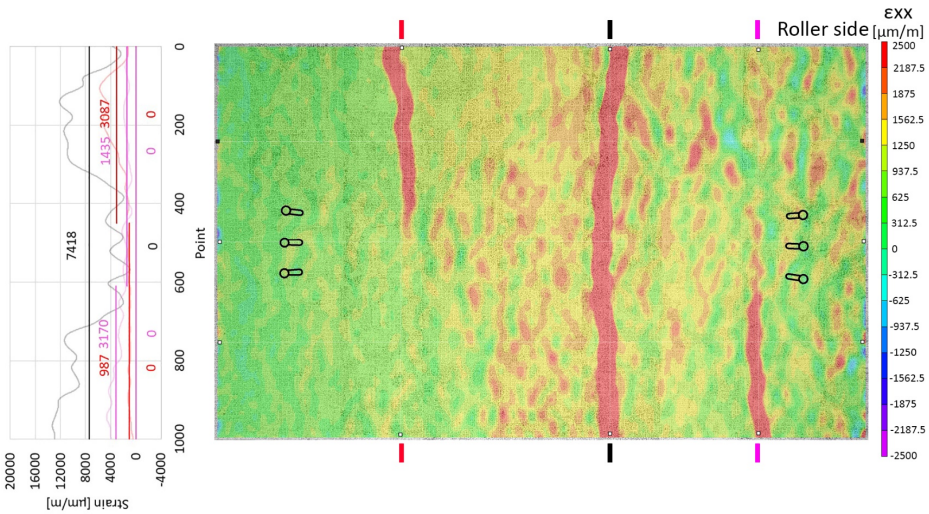

Figure 101. Illustration. Longitudinal strain on the TEC specimen at 110.0°F (43.3°C).

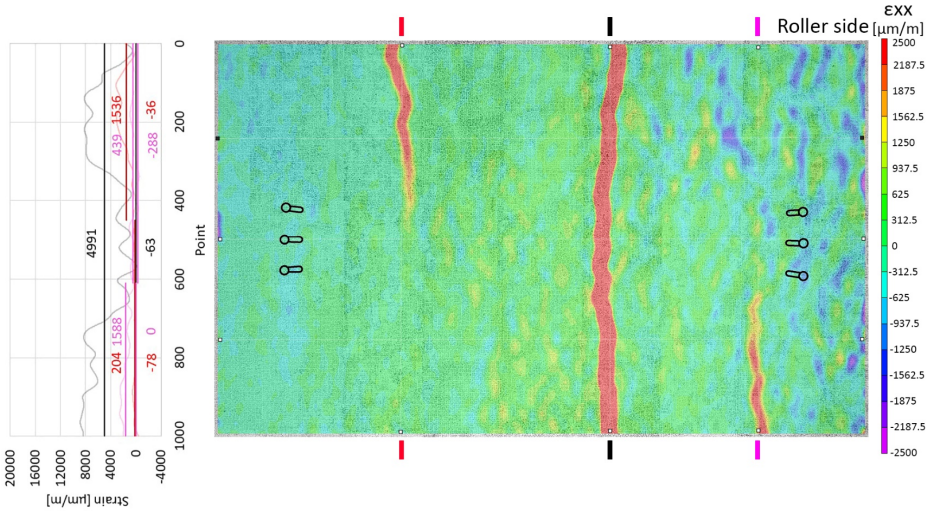

Figure 102. Illustration. Longitudinal strain on the TEC specimen at 72.4°F (22.4°C).


Illinois Department
of Transportation


ILLINOIS